# NUMERICAL INVESTIGATION OF BLOOD RHEOLOGY AND VESSEL ELASTICITY EFFECTS ON HEMODYNAMICS IN ARTERIES WITH ANEURYSM

by

Coşkun Bilgi

B.S., Mechanical Engineering, Boğaziçi University, 2016

Submitted to the Institute for Graduate Studies in
Science and Engineering in partial fulfillment of
the requirements for the degree of
Master of Science

Graduate Program in Mechanical Engineering
Boğaziçi University

2019

# ACKNOWLEDGEMENTS

I would like to express my sincere thanks and gratitude to my thesis supervisor, Prof. Kunt Atalık for his endless support, motivation and patience. His encouragement and wise guidance helped me through my graduate studies. Under his guidance, I successfully overcame many difficulties and learned a lot. I will always remember his contributions to me and consider myself fortunate to have such a concerning mentor.

I would like to thank my thesis committee, Prof. Günay Anlaş and Assist. Prof. Hatice Mercan for devoting their time to read, listen and comment on my study.

I would like to thank Tolga Akıner for all the times we had on and off the campus throughout my studies in the Boğaziçi. Special thanks to him for always being available to help no matter how far he is.

I would like to mention my deepest thanks to the current and former members of our floor, Fatma Mutlu, Eren Bekiloğlu, Gülcan Özerim, Cansu Özerim and Ozan Eriçok especially for the joyful coffee/tea time.

I appreciate the kindness of the departmental staff Seher Yıldız and Özlem Ulufer.

The most special thanks to my family for supporting and comforting me. It would have been impossible for me to made so far without them.

Last but definitely not the least, I cannot express my gratitude with the words to my wife, Selin Baç Bilgi. I am delightful for all of her support, help and love. Your love enlightens and motivates me for the past 9 years, and it will always keep me going.

Finally, financial support provided by TÜBİTAK BİDEB 2210-A and BAP-14761 are acknowledged.

# ABSTRACT

## NUMERICAL INVESTIGATION OF BLOOD RHEOLOGY AND VESSEL ELASTICITY EFFECTS ON HEMODYNAMICS IN ARTERIES WITH ANEURYSM

The aim of this study is to provide insight to how pulsatile hemodynamics varies with rheology of blood and blood vessel elasticity in case of an abdominal aortic aneurysm (AAA). Fluid-solid interaction method with arbitrary Lagrangian-Eulerian formulation is adopted with the Newtonian, the shear thinning Carreau and viscoelastic modified Oldroyd-B constitutive models to represent the rheological behavior of blood and the linearly elastic and the hyperelastic Yeoh wall models. Finite element based numerical solver is used to investigate the blood flow in terms of axial velocity across the AAA, vortical structure and shear stress acting on the aneurysm. The anomalies in the vascular network are monitored using the risk indices such as the oscillatory shear index and the time-averaged wall shear stress. The investigations are carried out for the purely shear thinning properties of the blood by using the Newtonian and Carreau models with different arterial wall models to compare the output parameters. Newtonian assumption for the blood, and modelling the arterial wall as linearly elastic lead to significant differences in oscillatory hemodynamic properties when compared to the use of Carreau fluid together with the hyperelastic vessel model. The combined effects of viscoelasticity and shear thinning properties are investigated by using modified Oldroyd-B, Carreau and Newtonian models. The viscoelastic fluid shows differences in the vortical field, and significantly higher risk indicators compared to the other models. The elasticity effects are further investigated by a smaller aneurysm geometry. The increase in the elasticity changes the vortical structure, and increases the wall shear stress, as well as the risk indicators.

# ÖZET

## KAN REOLOJİSİ VE DAMAR ESNEKLİĞİNİN ANEVRİZMALI ARTERLERDEKİ HEMODİNAMİĞE ETKİLERİNİN SAYISAL OLARAK İNCELENMESİ

Bu çalışmanın amacı, gelişmiş abdominal aort anevrizması (AAA) için pulsatil hemodinamiğin, kanın reolojisi ve damar elastikiyeti ile nasıl etkilendiğini gözlemlemektir. Keyfi Lagrangian-Eulerian formülasyonlu akışkan-katı etkileşim yöntemi ile birlikte Newtonyen, kayma incelmeli Carreau ve viskoelastik Oldroyd-B bünyesel modelleri ve lineer elastik ve hiperelastik Yeoh duvar modelleri kullanılmıştır. Sonlu eleman metodu kullanılarak AAA boyunca eksenel hız, girdapsal yapı ve anevrizma duvarındaki kayma gerilmesindeki değişimler incelenmiştir. Vasküler sistemdeki anomaliler, salınımlı kayma indeksi ve zaman ortalamalı duvar kayma gerilmesi gibi risk indeksleri kullanılarak izlenmiştir. Öncelikle, Newtonyen ve Carreau bünye modelleri ile farklı arter duvar modellerinden elde edilen çıktı parametreleri karşılaştırılarak kanın sadece kayma incelme özellikleri için araştırmalar yürütülmüştür. Kanın Newtonyen kabul edilerek arter duvarının lineer elastik olarak modellenmesi ve Carreau bünye modeliyle hiperlastik damar modelinin birlikte kullanımı kıyaslandığında hemodinamik özelliklerde önemli farklar gözlenmektedir. Viskoelastikliğin ve kayma incelme özelliklerinin birleşik etkileri, Oldroyd-B, Carreau ve Newtonyen bünye modelleri kullanılarak araştırılmıştır. Viskoelastik akışkan diğer modellere göre girdapsallıkta farklılıklara ve risk indekslerinde önemli ölçüde artışa yol açmaktadır. Ayrıca kanın elastik etkileri anevrizmalı geometrinin yarısı çapında bir geometri kullanılarak incelenmiştir. Elastiklikteki artış girdapsal yapıyı değiştirdiği gibi duvar kayma gerilmesini ve risk indekslerini de arttırmaktadır.

# TABLE OF CONTENTS

# LIST OF FIGURES

# LIST OF TABLES

# LIST OF SYMBOLS

| | |
|---|---|
| $E$ | Elastic modulus |
| $El_m$ | Elasticity number |
| $I_{\mathbf{B}}$ | First invariant of the left Cauchy-Green tensor |
| $L$ | Length of the aneurysm |
| $L_{ent}$ | Entrance length |
| $L_{exit}$ | Exit length |
| $\mathbf{n_f}$ | Unit normal vector at the surface of the fluid domain |
| $\mathbf{n_s}$ | Unit normal vector at the surface of the solid domain |
| $p$ | Fluid pressure |
| $R$ | Dilated radius of the aneurysm |
| $r_0$ | Radius of the abdominal aorta |
| $Re$ | Reynolds number |
| $Re_{m,N}$ | Time averaged mean velocity and Newtonian viscosity based Reynolds number |
| $T$ | Period of the cardiac cycle |
| $t$ | Wall thickness |
| $\mathbf{u_f}$ | Fluid displacement vector |
| $\mathbf{u_s}$ | Solid displacement vector |
| $\mathbf{v}$ | Fluid velocity vector |
| $\mathbf{v_g}$ | Velocity vector of the mesh grids |
| $\bar{v}$ | Spatially averaged fluid velocity |
| $\bar{v}_m$ | Time and spatially averaged fluid velocity |
| $W$ | Strain energy density function |
| $Wi$ | Weissenberg number |
| $Wi_m$ | Time averaged mean velocity based Weissenberg number |
| | |
| $\alpha$ | Material parameter for Yeoh model |
| $\beta$ | Material parameter for Yeoh model |
| $\dot{\gamma}$ | Shear rate |

| | |
|---|---|
| $\varepsilon_s$ | Strain tensor for the solid |
| $\kappa$ | Shear rate dependency term for the viscoelastic fluid model |
| $\lambda$ | Carreau relaxation time |
| $\lambda_1$ | Stress relaxation time |
| $\lambda_2$ | Retardation time |
| $\lambda_s$ | First Lamé coefficient |
| $\mu$ | Dynamic viscosity of the blood |
| $\mu_o$ | Total viscosity for the Oldroyd-B model at the zero shear rate |
| $\mu_0$ | Zero shear rate viscosity for Carreau model |
| $\mu_\infty$ | Infinite shear rate viscosity for Carreau model |
| $\mu_N$ | Reference Newtonian viscosity for the blood |
| $\mu_p$ | Polymeric viscosity |
| $\mu_{p,0}$ | Polymeric viscosity at the zero shear rate |
| $\mu_{p,\infty}$ | Polymeric viscosity at the infinite shear rate |
| $\mu_s$ | Solvent viscosity |
| $\mu_{solid}$ | Lamé coefficient *or* shear modulus for the solid |
| $\nu$ | Poisson's ratio |
| $\rho$ | Density of the blood |
| $\rho_s$ | Density of the vessel |
| $\sigma_f$ | Total stress tensor of the blood |
| $\sigma_s$ | Solid stress tensor |
| $\tau$ | Extra stress tensor |
| $\tau_p$ | Polymeric stress contribution of the extra stress |
| $\tau_{p,rr}$ | Polymeric normal stress in the r-direction |
| $\tau_{p,zz}$ | Polymeric normal stress in the z-direction |
| $\tau_{p,\theta\theta}$ | Polymeric normal stress in the $\theta$-direction |
| $\tau_s$ | Solvent stress contribution of the extra stress |

# LIST OF ACRONYMS/ABBREVIATIONS

| | |
|---|---|
| AAA | Abdominal Aortic Aneurysm |
| ALE | Arbitrary Lagrangian-Eulerian |
| FSI | Fluid-Solid Interaction |
| LAM | Large Artery Model |
| OSI | Oscillatory Shear Index |
| SAM | Small Artery Model |
| TAWSS | Time Averaged Wall Shear Stress |
| WSS | Wall Shear Stress |

# 1. INTRODUCTION

Cardiovascular system of a human consists of heart, arteries, veins and capillaries. The heart contracts to pump the blood through the aorta, and it relaxes to create a suction force to pull the blood from the veins. These contractions and relaxations of the heart cause periodic oscillations in flow rate in the arteries, which is known as pulsatile flow [1]. The pulsatile conditions appearing in the arterial part along with the changes in the pressure and velocity fields in the circulation system are given in Figure 1.1.

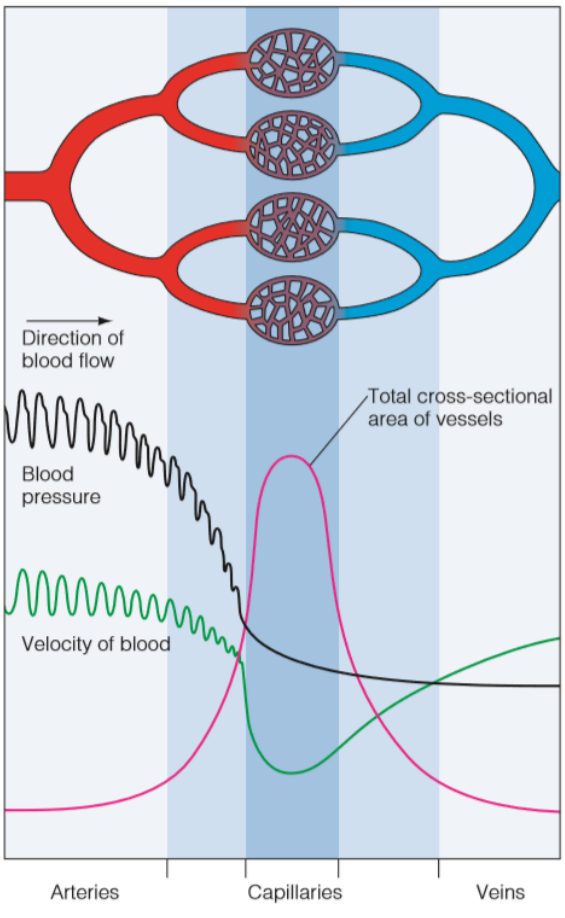


Figure 1.1. Representation of the circulatory network and pulsatile flow in the arteries [2].

### 1.1. Blood Rheology and Blood Flow Modeling

The blood is composed of blood cells, protein and lipid molecules, and their composition in a healthy blood is given in Table 1.1. The red blood cells acquire the highest percentage of the cellular components of the blood and their volume corresponds to ∼43% of the whole blood. They can be thought as fluid filled elastic cells, therefore the blood is expected to display viscoelastic properties, which are the result of elastic deformability of the red blood cells with their ability to form aggregates known as rouleaux [3–5]. The *rouleaux* formation mostly occurs at low shear rates. Therefore the non-Newtonian and elastic properties are dominant at the low shear rates, and the pulsatile nature of the blood magnifies the viscoelastic effects [6]. Formation of the aggregates gives rise to yield stress property, therefore blood is treated as viscoplastic fluid in some studies in the literature [7–10]. However, there is controversy about the viscoplastic behavior of the whole blood in the physiological conditions. Both the clinical and experimental studies show that the viscoplastic behavior has small effects on the blood flow at the natural flow ranges in medium and large arteries [10].

Table 1.1. Composition of whole human blood.

| **Plasma Components (∼57%)** | **Composition** |
|---|---|
| | Water (∼92%) |
| | Proteins (∼7%) |
| | Other solutes (∼1%) |
| **Cellular Components (∼43%)** | **Cell Type** |
| | Red blood cells(∼99.7%) |
| | White blood cells (∼0.2%) |
| | Thrombocytes (∼0.1%) |

Blood flow modelling is important to understand the hemodynamic effects occurring in the circulatory system. The development of some pathological conditions, such as atherosclerotic plaques, dilations and arterial lesions [11,12], are highly related with the blood flow dynamics. A rheological model close to the natural properties

of the blood is important to capture and analyze the flow field and the physiological conditions such as flow recirculation, separation, low and oscillating wall shear stress.

Blood is assumed to behave as a Newtonian fluid in many hemodynamic studies [13–17]. However, Berger and Jou [18] stated Newtonian assumption is only valid at shear rates higher than $100s^{-1}$ which generally occur in large arteries. Transient and pathological conditions, such as bifurcations and dilations of blood vessels, result in shear rates below $100s^{-1}$, where non-Newtonian effects become important. The shear thinning properties of blood have been shown by Chien *et al.* [19], and the parameters corresponding to the power-law, Carreau, and Cross models are obtained experimentally. The shear-thinning property of the blood at low shear rates necessitate the use of non-Newtonian fluid models to simulate more accurately the flow behavior.

As aforementioned, the blood is composed of blood cells, protein and lipid molecules, therefore it has viscoelastic properties along with the shear thinning properties. Thurston [20] was one of the earliest researchers reporting the viscoelastic nature of the blood and showed the elastic properties diminish with the increasing shear rate. Thurston [21, 22] conducted experiments with whole human blood under steady and oscillatory conditions to determine the viscoelastic and thixotropic properties of the blood combined with the shear thinning properties. In the study of Thurston [21], parameters for the six mode generalized Maxwell model are obtained, and the dependence of these modes on the shear rate are shown in detail. Yeleswarapu [23] conducted experiments with the porcine blood to obtain the viscoelastic and shear thinning parameters for the modified Oldroyd-B model with a shear thinning viscosity formulation for the elastic part of the blood. Then, Yeleswarapu *et al.* [24] compared the velocity field in a rigid tube under steady conditions with the developed modified Oldroyd-B formulation [23]. They showed that Newtonian assumption overestimates the velocity values in the experimental conditions and the viscoelastic nature of the blood should be taken into account along with its shear thinning property. Anand and Rajagopal [25] developed a shear thinning viscoelastic fluid model, which has a shear rate dependent relaxation time, and the model has been improved further into a generalized Oldroyd-B model in [26]. According to Anand *et al.* [26] the model proposed by Anand and Ra-

jagopal [25] was problematic for numerical simulations, having convergence problems for the mass and momentum equations in complex geometries. In the study of Anand *et al.* [26] they used the generalized Oldroyd-B model to solve the flow in straight and bent tubes, and they showed the differences between the improved model and the previously proposed model [25]. Campo-Deano *et al.* [27] used whole human blood in the rheometer experiments to obtain the viscoelastic parameters for Giesekus and sPTT models, and their aim was to find a suitable suspension which could mimic the viscoelastic behavior of the blood to be used in the experimental studies. Bodnar *et al.* [28] have compared the shear thinning Cross, Oldroyd-B and Generalized Oldroyd-B viscoelastic models for the blood under steady flow conditions in a rigid walled idealized circular stenosis geometry. They compared the results in terms of pressure drop, velocity along the artery and wall shear stress values. Shariatkhah *et al.* [29] used Oldroyd-B and Giesekus models under pulsatile flow conditions in a rigid walled capillary model. The differences in the velocity and shear stress are presented for different rheological models. Rojas [30] used the Thurston's [21] viscoelastic model in a circular rigid walled artery, and the differences in the velocity field and the wall shear stress values are compared with Newtonian model under pulsatile conditions. The results showed that the elastic properties cause huge differences in the velocity field in transient models.

It should be noted that the rheological experiments available in the literature are generally conducted with mammal blood [19, 23, 31]. Although, the mammal blood is known to be similar to the human blood, the average cell size and the cell concentrations differ [32], which may lead to changes in the *rouleaux* formation. Since the aggregation of the blood cells is the main reason of shear thinning behavior of the blood, the rheological properties of the mammal blood are expected to be different than human blood [21].

### 1.2. Artery Properties and Arterial Modeling

Different types of blood vessels vary in their structures, although they share the same features. Arteries have thicker walls than veins since they are closer to the heart and receive blood with higher pressure. Each type of vessel has a lumen which is a

hallow passageway where the blood flows. The lumens of the arteries are smaller than veins that help to maintain the pressure of blood while moving through the system. The thicker walls and smaller diameters of arterial lumens give a more rounded appearance than vein lumens. Also, both the arteries and the veins have the three distinct layers of tissue, and these layers are known as intima, media and adventitia/externa. These three layers and the lumen are given for an artery and a vein in Figures 1.2a and 1.2b, respectively. The layer of intima is composed of epithelial and connective tissues, and the epithelial tissue is often called as endothelium. The media is the middle layer of a vessel wall, and it is the thickest layer of an artery. The media consists of smooth muscle layer with the connective tissue which is made from the elastic fibers oriented as circular sheets. The adventitia layer is generally composed of collagen fibers and it can withstand high pressure values [33]. These layers have varying mechanical properties [2]. Therefore, an accurate arterial wall model should take into account these three layers, as well as the anisotropic effects due to the collagen fibers in the aortic tissue.

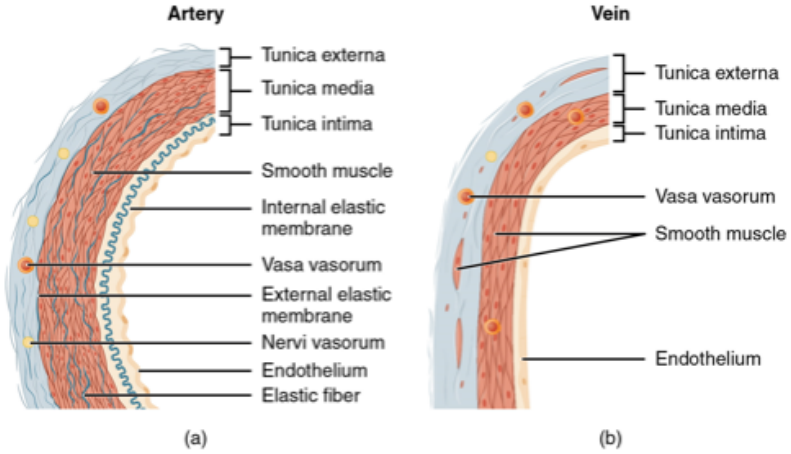


Figure 1.2. Representation of the layers in the blood vessels: (a) artery, (b) vein [33].

The aorta modelling is important to capture true response of the hemodynamics in the human body. Therefore, the structural models for the vessels have been studied widely in the literature [34–39]. The experimental studies on the vessel elasticity

have first been conducted by Fuchs [35]. In their study, a removed thraoric aorta is used to obtain the elastic modulus and Poisson's ratio. In the following years, Bergel [34] has studied elastic properties of a thraoric aorta *in vivo* conditions under static loading. In the study, the elastic moduli for thraocic and abdominal aortas have been calculated for four different pressure values. Also, the effect of hysteresis under repetitive loading and unloading has been shown. In addition to the findings of the study, a warning has been given regarding the previous studies on the elasticity of the vessels, where the experiments are conducted after the removal of the aorta from the body. The removal of the aorta leads to a retraction and these studies seem to neglect its effect, as in the study of Fuchs [35]. The improvements on the determination of mechanical properties of arteries in the following years have been summarized by Dobrin [40]. In this study, the experiments and clinical observations regarding the vessel wall elasticity are explained in detail, especially for the linearly elastic wall models in the circumferential and elongational directions. Also, the anisotropic effects of collagen fibers are discussed in the same study.

There is an increasing interest on the arterial wall models increased to obtain a model that mimics the biological movements of a vessel through a cardiac cycle. Raghavan and Vorp [36] proposed a hyperelastic model for the rubber-like behavior of the arteries, and their model has been widely used for the elastic vessel studies [41–45]. Their proposed model shows that the stress acting on the walls of an aneurysm is much higher compared to the linearly elastic model.

A new constitutive model, known as Odgen material, for arterial walls have been developed by Holzapfel *et al.* [37, 38]. In Odgen model, the aortic layers are treated as a thick-walled tube composed of two parts with non-linear elasticity, the inner part as the media and intima, and the adventitia as the outer part. Each layer is modeled as reinforced with fibers in the arterial tissues, which correspond to the collagen fibers.

## 1.3. Aneurysm Types, Geometries and Modeling

Arterial aneurysms are pathological conditions where the arterial vessel tissue dilates permanently and the dilation generally occurs in aorta and carotid/cerebral arteries. There are three common types of aneurysms, saccular, fusiform and false. The saccular aneurysms generally occur on cerebral arteries, whereas fusiform ones generally appear on the aorta. In contradiction to the true aneurysms, the false aneurysms are not related with the appearance of the dilation. In the false type, the dilation happens due to the hemorrhage between the endothelial cells and the layers of the artery. In this thesis, a fusiform type aneurysm positioned on aorta is investigated, and the most common type of aortic aneurysms occur at abdominal aorta, which is known as abdominal aortic aneurysm (AAA). The position of the aorta in the human body with the types of aneurysms, saccular, fusiform and false, are shown in the Figure 1.3.

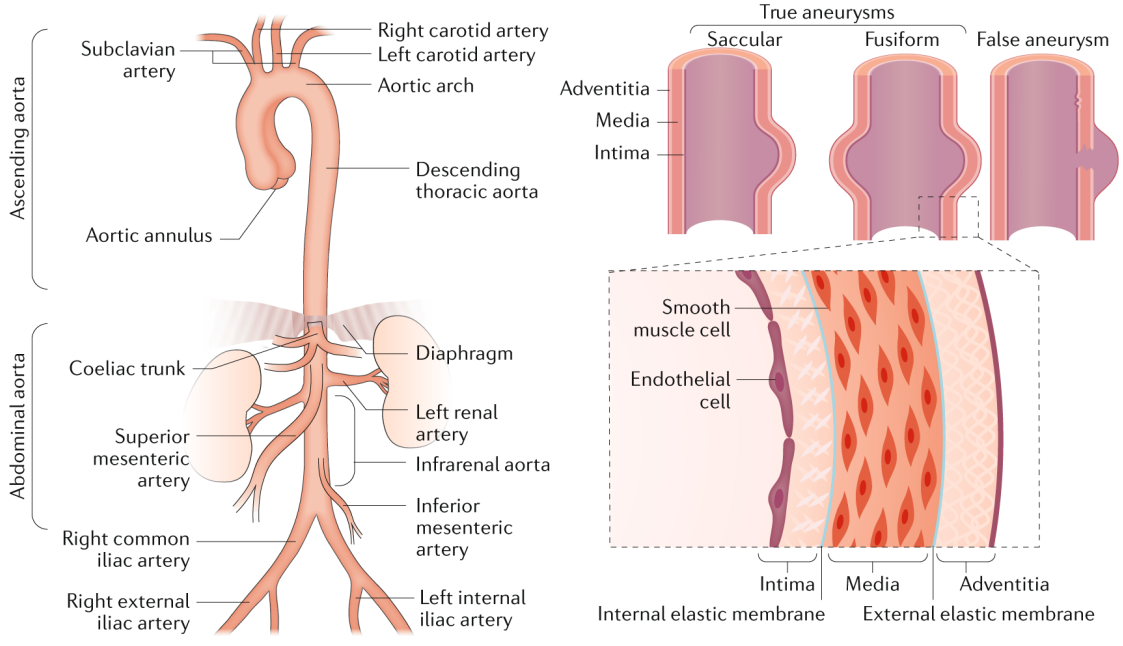


Figure 1.3. The aorta in the human body and types of aneurysms [46].

The aneurysms are mostly asymptomatic and their ruptures are associated with high mortality rates [47, 48]. Although the size of an aneurysm is commonly used as an indicator of rupture risk, there are examples where rupture occurs in small

aneurysms [48]. The advanced studies on aneurysms show that hemodynamic factors are better indicators of rupture than the size of the aneurysm [13, 49].

The studies on AAA in the literature focus on fusiform aneurysms and the aneurysms are located in the infrarenal region, since they are the most common case [50]. Transparent dilated pipes are used to study abdominal aortic aneurysms experimentally in terms of the vortical structure, velocity profiles and wall shear stresses. Budwig *et al.* [17] presented the vortex structure, velocity profile and the increase in the wall shear stress at the distal and proximal ends of the aneurysm under steady flow conditions. Egelhoff *et al.* [51] have shown the vortex translation in the aneurysmal cavity under pulsatile flow. The experiments of Fukushima *et al.* [52] have shown the flow patterns differ dramatically under pulsatile flow conditions and the transient nature of blood flow should not be neglected. In most of the previous hemodynamic studies on aneurysms modeling, blood has been assumed as an incompressible Newtonian fluid and blood vessels have been assumed as rigid walls, also branch arteries have been neglected [53, 54]. Taylor *et al.* [14, 55] developed a finite element based software to investigate blood flow in abdominal aorta and help surgical procedures under Newtonian fluid and rigid blood vessel assumptions. Javadzadegan *et al.* [56] have shown the differences in the blood flow and the risk indicators resulting from the aneurysm location by using the assumptions of rigid walls and Newtonian fluid. Khanafer *et al.* [57] and Neofytou and Tsangaris [58] investigated the effects of different non-Newtonian models in pathologically diseased arteries with rigid walls. Recenlty, Arzani [59] proposed a rheological model accounting the rouleaux formation time scale in blood shear thinning behavior. It has been argued that non-Newtonian effects are overestimated in aneurysm hemodynamics, and Newtonian models are more appropriate for this flow. The elasticity of arterial vessels are as important as the fluid rheology in hemodynamic modelling. With the advances in computational modelling techniques, elastic blood vessel models have been commonly available [16, 60, 61]. First studies on fluid-solid interaction (FSI) showed slight differences in wall shear stress values with respect to rigid wall assumption [41, 62]. However, further improved results showed the maximum wall shear stress increases by 12.5% for the linearly elastic model [63]. In addition to the linearly elastic models, hyperelastic modelling is used to model rubberlike behavior

of the blood vessel [36, 64]. Raghavan *et al.* [36] have shown the differences in the stress field exerted on the AAA between Yeoh and linearly elastic models. Recently, Stergiou *et al.* [65] have investigated the differences occuring in the wall shear and von Mises stresses with different hematocrit values by using viscoplastic Casson model for blood in combination with Yeoh wall model. Their results indicate that lower hematocrit values result in low wall shear stress. Advanced imaging techniques have allowed the researchers to directly import the geometry of AAA from the patients [41, 66–70]. These studies are important to understand the effects of the morphological geometry of the aneurysm with branch (iliac and renal) arteries and other pathological issues like intraluminal thrombus and plaque formation. However, there are reproducibility and generalization concerns with the patient specific geometries.

From a physiological point of view, flow disturbances due to aneurysms may lead to arteriosclerosis which is defined as the increase in the stiffness of the arterial walls [71]. The flow disturbances occur at bifurcations or expansions (aneurysm and stenosis) where stagnation and recirculation zones are observed. Researchers have developed correlations between the shear stress properties and lesions formation in arteriosclerosis. Kleinstreuer *et al.* [72] proposed a model to predict plaque formation at the regions with low wall shear stress values. Malek *et al.* [11] stated that low wall shear stress ($<$0.4 Pa) regions manifest greater endothelial cell cycling, and the change in the orientation of endothelial cells is a stimuli for the arterial tissue deformation. Ku [73] emphasized the relation between oscillatory shear stress and lesion development. According to their study, high oscillatory shear index (OSI) and low time averaged wall shear stress (TAWSS) lead to high risk of arteriosclerosis. Kawaguchi *et al.* [12] also showed high OSI values and rupture of the tissue are strongly related. Arzani and Shadden [74] showed the Pearson correlation is valid between the risk indicators based on the wall shear stress by using computational fluid dynamics in patient specific geometries. According to their results, the Pearson correlation coefficient for the relation between OSI and TAWSS is negative valued which means high OSI is likely to result in low TAWSS.

### 1.4. The Objectives and the Outline of the Study

There are many studies in the literature which take into account the shear thinning properties of the blood and the elastic nature of the blood vessels, separately. Also, the viscoelasticity of the blood is studied by many researchers. The main objective of this study is to reveal the combined effects of the wall compliance and non-Newtonian blood rheology in aortic aneurysms under pulsatile flow conditions. In this study, the investigation of the effects due to blood rheology can be separated into two parts, the first part focuses on the purely shear thinning property of the blood together with the vessel elasticity, and the second part focuses on the combination of the viscoelastic and shear thinning properties. In the former part, the blood vessel elasticity is investigated by using the hyperelastic, linearly elastic and rigid wall conditions and the shear thinning effects are investigated using Newtonian and the shear thinning non-Newtonian Carreau models and compared to observe the difference in the blood flow due to the fluid rheology. In the latter part, generalized Oldroyd-B model is used to investigate both shear thinning and viscoelastic effects due to fluid rheology and linearly elastic wall model is chosen to mimic the vessel behavior under pulsatile conditions. The simulations are carried out by fluid-solid interaction (FSI) model with Arbitrary Lagrangian-Eulerian (ALE) formulation for both linearly elastic and hyperelastic vessels. The differences in hemodynamics are investigated in terms of the axial velocity profile across the AAA, vortical structure, shear stress along the aneurysmal wall and risk indicators such as OSI and TAWSS. The mathematical formulation and solution method are presented in Sections 2 and 3, respectively. Tests and validations of the models are shown in Section 4, and the results and discussions are given in Section 5, before concluding in Section 6.

# 2. MATHEMATICAL FORMULATION

In this section the model used for the aneurysm, the formulations describing the fluid and solid domain, as well as the coupling between these domains are explained briefly.

## 2.1. Aneurysm model

The aneurysm evaluated in this study is a true aneurysm with fusiform type and it is located at the infrarenal region of the abdominal aorta between the renal arteries and the iliac bifurcation. The corresponding region can be observed in the Figure 1.3.

Although abdominal aortic aneurysms (AAA) have unique three dimensional geometry for every patient, the studied aneurysm model is idealized as two dimensional and axisymmetric. This idealization of the aneurysmal cavity and the aorta may fail to represent patient specific blood flow fields and neglect geometric non-linearity effects, however it is useful for carrying out a comparative parametric study between different models for the blood and vessel walls, which helps to have a general insight on the blood flow in the aneursyms independent of the patient specific geometric variations. The geometrical representation of the blood vessel used in the comparisons for the effects of purely shear thinning properties of the blood is given in Figure 2.1, as a two-dimensional axisymmetric aneurysm. In the computational model the sub-arterial branches are not taken into account since the abdominal aortic aneurysm is assumed to be located at the infrarenal region. The aneurysmal arc is defined with the following function:

$$f(z) = \frac{R - r_0}{2}\left[1 + \cos\left(\frac{2\pi z}{L}\right)\right] + r_0 + t \ , \ 0 \leq z \leq L \tag{2.1}$$

where $L$ is the length of the aneurysm, $r_0$ is the radius of aorta and $R$ is the dilated radius of the aneurysm. Head to neck ratio is selected as $L/r_0 = 8$ for this study since it is a typical fusiform for AAAs [50] and the dilation ratio is selected as $R/r_0 = 2.5$ to

investigate the effects for moderate sized aneurysm. The walls of the blood vessel are modeled as uniform and homogeneous with wall thickness $t$. The undilated reference radius of the aorta is $r_0 = 8mm$ and the thickness of the wall is $t = 1.5mm$. For the rigid walled simulations, the wall thickness is omitted.

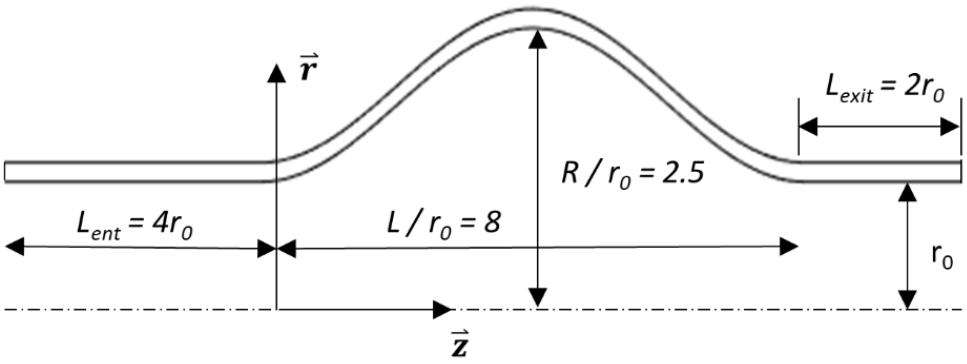


Figure 2.1. Representation of the computational model used in the comparison of purely shear thinning effects of blood rheology.

For the purely shear thinning model fully developed pulsatile flow is applied at the entrance boundary as the inlet condition and pressure waveform is applied at the outlet. The applied boundary conditions, correspond to mean pulsatile flow at the infrarenal region and the pressure waveform at the iliac bifurcation, reported by Mills *et al.* [75] under resting conditions, are represented in Figure 2.3. Therefore, the entrance length, $L_{ent}$ , is accepted as the distance from the renal arteries and the exit length, $L_{exit}$, is the distance from the iliac bifurcation are taken as $L_{ent} = 4r_0$, and as $L_{exit} = 2r_0$, respectively. For the viscoelastic fluid model, the pressure boundary condition at the exit is not applied in order to reduce the constraints on the system. Therefore, the exit and entrance lengths are taken longer than the purely shear thinning model instead of applying the pressure boundary condition. In the viscoelastic model, the entrance length, $L_{ent}$ and the exit length, $L_{exit}$, are taken as $L_{ent} = 10r_0$, and as $L_{exit} = 25r_0$, respectively. The representation of the aneurysm model used in the viscoelastic fluid simulations are shown in Figure 2.2. Similar to the purely shear thinning model, the wall thickness is only present in the elastic walled simulations.

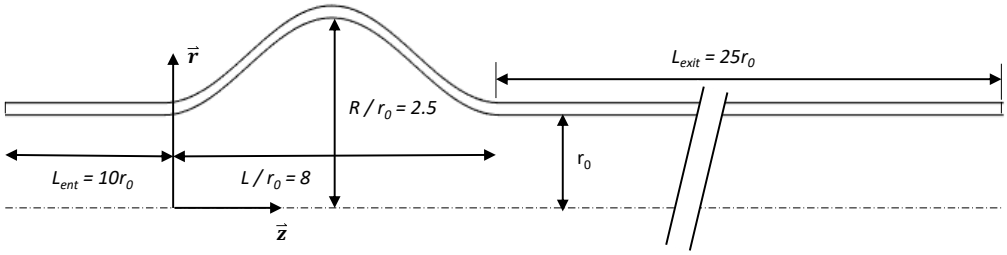


Figure 2.2. Representation of the computational model used in the comparison of viscoelastic effects of blood rheology.

The inlet boundary condition displayed in Figure 2.3 is the time dependent spatially averaged velocity, $\bar{v}(t)$, recorded at *in vivo* conditions for the abdominal aorta during a cardiac cycle. The waveform of the velocity displays the peak systole at $t = 0.32\ s$ and the end of systole, diastole, at $t = 0.53\ s$.

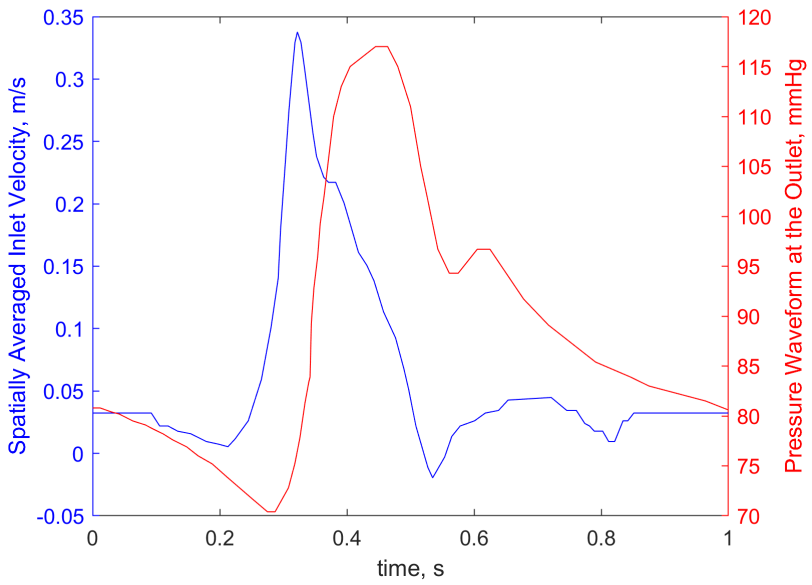


Figure 2.3. *In vivo* spatially averaged velocity and pressure conditions in the infrarenal region during a cardiac cycle [75].

## 2.2. Fluid Domain Formulation

In the simulations, the blood is assumed to be incompressible and the flow is laminar for the considered Reynolds ($Re$) numbers. The Arbitrary Lagrangian-Eulerian (ALE) formulation is used in the fluid domain which is important for the mesh adjustments in the fluid-solid interaction problems. The governing mass and momentum equations can be written respectively as,

$$\nabla \cdot \mathbf{v} = 0 \tag{2.2}$$

$$\rho\Big(\frac{\partial \mathbf{v}}{\partial t} + (\mathbf{v} - \mathbf{v_g}) \cdot \nabla \mathbf{v}\Big) = -\nabla p + \nabla \cdot \tau \tag{2.3}$$

where $\rho$ is the blood density, $\mathbf{v}$ is the velocity vector of the blood, $\mathbf{v_g}$ is the grid velocity, $p$ is the fluid pressure, and $\tau$ is the extra stress tensor. Three different constitutive models are used for the extra stress tensor to observe the effect of complex rheological property of the blood.

The definition of the extra stress tensor depends on the fluid rheology, and three different constitutive equations for the fluid viscosity are employed in the study. These models are namely, Newtonian, the shear thinning Carreau and the modified Oldroyd-B model which is proposed by Yeleswarapu [23]. These rheological models as well as their constitutive equations are described in detail in the following subsections.

### 2.2.1. Newtonian Model

The viscosity is independent of shear rate in the Newtonian model. The Newtonian assumption is commonly valid at shear rates $> 100\ s^{-1}$ [18], which generally occur in large vessels without abnormalities.

The extra stress tensor for the Newtonian model is defined as,

$$\tau = \mu(\nabla \mathbf{v} + (\nabla \mathbf{v})^T) \tag{2.4}$$

The dynamic viscosity value, $\mu$, is chosen as $\mu = 3.45\ mPa.s$, and the Newtonian fluid assumption and the corresponding Reynolds number are used as the reference states throughout the study.

### 2.2.2. Carreau Model

The Carreau model is an inelastic non-Newtonian model exhibiting shear thinning effects. However, in this model the viscosity value is constant at low and high shear rates, defined as zero-shear-rate and infinite-shear rate viscosities, respectively. This model yields high viscosity values at low shear rates similar to rheological experiments conducted with the whole human blood [76]. Also, the blood is observed to behave as a constant viscosity fluid at high shear rates which is consistent with Newtonian fluid assumption for blood at shear rates higher than $100s^{-1}$ [18]. The extra stress tensor for this model is expressed as,

$$\tau = \{\mu_\infty + (\mu_0 - \mu_\infty)[1 + (\dot{\gamma}\lambda)^2]^{\frac{n-1}{2}}\}(\nabla \mathbf{v} + (\nabla \mathbf{v})^T) \tag{2.5}$$

where $\dot{\gamma}$ is the shear rate given as $\dot{\gamma} = \sqrt{I_2/2}$, with $I_2$ defined as the second invariant of the rate of the deformation tensor. The model parameters for blood are obtained from the rheometer experiments conducted by [77], and the parameters for Carreau model are given as the infinite shear rate viscosity $\mu_\infty = 3.45\ mPa.s$, the zero shear rate viscosity $\mu_0 = 56\ mPa.s$, the Carreau relaxation time $\lambda = 3.313\ s$, and the Carreau power index $n = 0.36$. The value of the infinite shear rate is consistent with the Newtonian model, and as the shear rate increases the Carreau model displays constant viscosity values, which is similar to the Newtonian model.

### 2.2.3. Modified Oldroyd-B Model

Whole blood is treated as a dilute solution in the rheological models in the literature [21,27]. The Oldroyd-B model is suitable in the simulations of dilute viscoelastic solutions. The Oldroyd-B model is achieved by replacing the time derivative of the extra stress with the upper convected, Oldroyd derivative, in the Jeffrey's model. The differential form of the Jeffrey's model is shown as,

$$\tau + \lambda_1 \frac{\partial \tau}{\partial t} = \mu_o \Big[ \dot{\gamma} + \lambda_2 \frac{\partial \dot{\gamma}}{\partial t} \Big] \tag{2.6}$$

where $\lambda_1$ is the stress relaxation time, $\lambda_2$ is the retardation time and $\mu_o$ is the total viscosity at the zero shear rate. The extra stress term can be split into two as the polymeric and the solvent contributions to the extra stress. The split formulation of Jeffrey's model can be written as,

$$\tau = \tau_s + \tau_p \tag{2.7}$$

where $\tau_s$ and $\tau_p$ are the of the solvent and the polymeric stress terms, respectively. These stress terms can be expressed in terms of the polymeric stress as,

$$\tau_p + \lambda_1 \frac{\partial \tau_p}{\partial t} = \mu_p \dot{\gamma} \tag{2.8}$$

$$\tau_s = 2\mu_s \dot{\gamma} \tag{2.9}$$

where $\mu_p$ and $\mu_s$ are the polymeric and solvent viscosities, respectively. The total viscosity at the zero shear rate, $\mu_o$ is the summation of the polymeric and the solvent viscosities, $\mu_o = \mu_s + \mu_p$.

As mentioned above in the Oldroyd-B model the time derivative of the extra stress tensor is replaced with the upper convected derivative, therefore the Oldroyd-B model in the split form can be written as,

$$\tau_p + \lambda_1 \overset{\nabla}{\tau_p} = 2\mu_p \dot{\gamma} \tag{2.10}$$

where $\overset{\nabla}{(\cdot)}$ represents the upper convected derivative operator and it is defined as,

$$\overset{\nabla}{\tau_p} = \frac{\partial \tau_p}{\partial t} + (\mathbf{v} - \mathbf{v_g}) \cdot \nabla \tau_p - [(\nabla \mathbf{v}) \cdot \tau_p + \tau_p \cdot (\nabla \mathbf{v})^T)] \tag{2.11}$$

where $\mathbf{v}$ is the velocity of the fluid, and $\mathbf{v_g}$ is the velocity vector of the grid. The contribution of the ALE formulation can be observed in the grid velocity term in the upper convected derivative.

From the experiments [19,21,27,77], it is well known that the blood exhibits shear thinning behavior, however the parameters of the Oldroyd-B model are independent of the shear rate. In order to combine the shear thinning and viscoelastic properties of the whole blood, Yeleswarapu [23] proposed a modified Oldroyd-B model, where the polymeric viscosity is the function of shear rate. The proposed polymeric viscosity is written as,

$$\mu_p = (\mu_{p,\infty} - \mu_{p,0}) \left[ \frac{1 + ln\big(1 + \kappa A\big)}{\big(1 + \kappa A\big)} \right] \tag{2.12}$$

the shear rate term, $A$, in the equation is defined as [23],

$$A = \left[ \frac{1}{2} tr\Big( \big[ (\nabla \mathbf{v} + \nabla \mathbf{v}^T) \big]^2 \Big) \right]^{1/2} \tag{2.13}$$

where $\mu_{p,\infty}$ is the polymeric viscosity at the infinite shear rate, $\mu_{p,0}$ is the polymeric viscosity at the zero shear rate, and $\kappa$ is the shear rate dependency term for the blood. The values for the polymer viscosity are taken from the experiments of Yeleswarapu [23] as, $\mu_{p,0} = 6.5\ mPa.s$, $\mu_{p,\infty} = 200\ mPa.s$, and $\kappa = 11.14\ s$. Also, the solvent part of the blood is modelled as a Newtonian fluid, and its contribution to the extra stress tensor is written as in the Eq. 2.9. The solvent viscosity is assumed as the infinite shear viscosity of the polymeric viscosity, in order to be consistent with the experiments of Thurston [20, 21] and the assumption of the blood viscosity tends to be Newtonian at high shear rates [18, 19, 77].

In addition to the polymeric viscosity selection, the stress relaxation time must be determined for the viscoelastic formulation. Although viscoelasticity of the whole blood and stress relaxation times have been widely studied in the literature [21, 23, 27, 78], some of the elastic properties defined in these studies have multiple modes [21, 27]. Since a single mode modified Oldroyd-B model is applied in this study, a relaxation time obtained for a single mode viscoelastic formulation is adopted as $\lambda_1 = 2.6\ ms$ from the study of Brust *et al.* [78].

## 2.3. Solid Domain Formulation

The aorta modelling has drawn the attention of many researchers [34–39]. The aorta consists of three layers (intima, media and adventitia) as shown in the Figure 2.4. An accurate model for aortic wall should take into account these three layers and the effects of anisotropy due to collagen fibers in the tissue. The anisotropic material models for the aortic vessel walls have been developed [36, 37, 39]. However, in the fluid solid interaction simulations the large arteries are often modeled as single layered, isotropic and linearly elastic [16, 61, 79], as well as hyperelastic [36, 39, 80].

Regardless of the material model, the movement of the vessels is governed by the following conservation of momentum equation,

$$\nabla \cdot \sigma_{\mathbf{s}} = \rho_s \ddot{\mathbf{u}}_{\mathbf{s}} \tag{2.14}$$

where $\sigma_{\mathbf{s}}$ is the solid stress tensor, $\rho_s$ is the density and $\ddot{\mathbf{u}}_{\mathbf{s}}$ is the local acceleration of the blood vessel. The arterial wall is assumed to be elastic and nearly incompressible with constant density of $\rho_s = 1120\ kg.m^{-3}$ [81]. The material model for the arterial wall affects the stress tensor similar to the rheological model selection in the fluid domain. The effects of wall compliance is investigated with the linearly elastic and hyperelastic Yeoh models and their results are compared with the rigid walled simulations in this study. The formulations for the solid stress tensor for these models are described in detail in the following subsections.

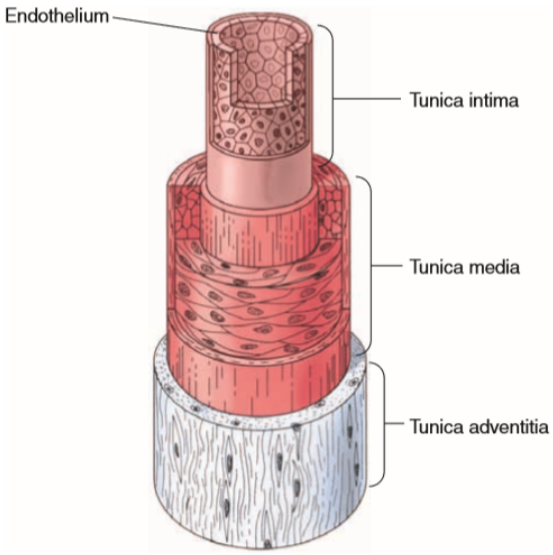


Figure 2.4. General structure of arteries. The major three layers (intima, media and adventitia) can be observed with the endothelial cells in the vessel [2].

### 2.3.1. Linearly Elastic Model

In the linearly elastic model, the elasticity of the vessel walls are independent of the strain rate, which is similar to the rheology of a Newtonian fluid whose viscosity is independent of shear rate. The stress tensor, $\sigma_{\mathbf{s}}$, for a linearly elastic solid can be written in the tensor and component forms, respectively.

$$\sigma_{\mathbf{s}} = \lambda_{\mathbf{s}}\mathbf{tr}(\varepsilon_{\mathbf{s}})\mathbf{I} + \mathbf{2}\mu_{\mathbf{solid}}\varepsilon_{\mathbf{s}} \tag{2.15}$$

$$\sigma_{\mathbf{ij}} = \lambda_s \varepsilon_{kk} \delta_{ij} + 2\mu_s \varepsilon_{ij} \tag{2.16}$$

where $\delta$ is the Kronecker delta operator, $\lambda_s$ and $\mu_{solid}$ are the Lamé coefficients, and $\varepsilon_s$ is the strain tensor for the solid component. The Lamé coefficients are obtained using the material properties, Young's modulus $E$ and Poisson's ratio $\nu$, and the formulation for the Lamé coefficients, $\lambda_s$ and $\mu_{solid}$, are shown in the Eq. 2.17 and 2.18, respectively. In this study, the elastic properties for the vessel wall, Young modulus and Poisson's ratio, are chosen as $E = 1\ MPa$ and $\nu = 0.48$, respectively [81].

$$\mu_{solid} = \frac{E}{2(1+\nu)} \tag{2.17}$$

$$\lambda_s = \frac{E\nu}{(1+\nu)(1-2\nu)} \tag{2.18}$$

### 2.3.2. Hyperelastic Yeoh Model

The rubber-like behavior of the blood vessels have been expressed with hyperelastic models in the literature [36, 39, 80, 82]. In this study, Yeoh model is selected to mimic the hyperelastic behavior of aortic walls, and the results are used to compare the effects of wall elasticity. In the Yeoh model, the strain energy density function is given in the study of Raghavan and Vorp [36]. The proposed strain energy density function, $W$ is,

$$W = \alpha(I_{\mathbf{B}} - 3) + \beta(I_{\mathbf{B}} - 3)^2 \tag{2.19}$$

where $\alpha$ and $\beta$ are the material parameters, and $I_{\mathbf{B}}$ represents the first invariant of the left Cauchy-Green tensor, $\mathbf{B}$, where $I_{\mathbf{B}}$ can be written as,

$$I_{\mathbf{B}} = \lambda_{s,1} + \lambda_{s,2} + \lambda_{s,3} \tag{2.20}$$

where $\lambda_{s,i}$ shows the stretch ratio in the eigenvector direction, $i$. The global coordinate system coincide with the eigenvector direction in this study, therefore the elements of the normal strains are related with the stretch ratios, and they can be expressed as,

$$\varepsilon_{ii} = \lambda_{s,i} - 1 \tag{2.21}$$

The strain energy density function is related with the solid stress tensor; the derivatives of $W$ with respect to components of the strain tensor result in the components of the solid stress tensor. Their relation can be written as,

$$\frac{\partial W}{\partial \varepsilon_{ij}} = \sigma_{s,ij} \tag{2.22}$$

The material parameters used in the study, to model the elastic behavior of the vessel walls, are obtained from non-invasive experimental study and are reported as $\alpha = 12.0\ N.cm^{-2}$ and $\beta = 90.0\ N.cm^{-2}$ [80].

## 2.4. Coupling Between the Fluid and Solid Domains

The coupling between the solid and fluid domains is performed using the continuity conditions at the interface of the blood and the vessel. These conditions can be explained as:

- The displacements of the fluid and the solid are compatible.
- The no slip boundary condition is applicable to the fluid domain.
- The stresses on the solid and fluid boundary are at the equilibrium.

The equations representing those conditions are written, respectively.

$$\mathbf{u_f} = \mathbf{u_s} \tag{2.23}$$

$$\mathbf{v} = \frac{D\mathbf{u_s}}{Dt} \tag{2.24}$$

$$\sigma_\mathbf{f} \cdot \mathbf{n_f} = \sigma_\mathbf{s} \cdot \mathbf{n_s} \tag{2.25}$$

where $\mathbf{u}$ is the displacement vector, $\sigma$ is the total stress tensor and $\mathbf{n}$ is the unit normal vector at the surface, and the subscripts s and f denote solid and fluid domains, respectively. In the rigid walled case, the solid displacement vector is written as $\mathbf{u_s} = 0$.

## 2.5. Non-Dimensional Numbers

In this study, the non-dimensional numbers are obtained using time averaged mean velocity. The numbers used in the study are Reynolds, Weissenberg and Elasticity numbers.

The Reynolds number is used to observe the ratio of the inertial effects to the viscous effects. The time averaged mean velocity based Reynolds number, $Re_{m,N}$, gives an insight on the overall behavior of the flow throughout the cardiac cycle, and it can be written as,

$$Re_{m,N} = \frac{2r_0\rho\bar{v}_m}{\mu_N} \tag{2.26}$$

where $\bar{v}_m$ is the time-averaged inlet velocity and $\mu_N$ is the reference Newtonian viscosity. For the given pulse in Figure 2.3, the Reynolds number is calculated as $Re_{m,N} = 300$ in resting conditions for the abdominal aorta, and the highest Reynolds number is 1732 at the peak systole ($t = 0.32\ s$), which is consistent with the laminar flow assumption used in the study.

The Weissenberg number is the ratio of the elastic forces to the viscous forces. It gives the insight on the dominance of the stress relaxation time of the fluid over the process time. Similar to the Reynolds number, the time averaged mean velocity is used in the calculation of the Weissenberg number, $Wi_m$, and it can be written as,

$$Wi_m = \lambda_1 \frac{\bar{v}_m}{r_0} \tag{2.27}$$

where $\lambda_1$ is the relaxation time of the fluid. Weissenberg number is calculated as $Wi_m = 0.02$ for the mean conditions, where the highest Weissenberg number is 0.1 at the peak systole ($t = 0.32\ s$).

The Elasticity number, $El_m$, characterizes the importance of the elastic effects in the inertial flows of viscoelastic fluids. The Elasticity number is defined as the ratio of the Weissenberg number to the Reynolds number. $El_m$ is independent of the shear rate, whereas it represents the relation between the time scale of the fluid relaxation to the viscous diffusion. The Elasticity number can be written as,

$$El_m = \frac{Wi_m}{Re_{m,N}} = \frac{\lambda_1 \bar{v}_m / r_0}{2 r_0 \rho \bar{v}_m / \mu_N} = \frac{\lambda_1 \mu_N}{2 \rho r_0^2} \tag{2.28}$$

It can be observed that for the same fluid properties, the elasticity number, is related with the flow geometry, $\sim 1/r_0^2$.

# 3. SOLUTION METHODS

All of the numerical simulations presented in the thesis are conducted using the finite element method based commercial software COMSOL Multiphysics v5.3a. The governing equations for the aforementioned fluid and solid domains are both coupled and non-linear. The coupled equations are solved with fluid solid interaction (FSI) method, where the fluid stress causes forces loading to the solid, as well as the walls transmit velocity to the fluid domain. Also, the displacements of the solid leads to expansion of the fluid domain and mesh deformations. The Arbitrary Lagrangian-Eulerian formulation is applied to deal with the deformations in the mesh, together with the fully coupled solution method. A flowchart representing the FSI methodology used in the study is given in Figure 3.1. Direct solution method is used for the solution of space discretized system of equations, rather than the iterative approach which is more time consuming.

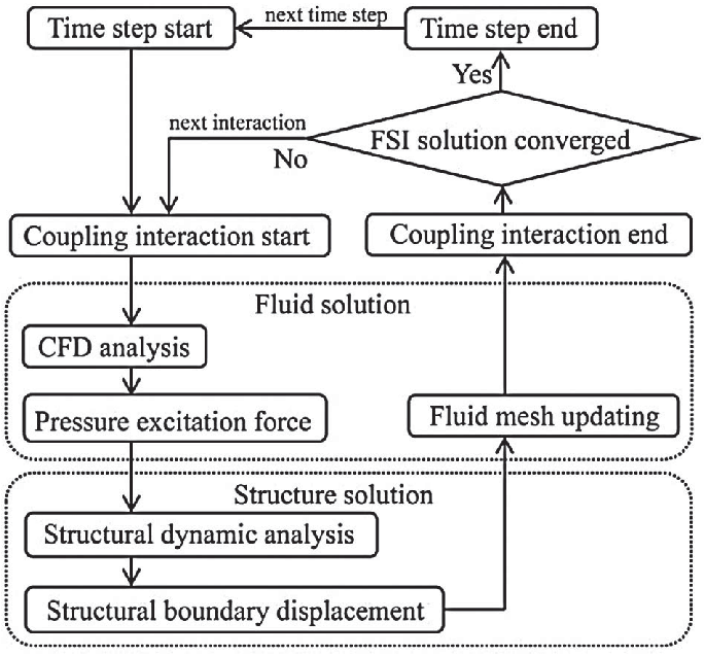


Figure 3.1. Flowchart representing the numerical methodology applied in the FSI simulations.

The solution methods applied for the numerical simulations in the study are covered in two subsections, since the methods differ with the problem. In the Section 3.1, the numerical methods used in the simulations of the investigation of effects resulting from the purely shear thinning fluid rheology and wall elasticity are given. The Section 3.2 introduces the solution methods applied in the numerical simulations to investigate the combined effects of the viscoelastic and shear thinning fluid rheology.

## 3.1. Newtonian and Carreau Simulations

The simulations in this subsection only consists of the Newtonian and Carreau models for the fluid rheology, and the rigid, linearly elastic and hyperelastic wall models for the arterial walls. The geometry and the applied boundary conditions are discussed in detail in the Section 2.1, and the geometric representation and the boundary conditions are shown in the Figures 2.1 and 2.3, respectively.

### 3.1.1. Interpolation Function and Stabilization Method Selection

In these simulations with the aforementioned fluid and solid models, quadratic interpolation functions are used for velocity and pressure variables in the fluid, displacement variables in the solid domains without using any stabilization techniques introduced in the COMSOL Multiphysics, as suggested by Khan *et al.* [83]. The first order interpolation functions for the mesh elements are tried to solve the problem with and without stabilization, and it is observed that the stabilized simulations underestimate the velocity values at the low shear rate. The comparison of the velocity values at the peak systole, end of the systole and late diastole, for first and second order interpolation functions with and without stabilization are given in the Figures 3.2, 3.3 and 3.4, respectively.

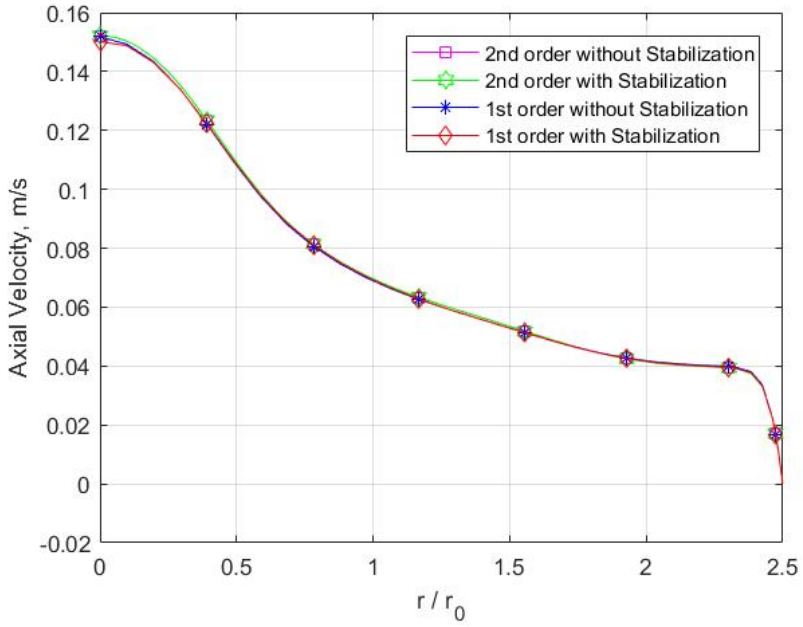


Figure 3.2. Comparison of velocity values at the center of AAA at the peak systole for the four different solution methods.

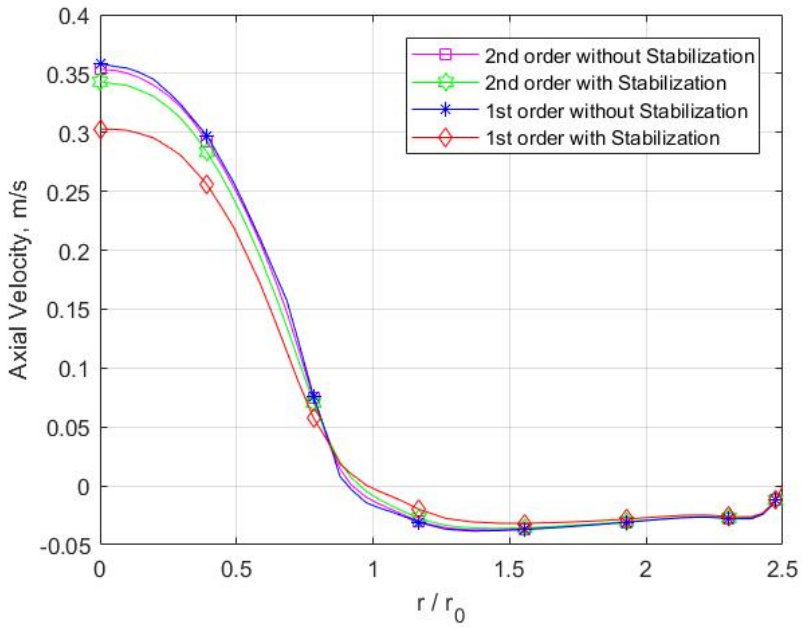


Figure 3.3. Comparison of velocity values at the center of AAA at the end of the systole for the four different solution methods.

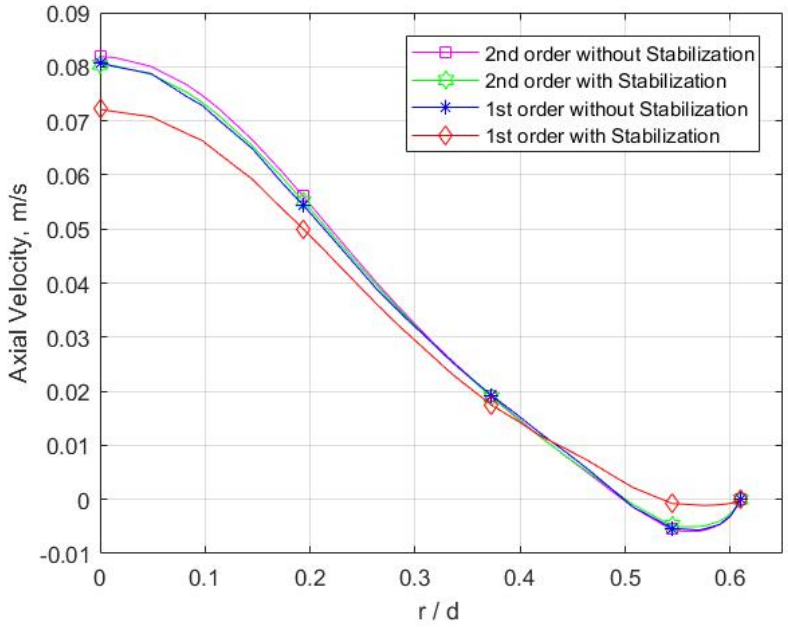


Figure 3.4. Comparison of velocity values at a section near the distal end of AAA at late diastole (t=0.75 s) for the four different solution methods.

It can be observed that the stabilization affects mainly the simulations performed using first order interpolation functions. At the peak systole, Figure 3.2, all four solutions yield very close velocity values, whereas at the end of the systole, Figure 3.3 and late diastole, Figure 3.4, the stabilized first order method underestimates the velocity values near the center of the vessel compared to other solution methods. Therefore, all of the simulations are performed by using second order interpolation without using any stabilization.

### 3.1.2. The Convergence Criterion

The convergence criterion is set in terms of an absolute tolerance less than $10^{-4}$. The time integration algorithm is chosen as adaptive and implicit Backward Differentiation Formulas (BDF) method with a time step of the order of $10^{-3}$.

Meshes on the solid and the fluid domains are generated separately. In the solid domain, only triangular mesh elements are used, whereas the fluid domain is meshed with both triangular and quadratic elements. Two rows of quadratic elements are placed at the near vicinity of the blood vessel to capture large gradients in the boundary layer. Three different meshes are tried, named as Mesh 1 , Mesh 2 and Mesh 3, with the total element numbers of 6,300 (5,300 + 1,000), 15,700 (12,100 + 3,600) and 18,000 (13,200 + 4,800), respectively . The first number in the brackets is the number of elements in the fluid domain, whereas the second number represents the number of elements in the solid domain. The corresponding degrees of freedom for these meshes are, 63,300, 151,000 and 181,000. A portion of the computational grid corresponding to Mesh 2 is given in Figure 3.5.

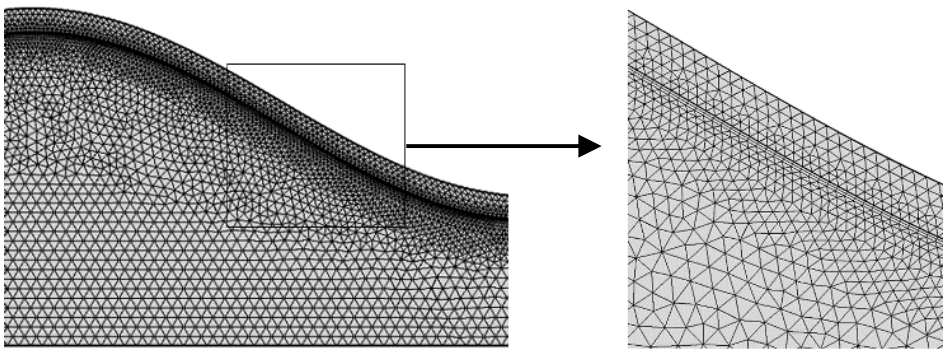

Figure 3.5. A portion of computational grid with 15,700 elements.

Mesh independency tests are performed for each rheological and wall models using the boundary conditions shown in the Figure 2.3. Non-Newtonian flow simulations require lower degree of freedom for mesh independent solution, since the lower shear rate in the flow separation regions leads to higher viscosity values having a numerically stabilizing effect as discussed [66]. Figures 3.6 and 3.7 represent the velocity profiles at two time instances and the wall displacement values throughout the cardiac cycle for the mentioned three meshes, respectively. The least square percentage differences in several output parameters are listed in Table 3.1. The difference in the converged values for all variables are found to be less than 1.0% for Mesh 1 and Mesh 2. According to these results, Mesh 2 is chosen and used to perform all flow simulations in this study.

The average simulation time for the hyperelastic wall model is $\sim$ 52 CPU-hours with Intel Xeon E5320 processors.

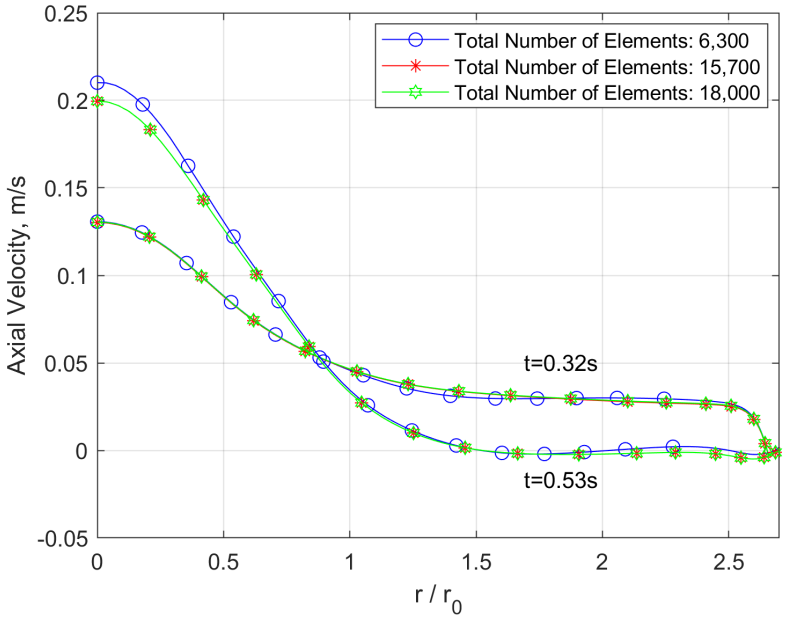


Figure 3.6. Axial velocity at the center of the AAA for the three different meshes.

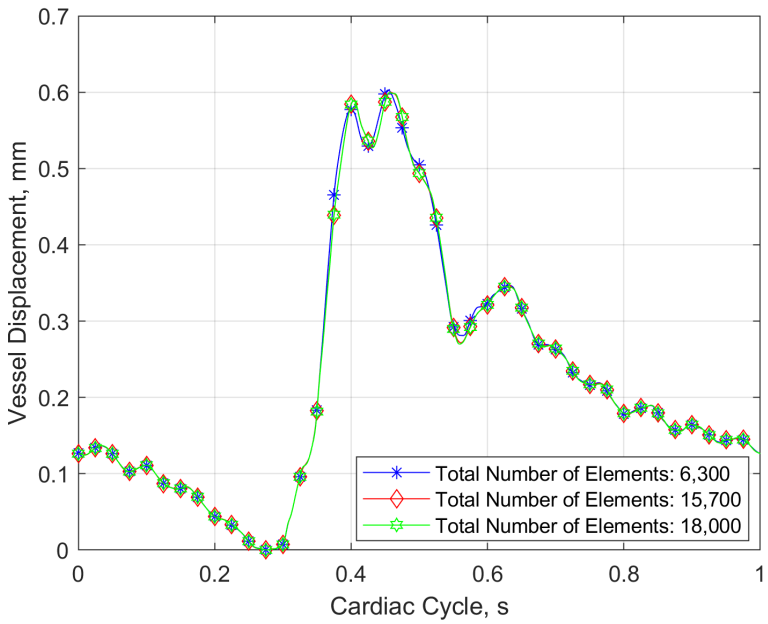


Figure 3.7. Wall displacement at the center of the AAA throughout the cardiac cycle.

Table 3.1. The least square percentage differences between the selected meshes.

| | **Mesh 1-Mesh 2** | **Mesh 2-Mesh 3** | **Mesh 1-Mesh 3** |
|---|---|---|---|
| **Velocity at the peak systole** | 0.0 % | 0.1 % | 0.1 % |
| **Velocity at the end of systole** | 0.5 % | 0.7 % | 0.5 % |
| **WSS at the peak systole** | 0.0 % | 0.0 % | 0.1 % |
| **Cyclic vessel displacement** | 0.1 % | 0.2 % | 0.2 % |
| **Time averaged von Mises stress** | 0.1 % | 0.2 % | 0.2 % |
| **TAWSS** | 1.0 % | 3.2 % | 3.3 % |
| **OSI** | 0.6 % | 1.2 % | 1.4 % |

### 3.2. Modified Oldroyd-B Simulations

The governing equations for the fluid and solid domains, as well as the extra stress tensor are coupled and non-linear, as previously mentioned in the Section 3.1. The elastic stress tensor and its evaluation equations are introduced to the COMSOL Multiphysics software by using a user defined function. The finite element formulation for the viscoelastic flows are given in detail in [84]. The space discretized system is solved with direct solution method by using second order interpolation functions for the velocity and the displacement fields, and first order functions for the pressure and the elastic stress terms. The least square stabilization technique for the elastic stress components, which is important to achieve the numerically stable solutions at high Weisenberg numbers [85], is applied for the elastic stress equations. The formulation of the least square Galerkin stabilization method is explained in detail in the study of Behr *et al.* [86].

### 3.2.1. Convergence Criterion

The convergence criterion for all variables are set in terms of an absolute tolerance as $10^{-5}$. The time integration algorithm is adaptive and implicit Backward Differentiation Formula with a time step order of $10^{-5}$.

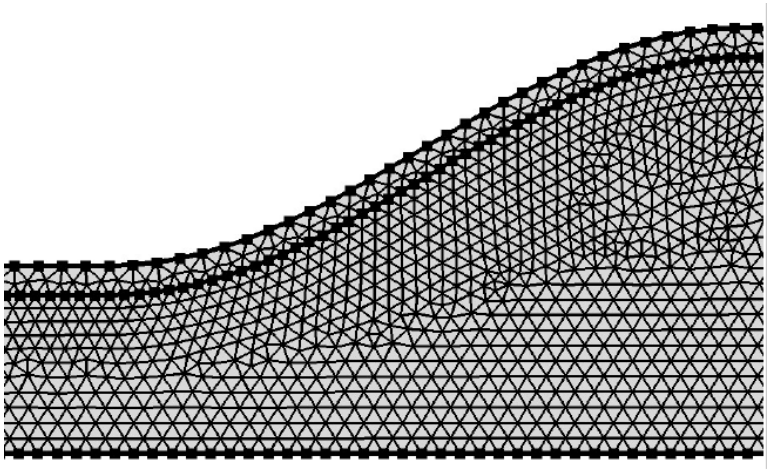

Figure 3.8. A portion of computational grid used in the viscoelastic fluid simulations.

Triangular mesh elements are used for the simulations of the modified Oldroyd-B model, since the quadratic meshes are incompatible with the least square stabilization technique. Therefore, both the fluid and solid domains are meshed with triangular elements. The mesh independency tests are done for each reported case by performing simulations with three different meshes. The highest number of mesh elements required to have a numerical convergence is found to be the case of viscoelastic fluid model with elastic walls. The meshes tried for the case have the total element numbers of (7183 + 1356), (4473 + 1049) and (3695 + 751), named as Mesh 1, Mesh 2 and Mesh 3, respectively. The first number in the brackets is the number of elements in the fluid domain, whereas the second number represents the number of elements in the solid domain. The corresponding degrees of freedom for these meshes are, 86,500, 55,500 and 46,000. Figure 3.9 shows the velocity profiles along the center of the aneurysm at two time instances, and it can be observed that the velocity profiles of Mesh 1 and Mesh 2 are similar to each other, whereas the coarsest mesh, Mesh 3, displays different profiles for the velocity. Therefore, the Meshes 1 and 2 are used to investigate the differences in

the output parameters and Mesh 3 is omitted. The least square differences of several output parameters are listed in Table 3.2. The difference in output parameters are found to be less than 0.9 % for Mesh 1 and Mesh 2, and Mesh 1 is selected to perform the simulations. The computational domain with the Mesh 1 is given in Figure 3.8. The average simulation time for the viscoelastic fluid in the elastic walled model is ∼750 CPU-hour with Intel Xeon W-2155 processor.

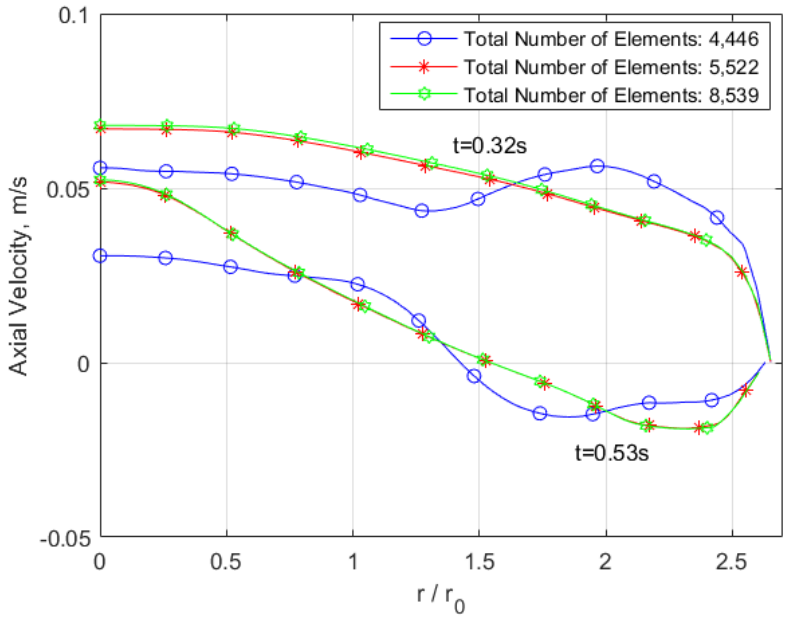


Figure 3.9. Axial velocity for the viscoelastic fluid model at the center of the AAA for the selected meshes.

Table 3.2. The least square percentage differences between Mesh 1 and Mesh 2.

| | **Mesh 1 - Mesh 2** |
|---|---|
| **Velocity at the peak systole** | 0.9 % |
| **Velocity at the end of systole** | 0.4 % |
| **WSS at the peak systole** | 0.5 % |
| **TAWSS** | 0.0 % |
| **OSI** | 0.3 % |

# 4. TESTS AND VALIDATIONS

Numerical tests are performed to validate all of the models used in the study with their corresponding solution methodology. The Newtonian model is compared with both the experimental and numerical results of Budwig *et al.* [17] in Section 4.1. The transient behavior of the flow and the shear thinning Carreau model is compared with the study of Khanafer *et al.* [57] in Section 4.2. The compliant wall models are compared with the displacement values reported by the clinical observations of Malina *et al.* [87] in the Section 4.3. The viscoelastic model is compared with the experimental results of Yeleswarapu *et al.* [24], and a numerical benchmark for 1:4 contraction geometry is given in the Section 4.4 .

## 4.1. Newtonian Model for Newtonian Case

Transparent and dilated pipes are used by Budwig *et al.* [17] in order to capture the velocity profile inside an aneurysm. In their experiments, a Newtonian fluid containing silica beads is used with particle image velocimetry to capture the velocity field. Figure 4.1 represents a comparison of the axial velocity profile at the center of the aneurysm with both the experimental and numerical results of Budwig *et al.* [17] for the steady flow of a Newtonian fluid in a rigid walled axisymmetric aneurysm geometry. Least square error between the present numerical analysis and the numerical results is 0.9% whereas the maximum error between the present numerical results and the experimental results is 9.7% in the Figure 4.1.

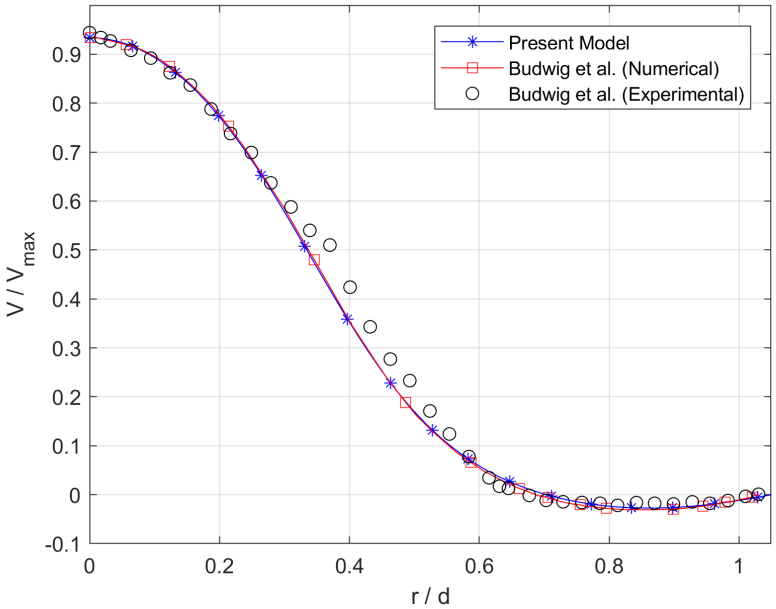


Figure 4.1. Comparison of steady Newtonian profile across the center of the AAA ($Re = 400$, $R/r_0 = 2.1$, $L/r_0 = 8$) [17].

## 4.2. Carreau Model for Pulsatile Case

The pulsatile flow model is compared and validated with the numerical results of Khanafer *et al.* [57] for a non-Newtonian Carreau fluid in a rigid walled vessel with aneurysm at the instances of peak and end systole, in terms of the axial velocity profile across the center of AAA, given in Figure 4.2 where the average errors between the present study and the results of Khanafer *et al.* [57] are 3.0% and 0.9% for peak and end systole, respectively. Also, the wall shear stress (WSS) profile comparison with the same study is given in Figure 4.3 for the peak systole and the average error is found to be 4.1%.

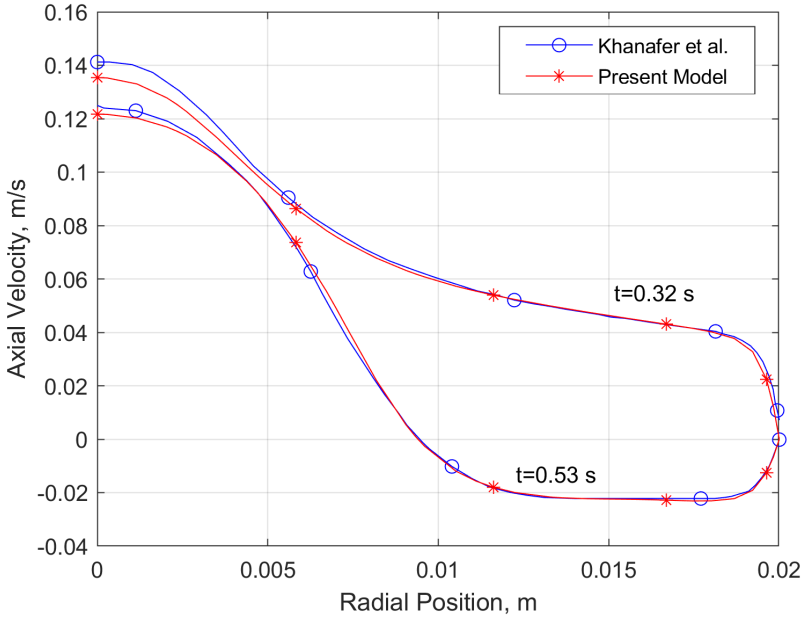


Figure 4.2. Comparison of Carreau model velocity profiles under pulsatile conditions at the center of the AAA ($Re_{m,N} = 300,\ R/r_0 = 2.5,\ L/r_0 = 8$) [57].

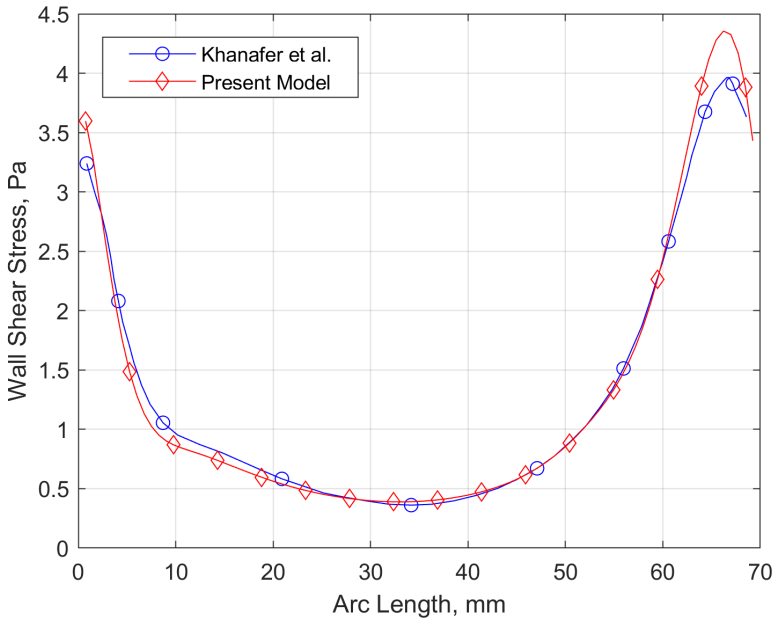


Figure 4.3. Comparison of WSS on the aneurysmal arc for Carreau model at the peak systole ($Re_{m,N} = 300,\ R/r_0 = 2.5,\ L/r_0 = 8$) [57].

### 4.3. Wall Elasticity Models

The displacements of the aortic wall are compared with the measurements of Malina *et al.* [87] obtained using ultrasound imaging techniques for the enlargement of abdominal aortic aneurysms under resting conditions. The pulsatile wall motions in our study are found to be similar in the time variation trend of the displacement, as shown in Figure 4.4, and the displacement values are in the expected range given in the clinical study of Malina *et al.* [87]. In their study, the average displacement values of the wall motion are given for a patient with an abdominal aortic aneurysm of dilated radius $R = 25mm$, where the maximum strain corresponds to 0.019. The variability in wall displacement measurements in AAA was mentioned to be 22%, therefore for their study, the maximum strain at the center of an AAA is between 0.015-0.023 under resting conditions. In our computational model, the maximum strains are 0.015 for hyperelastic model and 0.019 for the linearly elastic model.

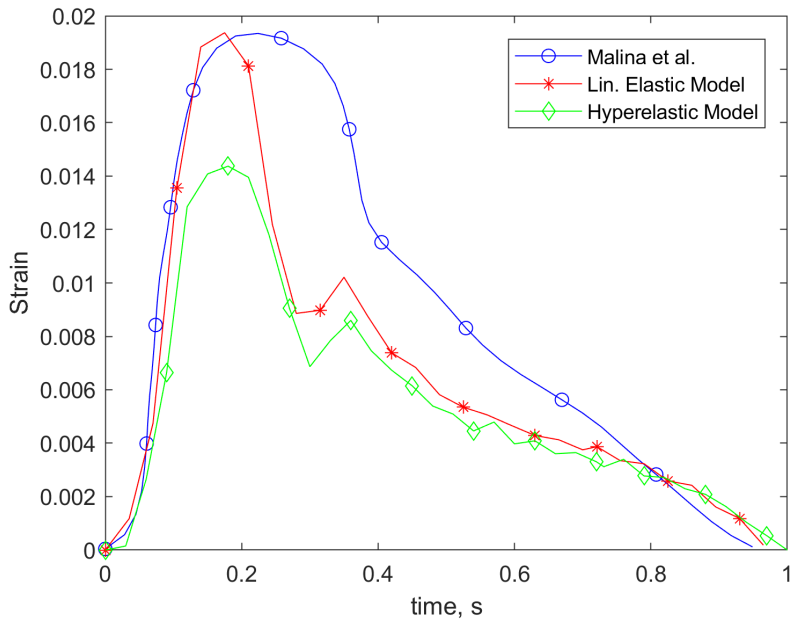


Figure 4.4. Comparison of the strain values for different wall models and clinical observations of Malina *et al.* [87].

### 4.4. Viscoelastic Fluid Models

The generalized Oldroyd-B model has been adopted from Yeleswarapu *et al.* [23], and the numerical results for the model has been compared with their experiments. Yeleswarapu *et al.* [24] conducted experiments with porcine blood for steady flow in a circular pipe at three different Reynolds numbers (Re=16, 20, and 25) and compared the measured velocity profiles with the numerical predictions obtained from Newtonian and the modified Oldroyd-B model. They showed that the modified Oldroyd-B model matches well with the experimental results and it is suitable to simulate blood flow. Rheological models used in this study, namely Newtonian and generalized Oldroyd-B together with shear thinning Carreau and Power-Law and shear thinning viscoplastic Casson model with yield stress which are also used in blood flow simulations in the literature, are compared with the experiments in [24] at the same conditions. The deviations of the centerline velocity values from the experimental results can be observed in Table 4.1, where the generalized Oldroyd-B model appears to be in good relation with the experimental values, and the results of this model are closer to the experimental results compared to the proposed model of the Yeleswarapu *et al.* [24] in the higher Reynolds numbers. When the viscoelastic properties of the blood are not considered, the Carreau model appears to be the most suitable model to mimic the shear thinning behavior of the blood with respect to the experiments of Yeleswarapu *et al.* [24].

Table 4.1. Deviation of centerline velocities from the experiments [24].

| | **Newtonian Model** | **Casson Model** | **Carreau Model** | **Yeleswarapu's Model [23]** | **Present Model** |
|---|---|---|---|---|---|
| ***Re=16*** | 38.3 % | 27.0 % | 20.9 % | 0.9 % | 1.7 % |
| ***Re=20*** | 37.0 % | 28.2 % | 20.8 % | 1.0 % | 1.4 % |
| ***Re=25*** | 43.9 % | 37.5 % | 27.9 % | 7.5 % | 4.4 % |

In addition to the experiments of Yeleswarapu *et al.* [24], the viscoelastic model is compared with the benchmark 1:4 contraction geometry. The elastic viscosity part is taken as constant which reduces the formulation to classical Oldroyd-B model. The

results of the contraction flow simulations are found to be in good agreement with the results in the literature. The components of the extra stress tensor at the contraction are given in the Figure 4.5, and these components are compared with the results of Meng *et al.* [88]. The present model shows similar extra stress values to the results of Meng *et al.* [88], when $Re \sim 0$ and $Wi = 0.1$.

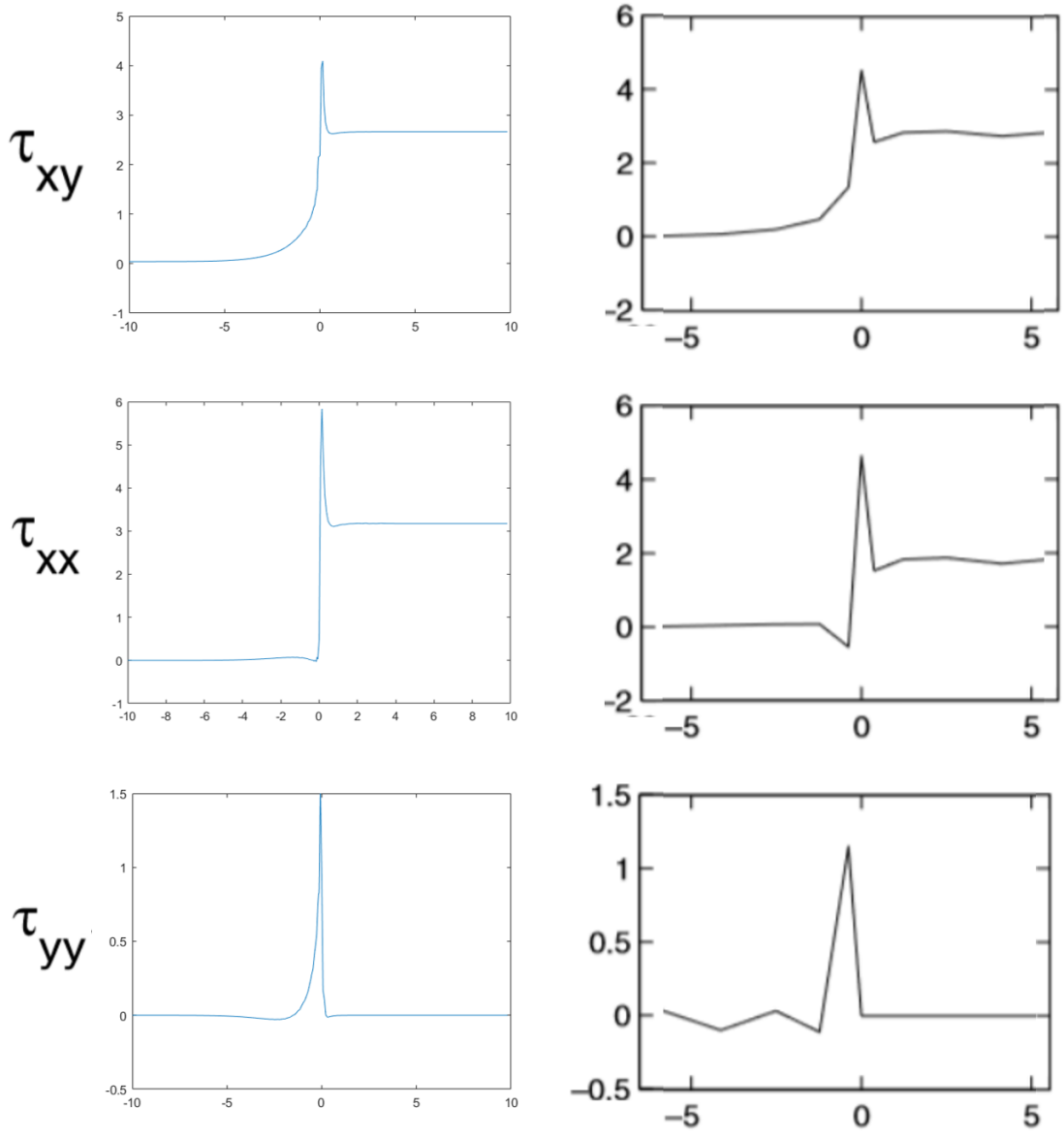


Figure 4.5. Comparison of the polymeric extra stress values with the results of Meng *et al.* [88].

In addition to the extra stress components, the change of the corner vortex length with the Weissenberg number is compared with the results of Sato and Richardson [89] and Alves *et al.* [90] in the Table 4.2, and the length of the corner vortex and its decrease with the increasing Weissenberg number have been found to be in a good agreement with their results.

Table 4.2. The length of the corner vortex for different Weissenberg ($Wi$) numbers.

| ***Wi*** | **Present Model** | **Sato and Richardson [89]** | **Alves *et al.* [90]** |
|---|---|---|---|
| 0 | 1.48 | 1.45 | 1.50 |
| 0.1 | 1.48 | 1.43 | - |
| 0.2 | 1.47 | 1.42 | - |
| 0.3 | 1.46 | 1.38 | - |
| 0.5 | 1.44 | 1.40 | 1.45 |

# 5. RESULTS AND DISCUSSIONS

The results of purely shear thinning effects and the wall elasticity are covered in the Section 5.1, and the combined effects of shear thinning and viscoelasticity are given in the Section 5.2.

## 5.1. Investigation of Purely Shear Thinning Effects

The results presented in this section are obtained by performing numerical simulations with three different wall models for the vessel (rigid, linearly elastic and hyperelastic) and two different rheological models for blood (Newtonian and Carreau) under pulsatile flow conditions corresponding to $Re_{m,N} = 300$. Differences in axial velocity, wall shear stress and vortical structures based on the blood rheology with different vessel wall elasticity are discussed in the Section 5.1.1. The effects of wall model elasticity in terms of displacement and von Mises stress are shown in the Section 5.1.2, and the differences in the rupture risk indicators, OSI and TAWSS are given in the Section 5.1.3.

### 5.1.1. Effects of Blood Rheology

Axial velocity profiles at the center of aneurysm are shown for the three wall models in Figures 5.1a, 5.1b and 5.1c for rigid, linearly elastic and hyperelastic wall models, respectively. When the fluid-solid interaction is taken into account in the elastic wall case, the vessels expand under the fluid pressure, therefore the velocities are slower with respect to the rigid walled case. At the peak of the systole ($t = 0.32\ s$), the velocity profiles for both rheological models have similar values in the near vicinity of the wall. Also, the Newtonian fluid overestimates the velocity values around 25% with respect to the Carreau fluid for all wall models through the center of the vessel due to the decrease in the shear rate, and the difference decreases from rigid walled case to hyperelastic walled case. At the end of the systole ($t = 0.53\ s$), similar to the peak systole, the Newtonian model shows higher velocity values near the centerline. This

difference between rheological models increases in the elastic walled simulations with respect to the rigid walled model, whereas this behavior is reversed for the instance of the peak systole. Hyperelastic simulations display higher velocity values for the Newtonian fluid compared to Carreau fluid at the end of the systole ($t = 0.53\ s$) in the near vicinity of the wall. However, simulations performed using the two other wall models, rigid and linearly elastic, yield smaller velocity values for the Newtonian fluid compared to Carreau fluid in the aneurysmal cavity and the Newtonian model displays higher velocity values near the center of the vessel where the shear rate decreases.

The wall shear stress values at the peak of the systole for rigid and linearly elastic vessel wall and different rheological models are compared in Figure 5.2 where straight and dashed lines represent rigid and linearly elastic walled models, respectively. The wall shear stress values of hyperelastic Yeoh and linearly elastic models are found to be similar as the maximum deviation between the values are found as 5.1% at the proximal end, therefore the results of Yeoh model is not shown on the figure. In the rigid walled case, different rheological models yield similar wall shear stress values, whereas at the proximal end the deviation between the models is 6.0% and the maximum deviation (10.4%) occurs at the distal end of the aneurysm between Carreau and Newtonian models. In the elastic wall model, the wall shear stress decreases with respect to the rigid walled case, as a result of structural response. Newtonian model yields lower shear stress values compared to the shear thinning model along the blood vessel. At the proximal end, there is a 11.1% difference and at the distal end the difference is 12.7% for the stress values between the Carreau and Newtonian models.

In the pathological sense, Malek *et al.* [11] stated that wall shear stress values of $\sim$2 Pa are suitable for maintaining the structure of arterial vessel and a lower shear stress value leads to the degeneration of endothelial cells. It can be observed in Figure 5.2 that wall shear stress (WSS) values are lower than 2 Pa in the middle section of the aneurysmal wall for all the studied models in both the rigid and elastic walled cases. Although the shear stress values are increased above 2 Pa for the rigid walled case at the proximal and distal ends of the aneurysm, they are much lower in the elastic walled case, especially at the distal end which is an indication for degeneration and

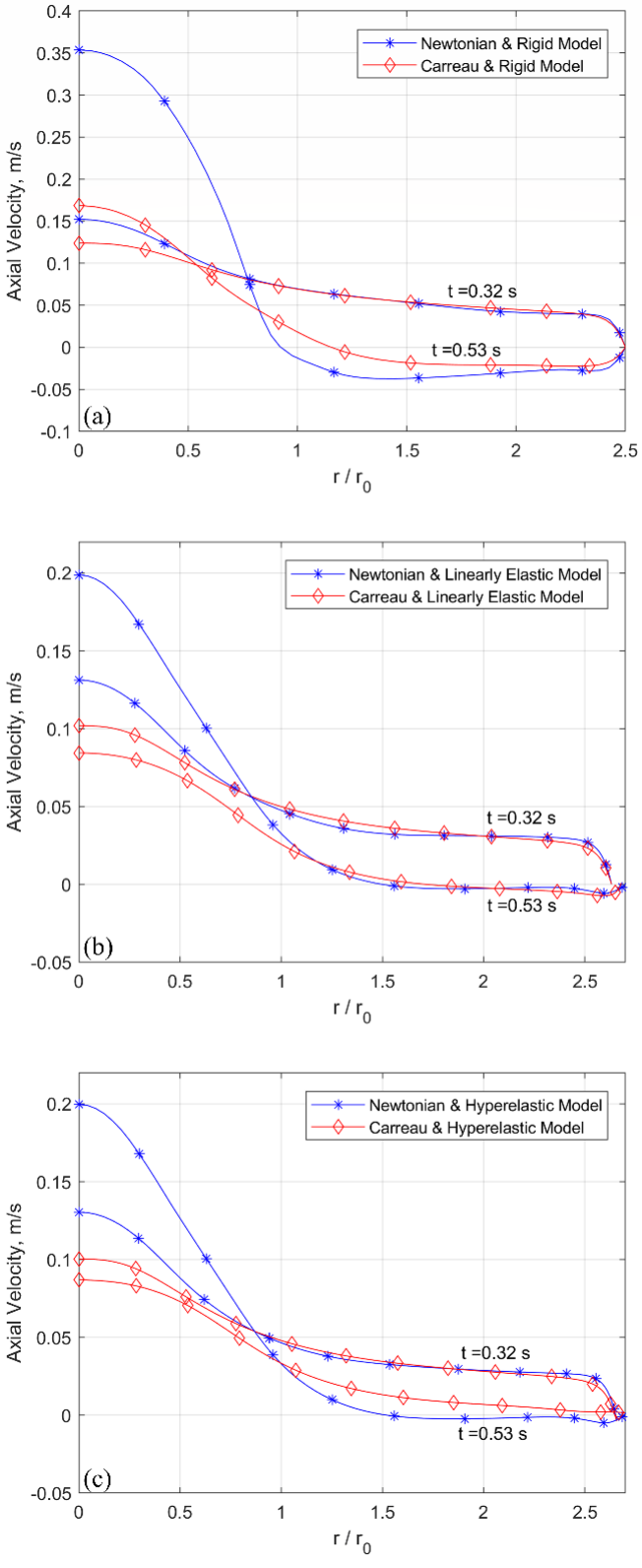


Figure 5.1. Axial velocity profiles at the center of AAA for (a) rigid walled model, (b) linearly elastic model, (c) hyperelastic model.

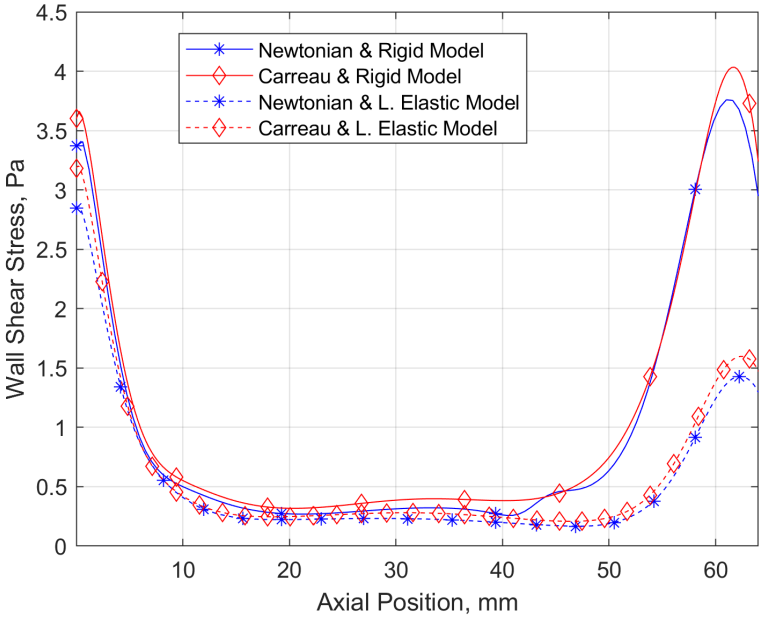


Figure 5.2. WSS Comparison for different rheological and structural models at the peak systole.

risk of arteriosclerosis. It can be deduced from rigid wall model simulations that the wall shear stress increases as the stiffness of the vessels increase.

Streamlines in the aneurysm at five different time values in the cardiac cycle, presented in Figure 2.3, including the instances of first deceleration ($t = 0.21\ s$), peak systole ($t = 0.32\ s$) and end of systole ($t = 0.53\ s$) are shown in Figures 5.3 and 5.4 for the Newtonian and Carreau models, respectively. The streamlines are colored with respect to the velocity magnitude, and the highest velocity values in the aneurysmal cavity are observed near the centerline, also the axial position of the primary vortex is near the highest velocity magnitude in the aneurysm. The patterns for the Newtonian model with rigid walls are consistent with the experimental study of Egelhoff *et al.* [51] which shows that a primary vortex is formed at the proximal end of the AAA as the flow decelerates after the peak systole, and the vortex shifts to the distal end towards the end of the cardiac cycle.

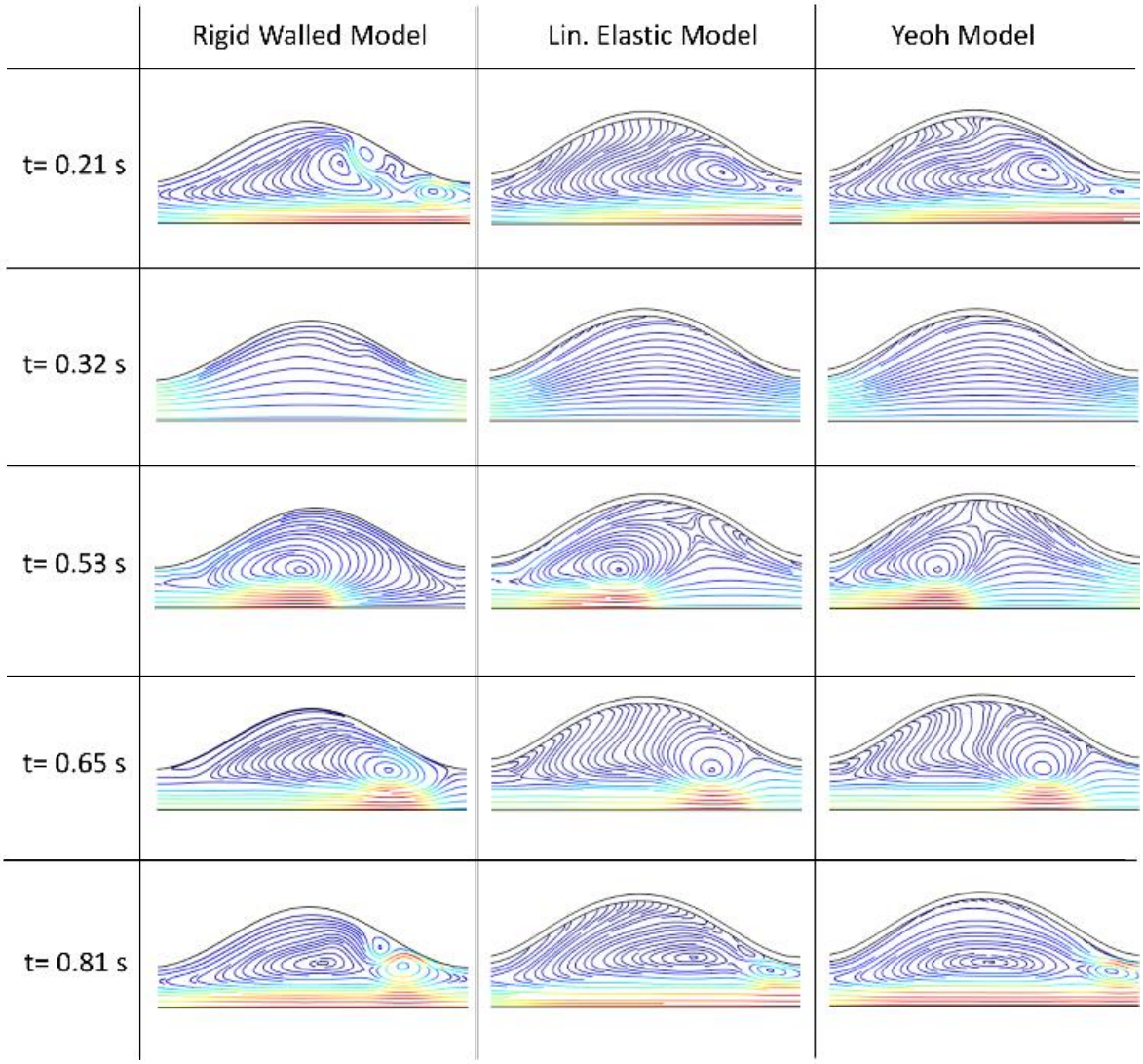


Figure 5.3. Streamlines for the Newtonian model with different wall models.

For the rigid wall case, at $t = 0.21\ s$ (first deceleration), both Newtonian and Carreau models yield a primary vortex near the distal end and a secondary counter rotating vortex near the center of the cavity, whereas Newtonian model shows an additional vortex near the aneurysmal wall which is co-rotating with the primary one. At the peak systole moment ($t = 0.32\ s$), the streamlines indicate fully attached flow for all rheological models. After the end of systole ($t = 0.53\ s$), a single vortex is formed and translates from proximal end to distal end in both rheological models similar to the experiments [51]. In the shear thinning model the vortex center has a tendency to shift towards the proximal end similar to the literature [91].

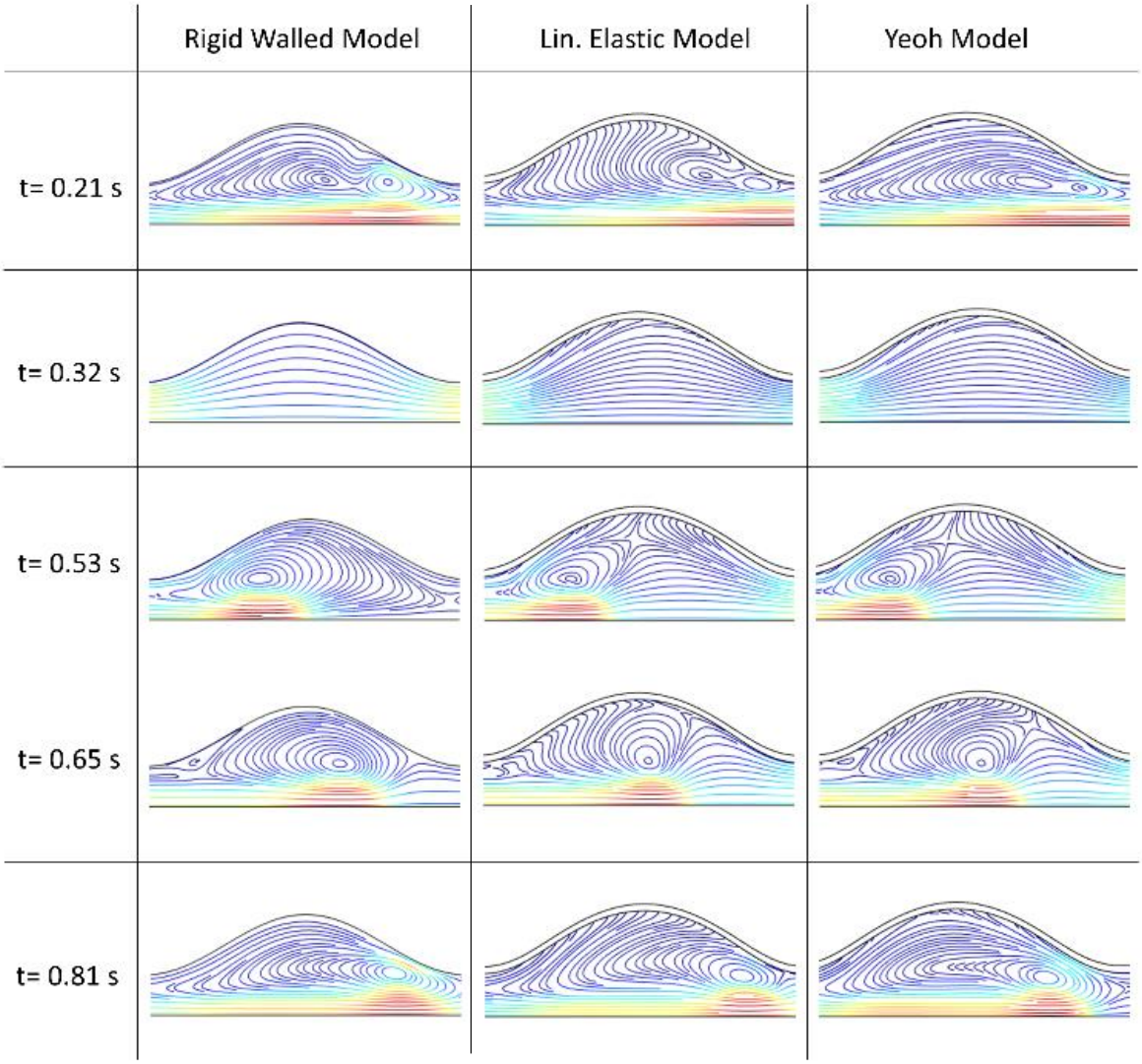


Figure 5.4. Streamlines for Carreau model with different wall models.

For the elastic walled cases, vortices are smaller compared to rigid walled case. The vortical structure and vortex translation are similar to the rigid walled case for both rheological models, whereas the vortices are observed to shift through the centerline of the blood vessel with respect to rigid wall model, from the peak systole to the end of the cardiac cycle. At the first instance of deceleration ($t = 0.21\ s$) Carreau model displays two co-rotating vortices near the distal end of the aneurysm where the primary vortex is located through the center of the cavity and the secondary one is located near the wall. On contrary, the secondary vortex is counter rotating in the Newtonian model. At the peak systole ($t = 0.32\ s$), both rheological models exhibit fully attached flow

for all wall models, therefore the peak systolic flow appears to have a neutral impact on vortical structure when compared to early and late diastolic flows which have more impact. After the systolic phase ($t > 0.53\ s$), the primary vortex shifts through the center of the aneurysm similar to the rigid walled models. Different elastic wall models do not affect the blood flow significantly in terms of vortical structure.

### 5.1.2. Effect of Wall Model Elasticity

The effect of blood rheology is found to be negligible ($< 0.1\%$) on the von Mises stress and the displacement of the vessel, therefore only the results of the Carreau model are used in this subsection. Differences in the displacement of the vessel wall are investigated by selecting three points on the aneurysm. In Figure 5.5a these points are shown and in the Figures 5.5b, 5.5c and 5.5d, the periodic displacements of these points under resting conditions are given. The displacement values of the center of the AAA (point #2) for both wall models are found to be within the expected values compared to the observations of Malina *et al.* [87] during the ultrasound imaging of an AAA. Pulsatile displacements follow the trend of the outlet pressure waveform. Yeoh model yields lower displacement values compared to the linearly elastic model.

Time averaged von Misses stress values along the aneurysm for both wall models are shown in the Figure 5.6. Except the central region of the aneurysm, both linearly elastic and Yeoh model yield the same trends with a difference of $\sim$80kPa. The difference between the models at the center of the cavity is similar with the results of Raghavan and Vorp [36] for the steady Newtonian flow. In the literature, the rupture of an AAA generally occurs at the ends [92], consistent with the fact that the distal and proximal ends are exposed to higher stress values than the center of the aneurysm.

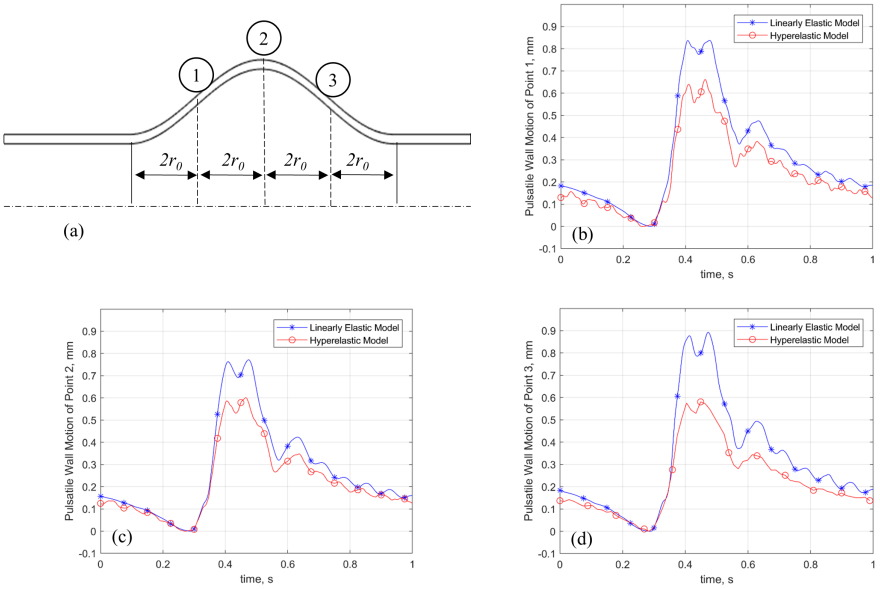


Figure 5.5. (a) Selected points on the vessel wall, and pulsatile wall motion of (b) point #1, (c) point #2, (d) point #3.

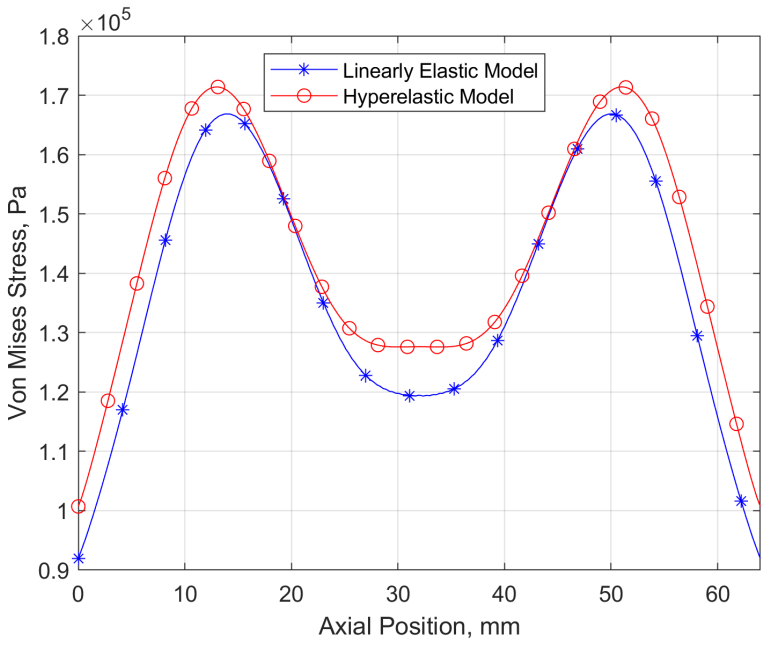


Figure 5.6. Comparison of von Mises stress values for linearly elastic and Yeoh models.

### 5.1.3. Risk indicators

Due to the nature of pulsatile flow, the pressure gradient at the inlet is oscillating. This behavior leads to periodic oscillations in the direction of wall shear stress and high oscillations lead to degeneration of the vessel tissue. The oscillatory shear index (OSI), is defined as [73],

$$OSI = \frac{1}{2}\left[1 - \frac{|\int_0^T \mathbf{WSS} dt|}{\int_0^T |\mathbf{WSS}| dt}\right] \tag{5.1}$$

This index is used to determine the deviations in the wall shear stress vector from its average direction by monitoring the changes in the magnitude and direction of the stress vector. $T$ denotes the period of the pulsatile flow at the inlet which is fixed as $T = 1\ s$ for this study. The OSI value varies from 0 to 0.5. Zero OSI denotes there is no change in the direction of the vector and OSI equal to 0.5 denotes the 180-degree deviation from the average direction.

OSI distributions on the aneurysm corresponding to Newtonian and Carreau models at resting conditions for both linearly elastic and hyperelastic modelled walls are shown in the Figures 5.7.a and 5.7.b, respectively. Although the intraluminal thrombus is neglected in this study, studies in the literature have shown that the average value of OSI increases very slightly ($\sim$0.01) when it is included [69].

Glor *et al.* [93] reported endothelial function, i.e. healthy elastic behavior of the vessels, is maintained under 0.20 OSI, physiologically. As shear thinning properties are taken into account, high OSI values tend to increase with respect to Newtonian model. The average OSI value increases by 0.05 for linearly elastic model and 0.07 for hyperelastic model. Also the total percentage of the distribution for high OSI ($>$0.20) increases by 10.7% and 23.1% for linearly elastic and hyperelastic models, respectively. The total percentage of high oscillatory shear stress increases by 19.5% for hyperelastic model when compared to linearly elastic model using Carreau fluid.

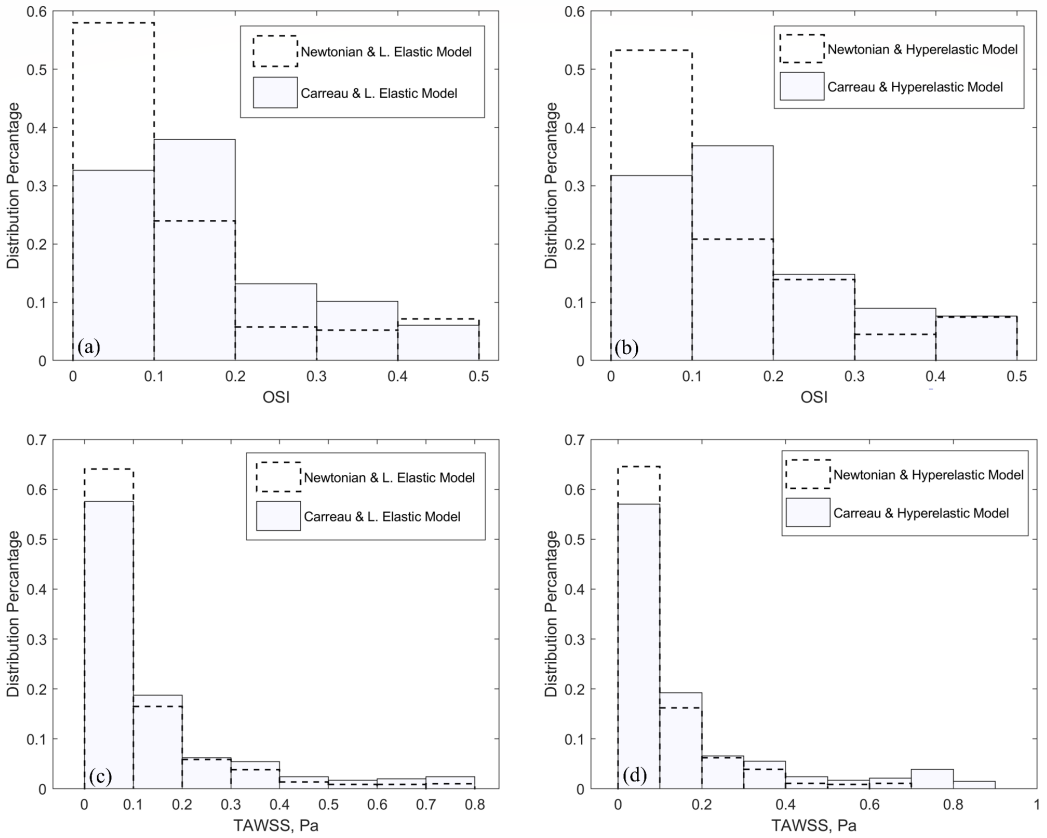


Figure 5.7. Percentage distribution of risk indicators on aneurysmal wall, (a) OSI for linearly elastic model, (b) OSI for hyperelastic model, (c) TAWSS for linearly elastic model, (d) TAWSS for hyperelastic model.

As discussed by Ku *et al.* [73] this increase in the OSI may lead to changes in the orientation of endothelial cells and arteriosclerosis which may result in rupture. In addition to OSI distribution, time-averaged wall shear stress (TAWSS) percentage distribution on the aneurysm are displayed in Figures 5.7c and 5.7d for linearly elastic and hyperelastic models, respectively. As reported by Kawaguchi *et al.* [12] ruptured cerebral aneurysms have lower shear stress values than non-ruptured ones. According to their results, at the point of rupture TAWSS is lower and it has the mean value of 0.49 Pa. As shear thinning properties are taken into account, regions experiencing low TAWSS slightly increase for the hyperelastic walled model with respect to Newtonian model. The total percentage of the low TAWSS distribution ($< 0.49\ Pa$) increases by 0.5% for the hyperelastic model, whereas the low TAWSS distribution decreases very

slightly ($< 0.1\%$) for the linearly elastic model. The total percentage of low TAWSS is affected very slightly ($< 0.1\%$) when hyperelastic and linearly elastic models compared for Carreau fluid. Therefore, the assumption of the Newtonian fluid, as well as linearly elastic wall, may predict much lower risk compared to non-Newtonian Carreau fluid combined with hyperelastic wall assumptions.

## 5.2. Investigation of the Combination of Shear Thinning and Viscoelastic Effects

The combined effects of shear thinning and elasticity on blood rheology,are investigated in this section. The simulations are performed by using modified Oldroyd-B, Carreau and Newtonian models for the fluid rheology, and two wall models (rigid and linearly elastic) for the computational domain given in the Figure 2.2. The boundary conditions applied to the computational domain are introduced in the Section 2.1, and the average Reynolds number corresponding to the inlet condition is $Re_{m,N} = 300$. The differences in the results of the viscoelastic and Newtonian models are shown to reveal to show the possible misestimation of the Newtonian fluid assumption. Also, the Carreau and modified Oldroyd-B model results are compared to observe the effects of the elastic nature of the blood. The results are presented in a similar order as in the Section 5.1, the effects of fluid rheology for different vessel walls are discussed in terms of axial velocity, wall shear stress and vortical structures in the Section 5.2.1. The differences in the rupture risk indicators, OSI and TAWSS are given in the Section 5.2.2.

### 5.2.1. Effects of Blood Rheology

The axial velocity profiles at the center of the aneurysm cavity are shown in the Figures 5.8 for the rigid walled model with the three rheological models. The Figures 5.8a and 5.8b represent the peak and end systole time instances, respectively. The shear thinning Carreau and Newtonian models yield the similar values for the axial velocity in the near viscinity of the wall, and as the shear rate decreases through the center of the vessel, the Newtonian model overestimates the velocity values at both

of the time instances. The relation between the Newtonian and the Carreau model is similar with the results given in the Section 5.1.1. At the peak systole ($t = 0.32\ s$), the modified Oldroyd-B model shows the velocity gradients near the wall are smaller with respect to both the Newtonian and Carreau model results, and as both the first normal stress difference, $\tau_{p,zz} - \tau_{p,rr}$, and the shear rate decrease through the center of the vessel the viscoelastic model yields much lower velocities compared to the other rheological models. The difference between the results can be related to the elastic response of the fluid, i.e. normal stress differences , since the Carreau is an inelastic model which mimics the shear thinning properties of the blood. At the end of the systole ($t = 0.53\ s$), the modified Oldroyd-B model yields higher velocity values than the Newtonian model as shown in Figure 5.8b. The reverse behavior between the peak and end systole time instances of the velocity field might be related to the increase in the first and the second, $\tau_{p,rr} - \tau_{p,\theta\theta}$, normal stress differences with decreasing shear rate through the center of the vessel.

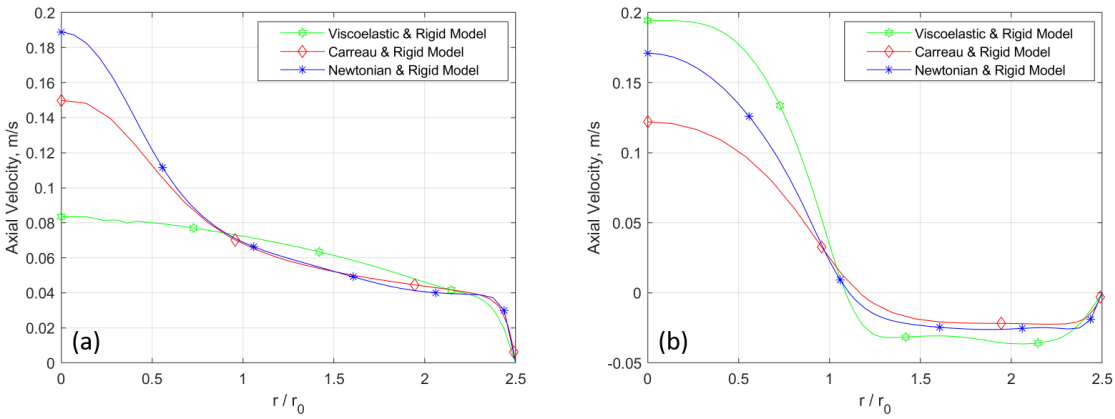


Figure 5.8. The axial velocity at the center of the rigid walled AAA for the different rheological models (a) at the peak systole, (b) at the end of the systole.

The first and the second normal stress differences at the peak and end systole are shown in the Figures 5.9 and 5.10 for the rigid and linearly elastic walled models, respectively. The differences concentrate between the ends of the aneurysm and the center of the vessel, therefore the flow field, as well as the vortical structure, inside the aneurysm are expected to be different than the Newtonian and Carreau models. Figures

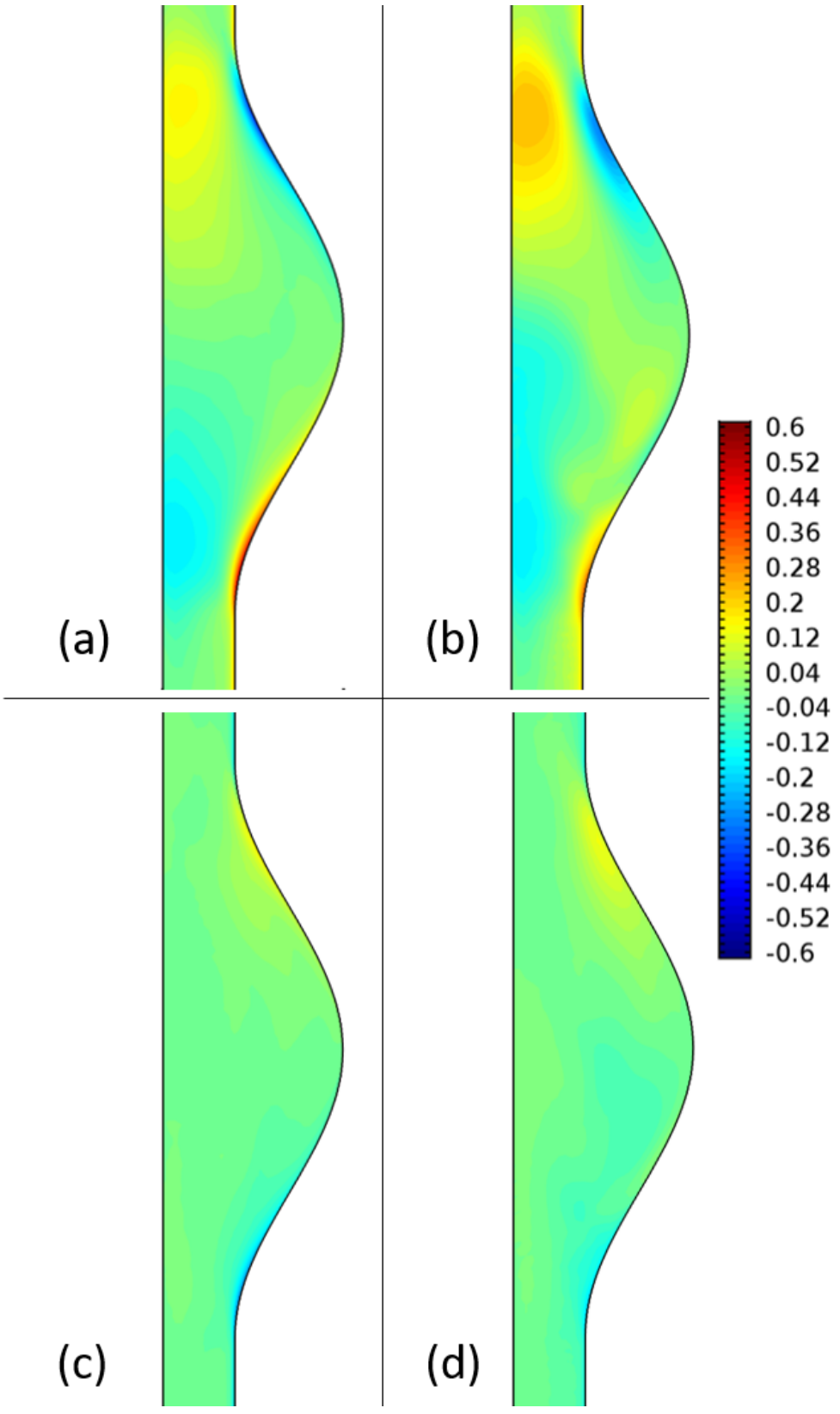


Figure 5.9. The normal stress differences for the rigid walled model: (a) $1^{st}$ at $t = 0.32\ s$, (b) $1^{st}$ at $t = 0.53\ s$, (c) $2^{nd}$ at $t = 0.32\ s$, (d) $2^{nd}$ at $t = 0.53\ s$.

5.9a and 5.9b show the first normal stress difference for the rigid walled aneurysm at the peak and end of the systole, respectively. At the end of the systole, the stress difference at the ends of the aneurysm decrease and the difference near the center increases compared to the peak systole instance. The second normal stress differences are given in the Figures 5.9c and 5.9d for the rigid walled model at the peak and end systole instances, respectively. The second normal stress difference concentrates near the ends of the aneurysm wall, unlike the first normal stress. In the linearly elastic walled model, shown in the Figure 5.10, the trend for the first and second normal stress differences is similar to the rigid walled model, whereas the values are higher than the rigid walled model. Both the first and second stress differences concentrate near the ends of the aneurysm at the peak systole, and their concentration shifts through the center of the vessel at the end of the systole, which may lead to significant differences in the vortical field between the rigid and linearly elastic walled models.

The axial velocities for the linearly elastic walled aneurysm model corresponding to the three rheological models are given in the Figure 5.11. As the vessel walls are modeled as elastic, they expand under the fluid pressure, therefore the velocity values are slower with respect to the rigid walled case [42]. All of the rheological models follow the same trends of the rigid walled model with slower velocities at the peak systole. However, the effect of pressure loss on the fluid velocity due to the expansion of the vessel is more dominant at the end of the systole, when the pressure is minimum throughout the cycle. The velocity field for the generalized Oldroyd-B model is affected more than the Newtonian and Carreau models, and the difference in the axial velocity between the viscoelastic and other rheological models increase towards the center of the vessel, which is opposite of the rigid walled model.

The total wall shear stress values acting on the vessel wall at the peak systole for rigid and elastic walled models are also investigated, and the trends of the Carreau and Newtonian models are found to be similar to the Figure 5.2, where their maximum differences occur at the distal end as 18.1% for the rigid walled model, and 11.1% for the linearly elastic model. Therefore, the results for Carreau model are not given on the figure. The total wall shear stress values for the viscoelastic and Newtonian models

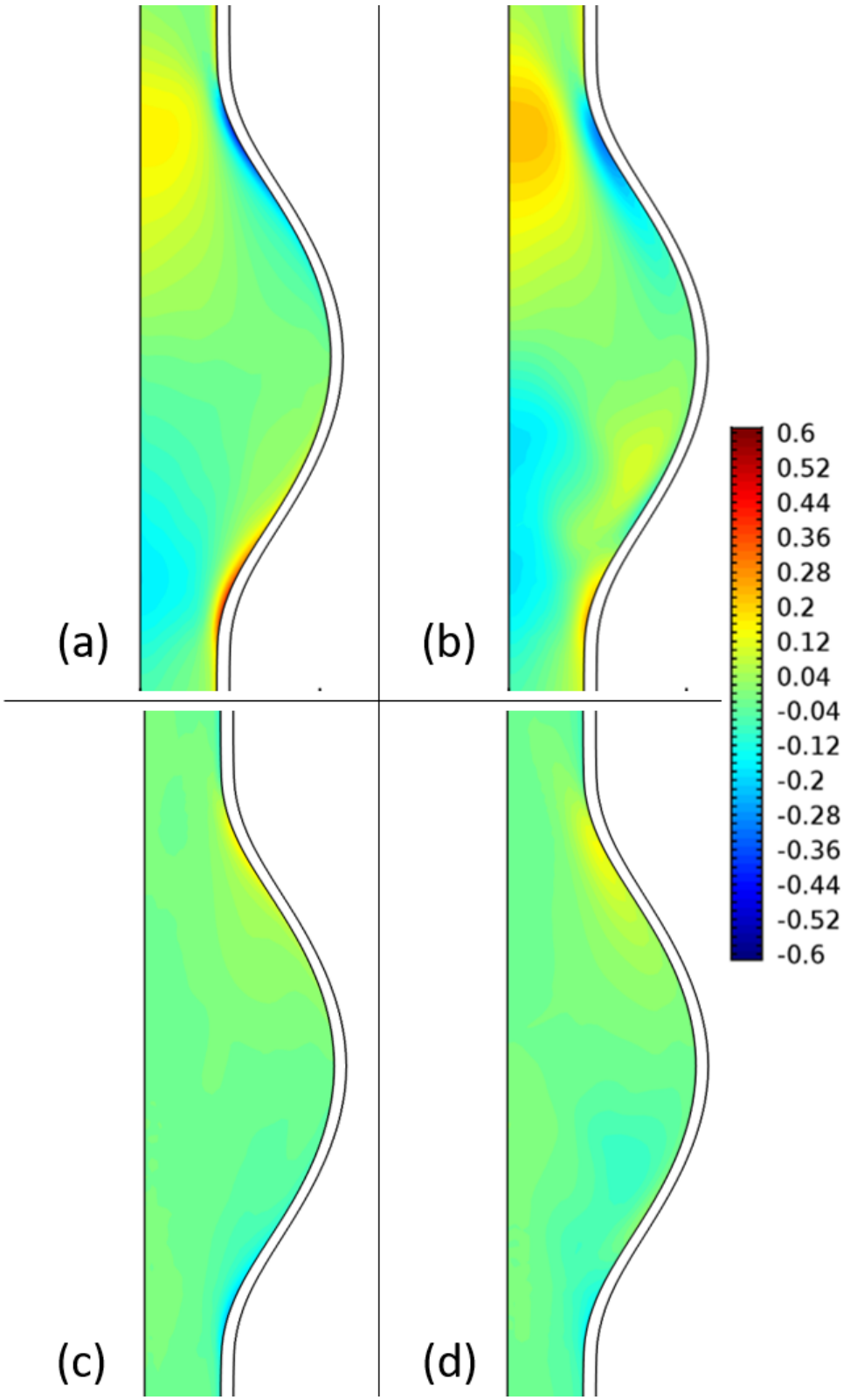


Figure 5.10. The normal stress differences for the linearly elastic model: (a) $1^{st}$ at $t = 0.32\ s$, (b) $1^{st}$ at $t = 0.53\ s$, (c) $2^{nd}$ at $t = 0.32\ s$, (d) $2^{nd}$ at $t = 0.53\ s$.

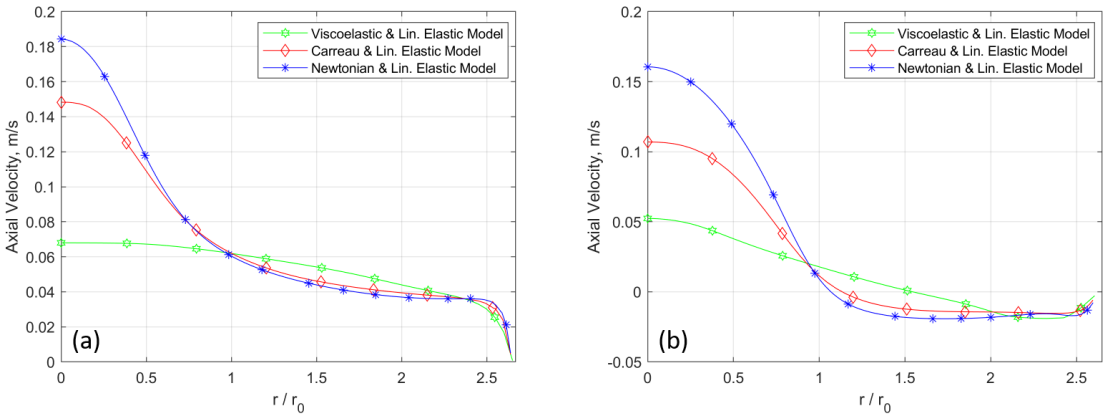


Figure 5.11. The axial velocity at the center of the linearly elastic walled AAA for the different rheological models (a) at the peak systole, (b) at the end of the systole.

are given in Figure 5.12 where the straight lines represent the rigid walled model, and the dashed lines represent the linearly elastic model. For all of the models, the wall shear stress values follow the similar trends as the maximum shear stress values are observed at the proximal and distal ends and the stress decreases through the center of the aneurysmal arc. However, at both proximal and distal ends of the aneurysm the deviation of the wall shear stress increases between the rheological models. The ends of the aneurysm are the locations where the highest first and second normal stress differences occur. For the rigid walled model, the wall shear stress difference between the Newtonian and modified Oldroyd-B rheological models is 14.6% at the distal ends. For the elastic walled model, the wall shear stress decreases towards the ends of the aneurysmal arc, as a structural response of the elastic walls. The wall shear stress values are similar at the center of the aneurysmal arc, however the viscoelastic model shows higher stress values through the distal end, as the first normal stress difference increases significantly. The difference in the WSS between the rheological models is 13.7% at the proximal end.

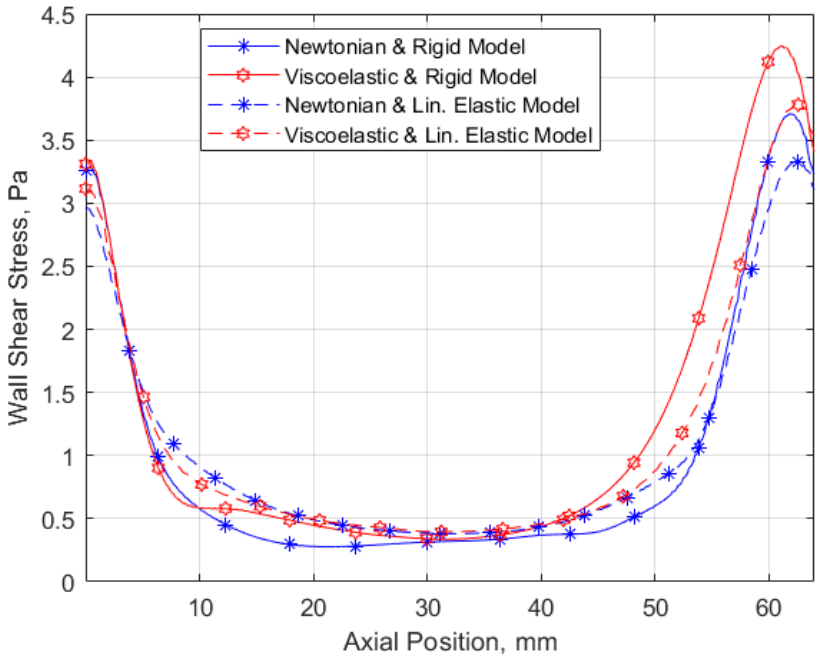


Figure 5.12. WSS Comparison for the different rheological and wall models at the peak systole.

The wall shear stress values lower than ∼2 Pa are considered as low shear stress regions and the endothelial cells may not align properly in these regions and the structure of the arterial vessel can not be maintained [11]. Similar to Figure 5.2, the wall shear stress (WSS) values are lower than 2 Pa in the middle section of the aneurysmal wall for the studied models, which is an indication for the degeneration of the arterial tissue and risk of arteriosclerosis.

Streamlines in the aneurysmal cavity are shown in Figures 5.13 and 5.14 at five different time instances in the cardiac cycle, presented in Figure 2.3, including the first deceleration ($t = 0.21\ s$), peak systole ($t = 0.32\ s$) and end of systole ($t = 0.53\ s$), for the rigid and linearly elastic models, respectively. The streamlines of the Newtonian and shear thinning Carreau model follow the same trends and the vortical structure in the Section 5.1.1, where the streamlines corresponding to these rheological models for different wall models are explained in detail. Therefore, the patterns for the Newtonian model with rigid walls are consistent with the experiments of Egelhoff *et al.* [51] which

shows that a primary vortex is formed at the proximal end of the AAA as the flow decelerates after the peak systole, and the vortex shifts to the distal end towards the end of the cardiac cycle.

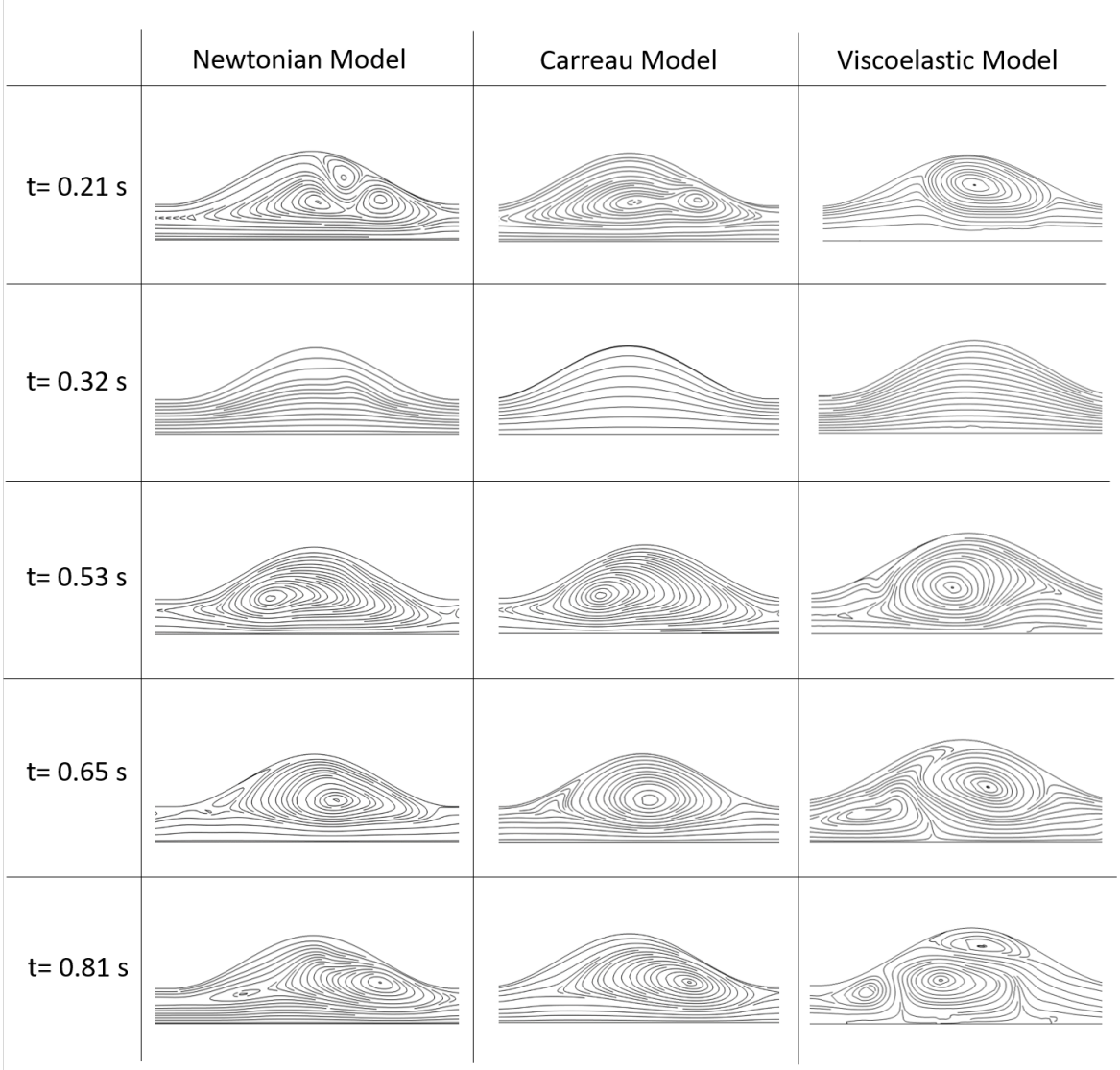


Figure 5.13. Streamlines for rigid walled model with different rheological models.

Although the shear thinning Carreau model does not show huge differences in the vortical field, the viscoelastic Oldroyd-B gives rise to significant changes in the vortical structure due to elastic effects. For the rigid walled simulations, given in Figure 5.13, at the first deceleration ($t = 0.21\ s$) the viscoelastic model shows a single vortex which is rotating in the clockwise direction, located near the vessel wall at the center of the

aneurysmal arc. The Newtonian model shows a primary vortex rotating in the clockwise direction located near the distal end with two additional vortices, a counter rotating vortex with respect to the primary vortex near the aneurysmal arc and a co-rotating vortex near the center of the aneurysmal cavity. At the peak systole ($t = 0.32\ s$), the flow field is similar with the other models and it displays fully attached profile. At the end of the systole $t = 0.53\ s$, the primary vortex is located closer to the center of the aneurysmal cavity compared to the Newtonian model, whereas both rheological models have similar vortex strength and rotation direction. At $t = 0.65\ s$, the primary vortex, which rotates in the counter clockwise direction, is located at the proximal end near the center of the vessel and a counter rotating secondary vortex appears near the aneurysmal arc in the viscoelastic case. However, the vortical structure in the Newtonian model displays primary vortex located at the distal end, which rotates in the clockwise direction. The viscoelastic fluid simulation shows differences in both the location and the rotation direction of the primary vortex. At $t = 0.81\ s$, the primary vortex is rotating in the clockwise direction near the proximal end. This location is similar to the previous time instance, however it is closer to the vessel wall and the rotation direction is reversed. Also, there are two additional vortices, one of them is counter rotating and appears at the center of the aneurysm and the other one is co-rotating with the primary vortex and located near the aneurysmal arc. The additional vortex at the previous time instance is diminished in size and shifted through the vessel wall. The location of the primary vortex in the Newtonian model is shifted to the other end of the aneurysmal cavity compared to the viscoelastic model. Therefore, the fluid elasticity leads to changes in the position, number and the rotation direction of the vortices in the rigid walled simulations.

For the elastic walled simulations, the differences in the vortical structure between the rheological models are similar with the rigid walled simulations, in terms of the rotation direction, number and strength of vortices. The main difference between the vortical structure of the rigid and linearly elastic walled models, is the shift of the center of the vortices towards the proximal end of the aneurysm.

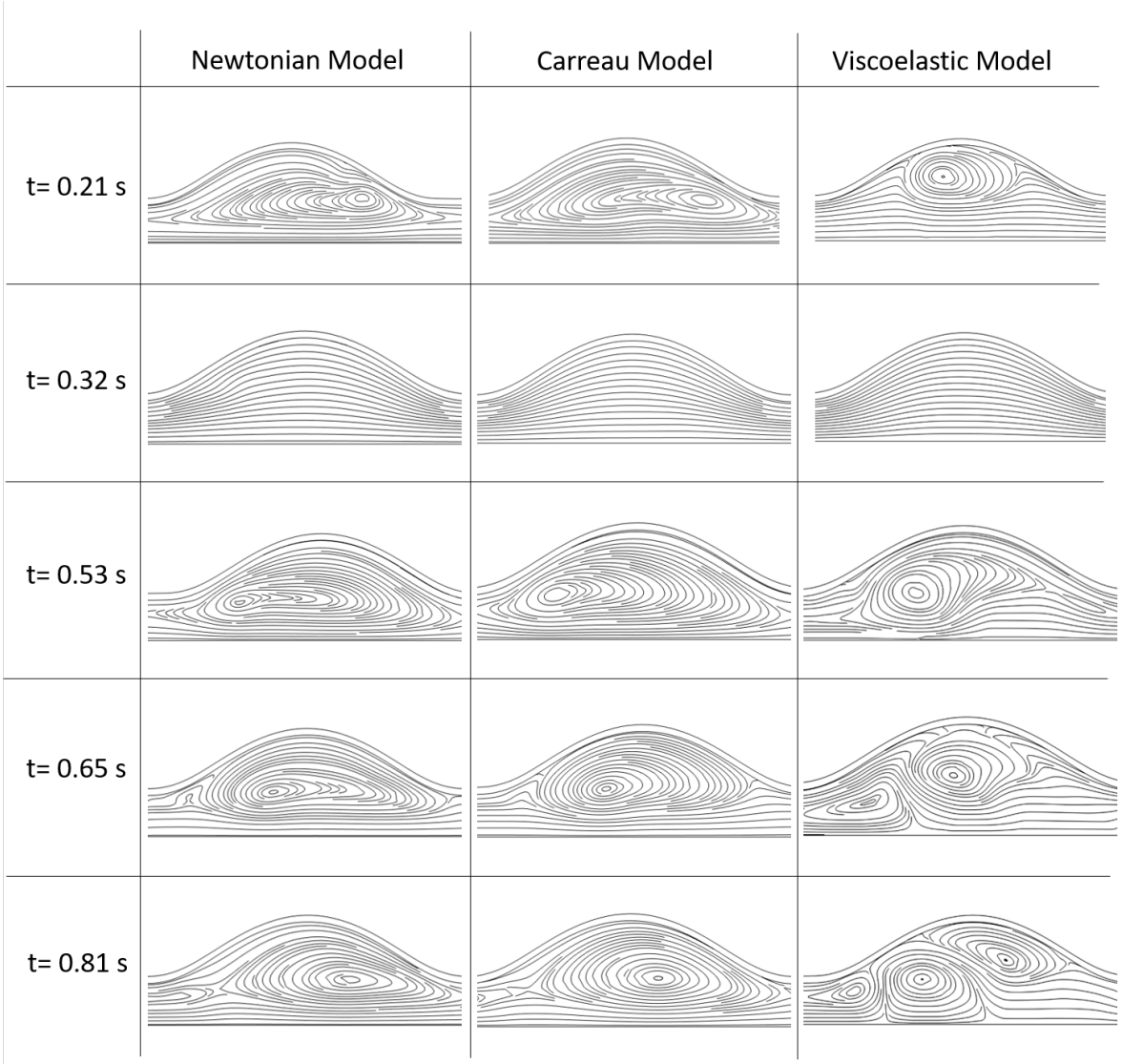


Figure 5.14. Streamlines for linearly elastic walled model with the different rheological models.

### 5.2.2. Risk indicators

The pressure gradient at the inlet is oscillating due to the nature of the pulsatile flow, and the oscillations lead to oscillating wall shear stress and the highly oscillating wall shear stress is related with the degeneration of the vessel tissue. The commonly used risk indicators, oscillatory shear index and time-averaged wall shear stress have been introduced and explained in detail in the Section 5.1.3.

OSI distributions on the aneurysmal arc corresponding to Newtonian and viscoelastic models at resting conditions for both rigid and linearly elastic walls are shown in the Figures 5.16a and 5.16b, respectively. The OSI distribution for the Carreau and Newtonian models with the linearly elastic walled vessel is given in the Figure 5.15, to understand the difference occurring due to the shear thinning property of the blood, so that the effect of elasticity could be observed.

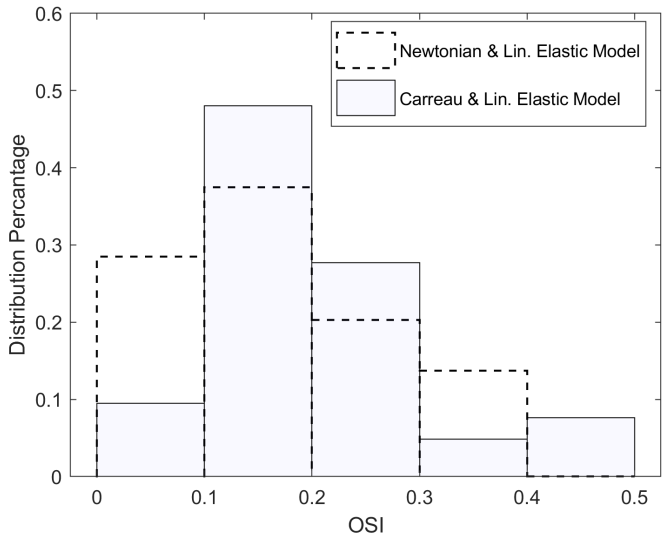


Figure 5.15. Distribution percentage of oscillatory shear index for Newtonian and Carreau fluid with linearly elastic walled model.

The healthy elastic behavior of the vessels are maintained under low oscillatory shear stresses (OSI<0.20) as reported by Glor *et al.* [93]. The differences in OSI between the shear thinning Carreau and Newtonian models are similar with the values presented in the Section 5.1.3, where the shear thinning model shows the average OSI and high oscillating regions (OSI>0.20) are higher by 0.04 and 6.1%. The slight differences between the results of Sections 5.1.3 and 5.2.2 are expected since the outlet conditions are different.

As the shear thinning and viscoelastic properties of the blood are taken into account, the average OSI values change slightly for the linearly elastic walled model

(<0.01), however, the regions experiencing high OSI (>0.20) increase by 4.3%. The rigid walled model shows higher OSI values compared to the elastic walled case for both Newtonian and viscoelastic models. The average OSI value increases 0.07 and the high OSI value increases 18.0% for the viscoelastic model when the vessel walls are assumed to be rigid. This is consistent with the physiological situation, since the rigid walled model is considered as the pathological case of arteriosclerosis, where the vessel tissue is degenerated and the healthy elastic behavior of the walls are lost. Also, in the case of arteriosclerosis arterial leaking occurs as the tissues start to tear with the high oscillating shear stress which increases the rupture risk of the aneurysm [12, 73]. The OSI indicates that both the viscoelastic and Carreau models show higher risk of rupture than the Newtonian model, and Carreau model predicts higher risk values than the viscoelastic model.

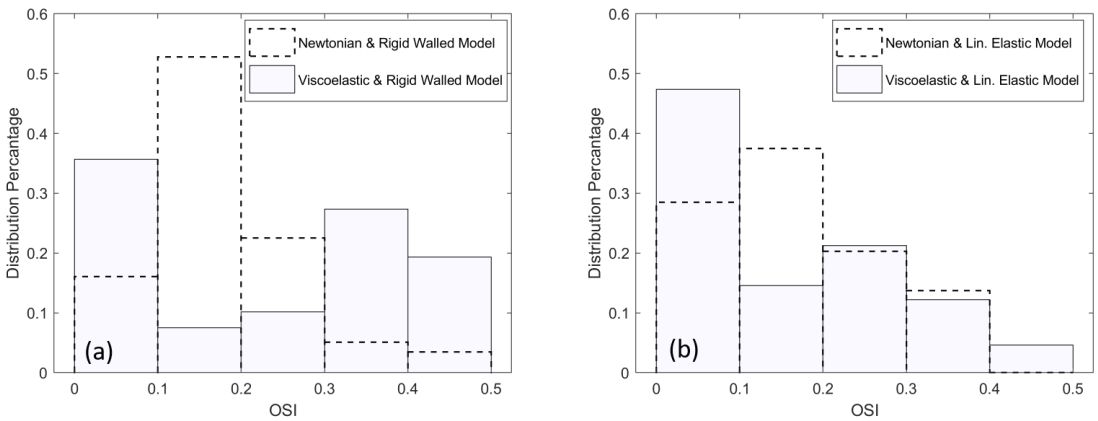


Figure 5.16. Distribution percentage of oscillatory shear index for Newtonian and viscoelastic fluid with (a) rigid walled model, (b) linearly elastic walled model.

In addition to OSI distribution, the comparison of the time-averaged wall shear stress (TAWSS) percentage distribution on the aneurysm is displayed in Figure 5.17a between the Newtonian and Carreau models, and Figure 5.17b shows the comparison of TAWSS between the Newtonian and viscoelastic fluid models. According to the investigations of Kawaguchi *et al.* [12], the ruptured aneurysms experience low TAWSS with a mean value of 0.49 Pa. The presented TAWSS results show that all of the

aneurysm experience low TAWSS ($< 0.49Pa$) for both the Newtonian and Carreau models, and the 88.5% of the wall is under the low TAWSS for the viscoelastic model. Therefore, in the simulated situation based on TAWSS the aneurysm is under high risk of rupture for all of the rheological models.

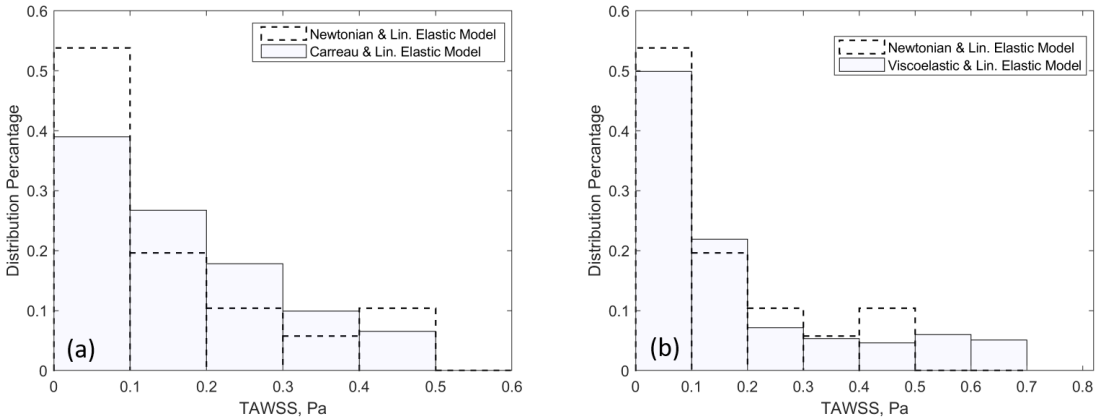


Figure 5.17. Distribution percentage of TAWSS on the aneurysmal wall for (a) Newtonian and Carreau models, (b) Newtonian and viscoelastic fluid models.

As the real physics of the hemodynamics cannot be reproduced in the laboratories, there are no experiments for the blood flow under these conditions. However, it is well known that the blood has both the viscoelastic and shear thinning properties [20–23], therefore it is safe to assume the modified Oldroyd-B model predicts the hemodynamics more accurately, and the Carreau model overpredicts the risk indices, whereas the Newtonian model underestimates.

### 5.2.3. Effects of Smaller Artery and Higher Elasticity

The elastic effects of a fluid can be monitored by introducing the elasticity number which is the ratio of Weisenberg to Reynolds numbers, as given in detail in the Section 2.5. The elasticity number depends on the fluid velocity, fluid viscosity, relaxation time and flow geometry. In this Section, the effect of fluid elasticity is investigated by keeping the fluid properties constant and reducing the vessel diameter to its half.

Therefore, the elasticity number for the small artery model is the four times of the original vessel geometry. The new artery geometry is used to model a small artery, then the original geometry corresponds to a large artery.

The simulations using the small artery geometry are performed for three rheological, namely Newtonian, shear thinning Carreau and modified Oldroyd-B models, and linearly elastic wall models. The boundary conditions applied in these simulations are introduced in the Section 2.1 and the corresponding Reynolds and Weissenberg numbers are $Re_{m,N} = 150$ and $Wi_m = 0.04$, respectively. The results of the small and the large artery geometries are compared in terms of the differences in the axial velocity at the center of the AAA, the wall shear stress, vortical structure and risk indicators for all rheological models. Also, the first and second normal stress differences are compared with the original aneurysm geometry.

The first $\tau_{p,zz} - \tau_{p,rr}$, and the second, $\tau_{p,rr} - \tau_{p,\theta\theta}$, normal stress differences are used to investigate the changes in the stress field with the increase in the elasticity number. Figure 5.18 shows these stress differences at the peak and end systole for small arterial aneurysm geometry. The first normal stress differences at the peak systole and end of the systole are given in the Figures 5.18a and 5.18b, where the differences concentrate between the center of the vessel and aneurysm wall near the distal and the proximal ends, similar to the original aneurysm geometry, whereas these differences are significantly higher than the results given in Figures 5.9 and 5.10. At the end of the systole the first normal stress difference decreases while its distribution is similar to the peak systole. Figures 5.18c and 5.18d represent the second normal stress difference at the peak and end of the systole, respectively. The higher differences concentrate near the ends of the aneurysm, unlike the first normal stress difference. Similar to the large arterial aneurysm geometry, both of the stress differences concentrate at the ends of the aneurysm at the peak systole, and the concentration shifts through the center of the vessel at the end of the systole, which is more significant in the second normal stress difference for the small artery.

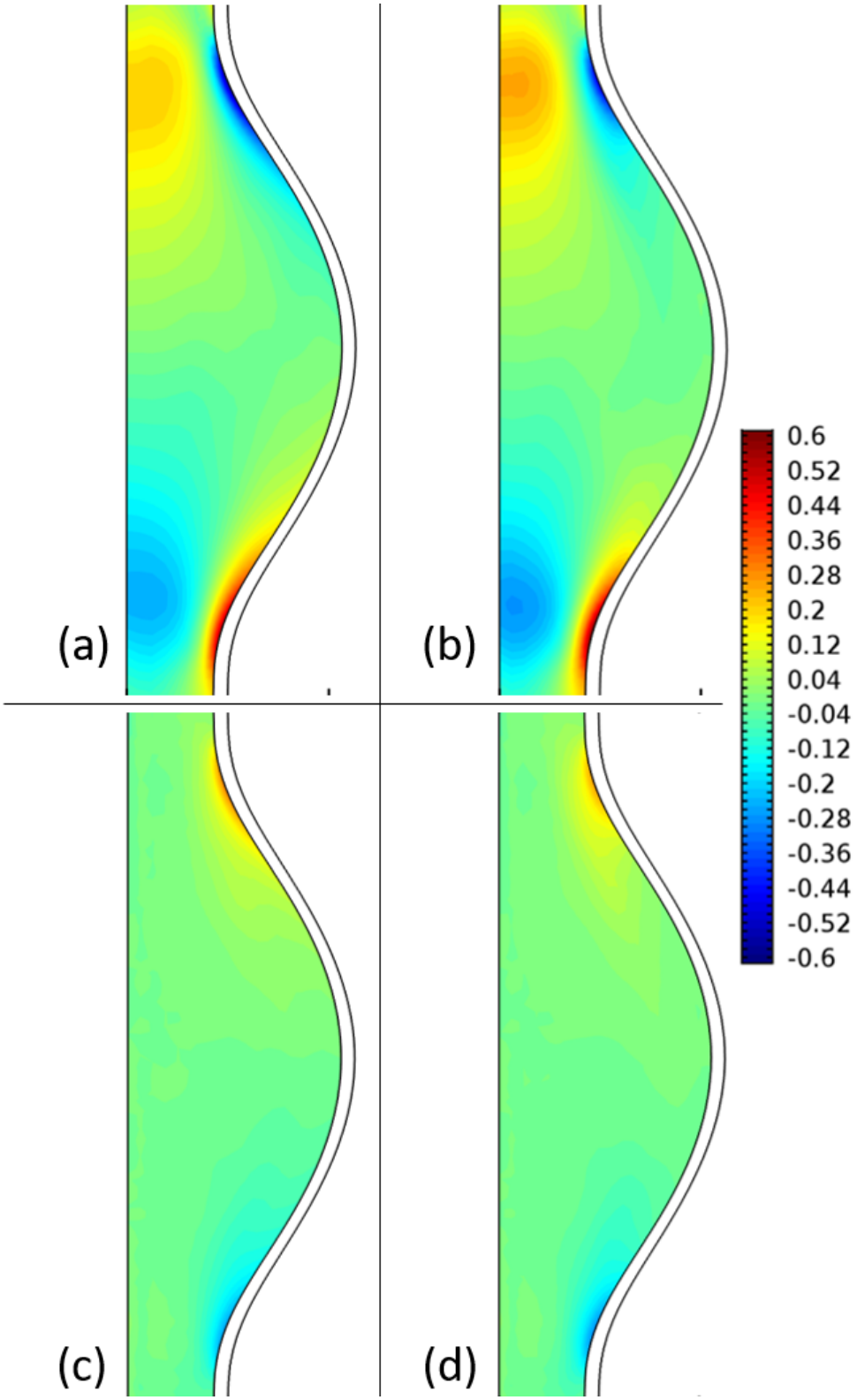


Figure 5.18. The normal stress differences in the small artery model: (a) $1^{st}$ at $t = 0.32\ s$, (b) $1^{st}$ at $t = 0.53\ s$, (c) $2^{nd}$ at $t = 0.32\ s$, (d) $2^{nd}$ at $t = 0.53\ s$.

The axial velocities at the center of the AAA corresponding to the two aneurysm geometries are given in the Figures 5.19a and 5.19b for the Newtonian and Carreau models at two time instances, respectively. The comparison for the Oldroyd-B model is given Figures 5.21a and 5.21b at different time instances.

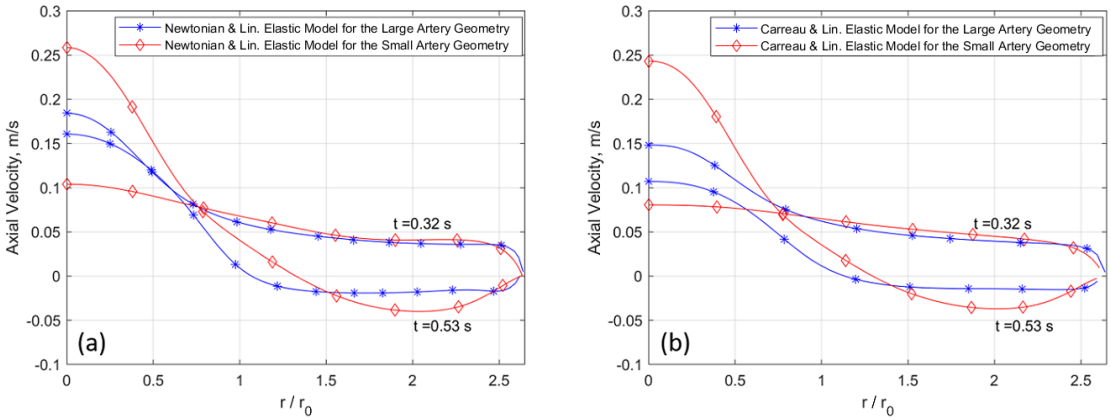


Figure 5.19. Axial velocity at the center of AAA for the large and small artery geometries with (a) Newtonian model, (b) Carreau model.

The Newtonian and Carreau models show that the axial velocities display similar behavior near the wall and the center of the cavity for both arteries at the peak systole ($t = 0.32\ s$). However, the velocity profiles separate near the center of the vessel, and the velocity values are significantly lower for the small artery model. At the end of the systole ($t = 0.53\ s$), the velocity trend in the small vessel is different from the large arterial model. The velocity values at the center are higher when compared with the large artery, and the velocity gradient is smaller the near vicinity of the vessel.

The effect of shear thinning fluid rheology on the axial velocity in the small arterial geometry, is shown in the Figure 5.20, where velocity profiles corresponding to the Newtonian and Carreau models at two time instances are given. In the Figure 5.20, it can be observed that the shear thinning properties are less effective on the axial velocity in the small artery model compared to the original aneurym geometry, which can be explained with the reduction in the diameter reducing the Reynolds number,

which in turn increases the shear rate. At high shear rates, the Carreau fluid model behaves like Newtonian model, therefore the flow field properties are expected to be similar.

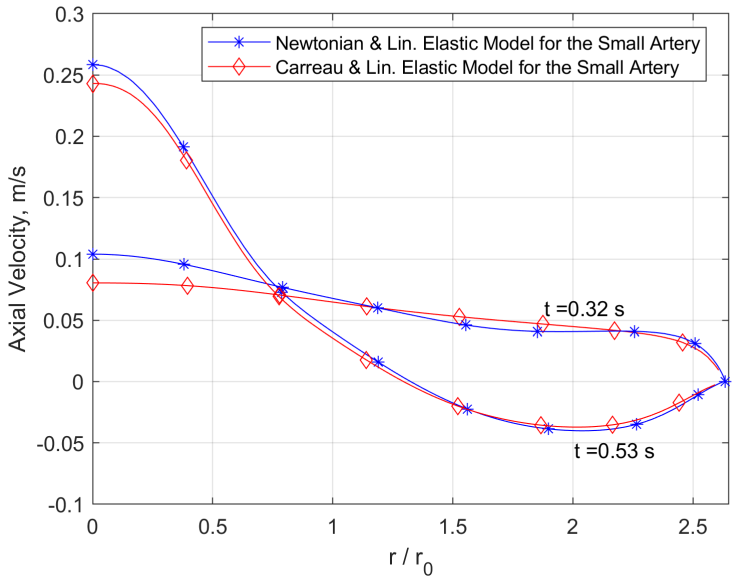


Figure 5.20. Axial velocity at the center of the small AAA geometry for the Newtonian and Carreau models.

The reduction of the flow geometry is expected to affect the viscoelastic fluid model more than the Newtonian and Carreau models. The axial velocity differences between the geometries for the modified Oldroyd-B model are given in the Figures 5.21a and 5.21b at the peak and end systole instances, respectively. It can be seen from the Figure 5.21a the velocity profile for the small artery is similar with the large arterial geometry at the peak systole, and the velocity field as well as the difference between the two models are similar with the profiles for the purely shear thinning and Newtonian models, presented in the Figure 5.20. Also, the small differences between the geometric models may be attributed to the increase in the shear rate, and the velocities are slower compared to the Newtonian and Carreau models as a result of elastic properties of the fluid, as explained in the Section 5.2.1. The velocity profile at the end of the systole ($t = 0.53\ s$), given in Figure 5.21, shows that the increase of the

elasticity changes the velocity field and the vortical structure, which will be presented in Figure 5.22. As displayed in the velocity profile at Figure 5.21b, near the vessel wall the velocity field has a smaller gradient compared to the large artery model, and at the center of the aneurysmal cavity the velocity values decrease to a negative value due to an additional vortex appearance in the case of small artery.

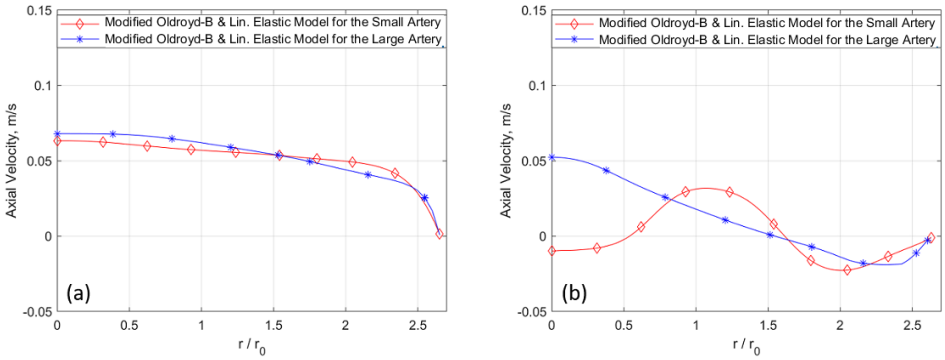


Figure 5.21. Axial velocity at the center of both AAA geometries for the modified Oldroyd-B model at (a) peak sytole ($t = 0.32\ s$), (b) end of the systole ($t = 0.53\ s$).

The vortical structure throughout the cardiac cycle is given for the small vessel model with the three rheological models in Figure 5.22. The flow field is shown at five different time including the first deceleration ($t = 0.21\ s$), peak systole ($t = 0.32\ s$) and end of systole ($t = 0.53\ s$), same as the streamline comparisons given in the Sections 5.1.1 and 5.2.1. When the vortical structure given in the Figure 5.22 is compared with the Figure 5.14 in order to understand the changes in the flow field with the change of diameter, i.e. Reynolds number, it is observed that the location of the primary vortices change and the additional vorticies appear after the end of the systole ($t = 0.53\ s$).

The Newtonian and Carreau model show nearly the same vortical field for the small artery model, except the instance of first deceleration ($t = 0.21\ s$). At that time instance, the Newtonian model shows three vortices, the primary vortex is rotating in the clockwise direction and it is located near the center of the cavity. Also, there are two additional vortices, the one near the distal end is co-rotating with the primary

vortex, whereas the other additional vortex is located near the aneurysmal arc and it rotates in the counterclockwise direction. The Carreau model shows a single vortex rotating in the clockwise direction at the instance of first deceleration. In the following time instances, the vortical structure is same for the Newtonian and Carreau models in terms of size, strength and vortex number, however the center of the vortices shifts through the center of the cavity for the Carreau model, which is consistent with the results presented in the previous Sections 5.1.1 and 5.2.1. Also, as observed from the axial velocity profiles of the Newtonian and Carreau models, shown in Figure 5.20, the difference in the flow field between these models are smaller compared to the large artery model, since the shear rate increased as the diameter decreased.

Figure 5.22 shows the effects of viscoelasticity on the vortical structure. At the first time instance, a single vortex is located at the center of the aneurysmal cavity, even though the location of the vortex is similar to the Carreau model, the vortex in the viscoelastic fluid model rotates in the counterclockwise direction, which is opposite to the results for Carreau model. At the peak systole ($t = 0.32\ s$) the flow field displays fully attached flow for all rheological models. As in the previous cases (Figures 5.3, 5.4, 5.13 and 5.14) and the experiments of Egelhoff *et al.* [51] at the peak systole. At the end of the systole ($t = 0.53\ s$), two counter rotating vortices appear in the aneurysm, the primary vortex dominates the center of the cavity and its center is located near the distal end, and the additional vortex rotates in the clockwise direction and it is located near the proximal end of the aneurysm. At the late diastole ($t = 0.65\ s$), the primary vortex preserves its direction and its size increases to fill the whole cavity, whereas the counter rotating additional vortex, observed at the end of systole ($t = 0.53\ s$), is translated through the vessel wall near the distal end. As the flow decelerates at the $t = 0.81\ s$, the vortices are translated to the center of the aneurysm and an additional vortex, which is counter rotating to the primary, appear. The secondary vortex is located near the vessel wall between the center of the aneurysm and the proximal end, and the additional vortex is located near the distal end of the aneurysm.

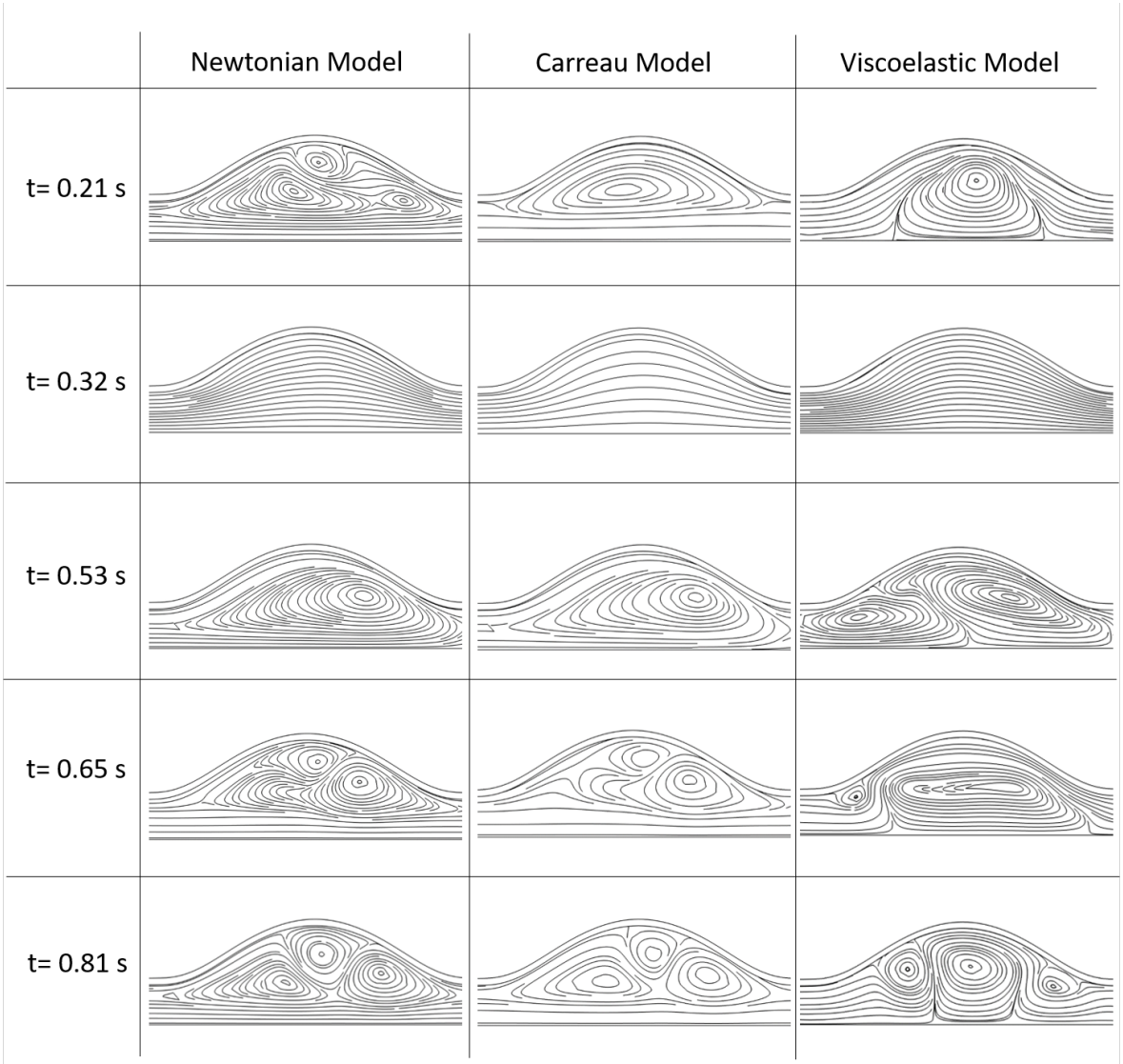


Figure 5.22. Streamlines of the small artery with aneurysm for the three rheology.

When the streamlines of the viscoelastic model are compared for the different aneurysm geometries, in Figures 5.14 and 5.22, the effect of the elasticity on the vortical structure can be observed, and for the simplicity the streamlines of these two models are presented in Figure 5.23, where LAM and SAM stand for the large artery model, and the small artery model, respectively. At the first deceleration ($t = 0.21\ s$), the large arterial model shows a single vortex rotating in the clockwise direction at the center of the aneurysm wall, whereas the small vessel model shows both the location and the direction of the vortex changes as with elasticity increasing. At the end of the systole ($t = 0.53\ s$), a single vortex, rotating in the clockwise direction, dominates the

aneurysmal cavity and its center is located between the proximal end and the center of the aneurysm according to large artery model, whereas for small artery model shows the primary vortex is located at the distal end and rotates in the reverse direction. Also, there is a counter rotating secondary vortex near the proximal end. Similarly, in the following time instances both the location and rotation directions are affected as the elasticity is increased.

Wall shear stress at the peak systole for Newtonian and viscoelastic rheological with large (LAM) and small (SAM) artery models are given in the Figure 5.24, where the straight and dashed lines represent SAM and LAM models, respectively. The wall shear stress values of the Carreau model is found to be similar in trend with the Newtonian model, and the stress values at the ends of the aneurysms are less than the Newtonian model by 8.0% and 13.1% for the proximal and distal ends, respectively. Therefore, it can be observed that the shear thinning effects lead to smaller wall shear stress values in the SAM geomertry. In order to observe the combined effect of viscoelastic and shear thinning properties of blood, the comparison of wall shear stress for the Newtonian and modified Oldroyd-B models are given. In Figure 5.24, Newtonian model shows higher stress values than the viscoelastic model and the deviations at the ends of the aneurysm are less than 1.0%. However, the region experiencing negative stress value, i.e. experiencing stress in the other direction, is bigger for the Newtonian model than the viscoelastic fluid model. Therefore, it is expected to observe differences in the oscillatory shear index (OSI).

The risk indicators have been discussed in detail in the previous Sections 5.1.3 and 5.2.2, as the oscillating flow conditions lead the wall shear stress to change direction. The change of the wall shear stress vector is an important indicator of rupture risk of the vessel. Also, the time averaged wall shear stress is used to understand the regions experiencing low shear stress, which degenerates the endothelial cells and may cause to pathological conditions, such as arteriosclerosis. The differences in the oscillatory shear stress and the time averaged wall shear stress are investigated for the three rheological models for the small arterial aneurysm geometry and they are compared with the results of large artery.

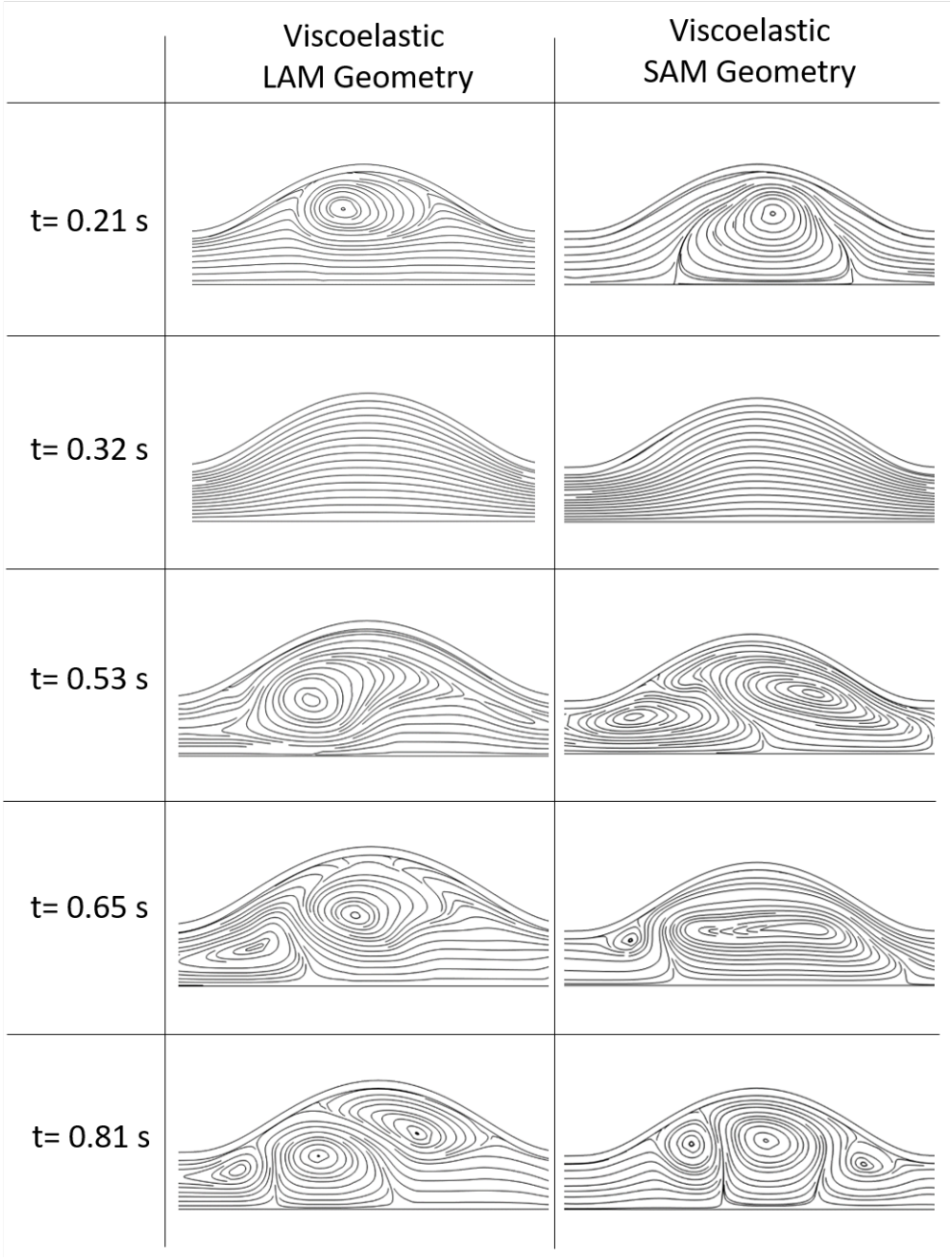


Figure 5.23. Streamlines of the large and small arterial aneurym geometries for the viscoelastic fluid model.

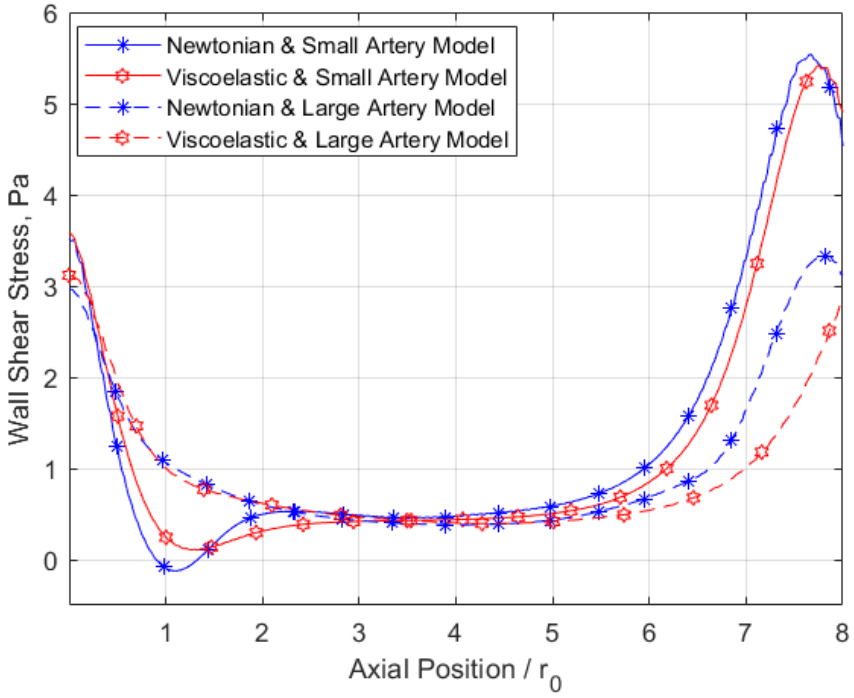


Figure 5.24. Wall shear stress at the peak systole for Newtonian and modified Oldroyd-B model with large and small artery geometries.

Figure 5.25a shows the difference in the oscillatory shear index (OSI) in the small aneurysm for the Carreau and Newtonian models, and the Figure 5.25b shows the differences between the Newtonian and viscoelastic fluid models. The average OSI value increases by 0.05, when only the shear thinning property of the blood is taken into account, whereas, the average OSI changes slightly ($< 0.01$) between the viscoelastic and Newtonian models. However, the regions experiencing high OSI ($>$ 0.20) values increases by 21.9% and 20.3% for the viscoelastic and Carreau rheological models compared to the Newtonian model, respectively. Similar to the results of other subsections, Newtonian model underestimates the risk of rupture by underestimating the oscillation of the wall shear stress, and in terms of average OSI the Carreau model predicts higher values than both the viscoelastic and Newtonian model.

The distribution of the OSI is compared for the LAM and SAM geometries to observe the effect of the increase in the shear rate and the elasticity of the fluid. Figures

5.26a, 5.26b and 5.26c represent OSI distributions of the Newtonian, Carreau and modified Oldroyd-B models in the large and small vessels, respectively. The average OSI values increase between the geometric models by 0.06 for all rheological models. Although, the fluid rheology seems not to affect the average of the OSI, the regions under the influence of high oscillations increase by 9.9%, 24.0% and 27.7% for the Newtonian, Carreau and viscoelastic fluid models, respectively. Therefore, the rupture risk increases significantly with the increase of shear rate, as well as the elastic effects.

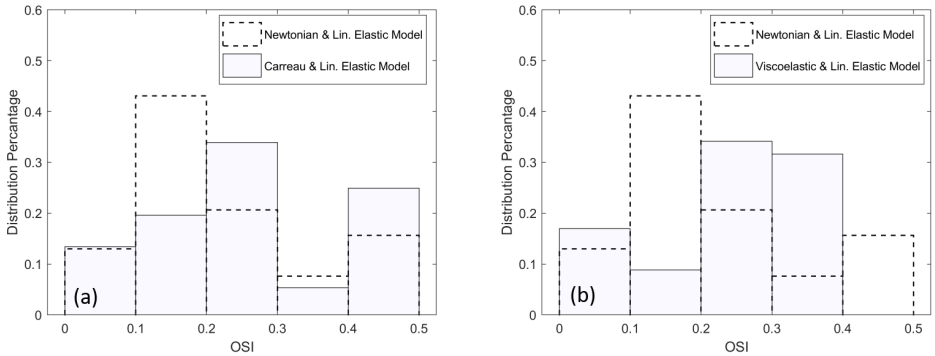


Figure 5.25. Distribution percentage of oscillatory shear index in small artery for (a) Newtonian and Carreau models, (b) Newtonian and viscoelastic fluid models.

In addition to OSI distribution, time-averaged wall shear stress (TAWSS) percentage distributions on the small vessel model are shown in Figure 5.27. TAWSS for the Newtonian and Carreau models are compared in the Figure 5.27a and the viscoelastic and Newtonian models are given in the Figure 5.27b. As previously explained in the Sections 5.1.3 and 5.2.2, Kawaguchi *et al.* [12] reported that ruptured cerebral aneurysms have lower shear stress values than non-ruptured ones. According to their results, TAWSS is lower at the point of rupture with the mean value of 0.49 Pa. When only the shear thinning properties are taken into account, regions experiencing low TAWSS increase by 4.3% for the small artery model with respect to Newtonian model, whereas the low TAWSS distribution decreases for the viscoelastic fluid with respect to Newtonian model by 1.7%.

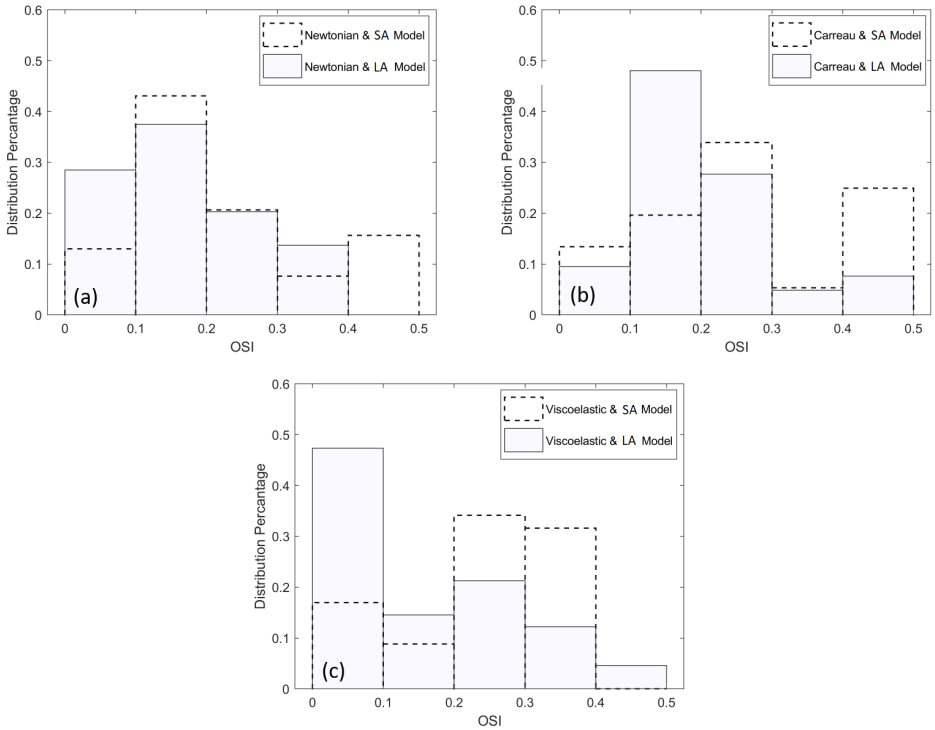


Figure 5.26. Distribution percentage of oscillatory shear index for the large and small artery geometries with different rheological models: (a) Newtonian, (b) Carreau, (c) modified Oldroyd-B models.

TAWSS increases with the small arterial model compared to the large artery, since the wall shear stress values increase with the increase of the shear rate, as shown in the Figure 5.24. The small artery model shows that the average TAWSS is higher by 0.07 Pa, 0.08 Pa, and 0.13 Pa compared to the large artery geometry for Newtonian, Carreau and viscoelastic fluid models, respectively. As the TAWSS values increase with the small vessel geometry, the regions experiencing low shear stress decrease by 19.3%, 15.0% and 9.5%, for the Newtonian, Carreau and viscoelastic rheologies, respectively.

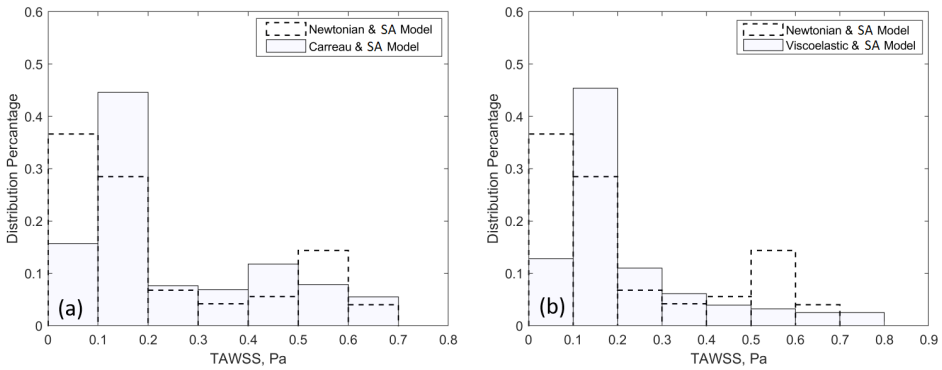


Figure 5.27. Distribution percentage of TAWSS on the small artery model for (a) Newtonian and Carreau models, (b) Newtonian and viscoelastic fluid models.

Basing on the risk indicators, the use of different fluid rheology may predict similar rupture risk, since the low TAWSS regions are found to be similar between the rheological models in small artery model. However, the shear thinning and viscoelastic models show higher oscillatory shear stress, as well as average OSI, compared to Newtonian model, leading to higher rupture risk. The highly oscillating shear stress is influencing bigger regions for the viscoelastic model. Also, both the shear thinning and viscoelastic properties of the blood are well established, so that the modified Oldroyd-B model is assumed to mimic the physiological conditions more accurately than Carreau and Newtonian models. Therefore, omitting the viscoelastic behavior of the blood may lead to predict lower risk of rupture, and underestimate the risk of arterial degeneration.

# 6. CONCLUSION

In this study, the effects of using different rheological and wall models on pulsatile blood flow through an abdominal aortic aneurysm are investigated. Throughout the study the aneurysm is assumed to be symmetric, developed and two dimensional. The aortic parts before and after the aneurysm are modelled as straight tubes. The mechanical properties of the aneurysmal wall are kept constant and a uniform wall thickness is assumed. These limitations might be overcome when the three dimensional patient specific geometries are applied and the geometric non-linearities are taken into account. The aim of this study is to show the differences in blood flow and wall displacement fields as well as the aneurysmal rupture risk indicators when different blood rheology and wall elasticity models are used in combination for the simulations.

In the first part of the thesis, the purely shear thinning effects on hemodynamics are investigated by using shear thinning Carreau and Newtonian models for the blood rheology. Healthy and degenerated vessel tissues are considered by using elastic and rigid wall models, respectively. Two rheological models namely, the Newtonian and the non-Newtonian Carreau and two elastic wall models, linearly elastic and hyperelastic Yeoh, are used. The velocity fields for all rheological and wall models show similar trends in the aneurysmal cavity, whereas Newtonian model overestimates the velocity values compared to the Carreau model especially near the center of the vessel at instances of the cardiac cycle. At the end of the systole, the deviations in the velocity field near the centerline between the Newtonian and Carreau models are higher than the peak systole, and these deviations increase for the elastic wall cases compared to the rigid walled. For the Newtonian model, the location of the primary vortex center in the aneurysm moves closer to the distal end, when compared to the Carreau model, after the peak systole of the cardiac cycle. The effects of wall model on the vortical structure are observed to be small, since both rheological models yield the similar vortex formation and translation trends. Elastic wall simulations show that the hemodynamic pressure exerted on the vessel walls causes an expansion which leads to lower flow velocities as well as lower wall shear stress values. Hyperelastic wall model

yields that von Mises stress exerted on the vessel wall is higher than the linearly elastic model. Also, near the center of the aneurysm, the linearly elastic model underestimates the resulting stress values when compared to hyperelastic model. However, the displacement of the vessel corresponding to the hyperelastic model is lower compared to the linearly elastic model, whereas both of the models show that the displacement values are within the expected range for AAAs. As the risk indices are investigated, Carreau model displays higher OSI with low TAWSS values compared to Newtonian case for both elastic wall models, which indicates a higher risk for arterial degeneration. Also, the hyperelastic model indicates significantly higher risk of degeneration with respect to linearly elastic model. Therefore, assuming blood as a Newtonian fluid leads to significant differences in the oscillatory hemodynamic behavior even in large arteries when compared to shear thinning Carreau model, for all wall models, including rigid, linearly elastic and hyperelastic cases. Also, the Newtonian blood rheology with linearly elastic wall assumption gives much lower aneurysmal rupture risk with respect to the non-Newtonian Carreau blood rheology and hyperelastic wall case.

In the second part, the combined effects of viscoelastic and shear thinning properties of blood on the hemodynamics under the pulsatile flow conditions are investigated by using Newtonian, shear thinning Carreau and modified Oldroyd-B models for the blood rheology, as well as linearly elastic and rigid vessel walls to represent the healthy and degenerated vessel tissues, respectively. The aneurysm geometry and the outlet condition applied in the first part are modified in order to reduce the constraints on the simulation. Although, the same rheological and structural models, as well as the inlet condition are same for these two parts, the results of the second part slightly differ due to the changes in the outlet condition and the geometry. The differences between the rheological and structural models are sought in terms of axial velocity, vortex field in the aneurysm, wall shear stress and the OSI and TAWSS risk indicators. Also, the first and second normal stress differences at different time instances for the viscoelastic fluid model are discussed in order to show the possible differences in the vortex structure due to fluid rheology. The aforementioned output parameters are used to observe the effects of shear rate and elasticity increase by reducing the diameter of the vessel geometry. The axial velocity profiles for the rigid walled simulations, are similar

for the Carreau and Newtonian models near the vessel walls, whereas the viscoelastic fluid model gives rise to a smaller velocity gradient compared to the other rheological models. Also, the modified Oldroyd-B model shows lower velocity values through the center of the vessel, as both the first normal stress difference and the shear rate decrease. At the end of the systole, the behavior of the axial velocity is reversed for the viscoelastic fluid model, and it predicts higher velocity values than the Newtonian and Carreau rheological models. The linearly elastic walled simulations show that the expansion of the vessel walls under fluid pressure reduces the velocity values, and the pressure loss of the fluid is more dominant for the viscoelastic fluid model at the end of the systole, when the pressure is minimum throughout the cycle. The wall shear stress values at the peak systole follow the similar trends for all rheological models and the maximum deviations in the wall shear stress are observed at the proximal and distal ends of the aneurysm between the fluid rheologies. These ends of the aneurysm are the locations where the highest first and second normal stress differences occur in the flow field. The vortical structure is observed for all rheological and wall models at different time instances, and the differences in the vortex field show that modeling the blood as an elastic fluid leads to changes in the position, number and the rotation direction of the vortices. The investigations of the risk indices show that the modified Oldroyd-B model show significantly higher oscillating shear stress compared to the Newtonian model, whereas the Carreau model yields higher average OSI than the other rheological models. Since the blood is a well known viscoelastic and shear thinning fluid, the Oldroyd-B model is assumed to predict the hemodynamics more accurately, and the Carreau model might be overpredicting the risk indices, whereas the Newtonian model underestimates.

The diameter of the aneurysm vessel is reduced to the half of the original diameter to observe the effects of smaller diameter and higher elasticity on the flow field. The results showed that the axial velocity profiles for the Newtonian and Carreau models are similar near the wall and the center of the cavity for the small and large artery geometries at the peak systole. At the end of the systole, the velocity profiles in the small arterial geometry are different than the large vessel, and the velocity values at the center of the vessel are higher compared to the large artery model. Also, the shear

thinning effects are less effective on the axial velocity in the small artery, since the reduction of the diameter increases the shear rate. The Oldroyd-B model shows that the increase in the elasticity changes the velocity field and the vortical structure. The vortical field for the different rheological models showed that, Newtonian and Carreau models are not affected significantly with the increase of the shear rate. However, the number, location, size and the rotation direction of the vortices corresponding to the viscoelastic fluid model are affected with the increasing elasticity. The investigation of the risk indicators shows that the average OSI as well as the regions under the high oscillatory shear stress are higher for the small artery geometry. Newtonian model underestimates the risk of rupture by underestimating the oscillations of the wall shear stress, and the average OSI predicted by the Carreau model is higher than the other rheological models. However, the viscoelastic model predicts that the region under the high oscillatory shear stress is bigger when compared to the Carreau model, and the TAWSS values show similar rupture risk for the small arterial geometry. Based on the risk indicators, the low TAWSS regions are found to be similar for the rheological models at the small vessel geometry. However, the shear thinning and viscoelastic models predict higher average OSI and bigger regions are being affected by the highly oscillating shear stress than the Newtonian model. The regions under high OSI are observed to be bigger for the viscoelastic fluid model than the Carreau model. Since the shear thinning and viscoelastic properties of the blood are well established, the modified Oldroyd-B model is assumed to mimic the physiological conditions more accurately. Therefore, assuming the blood as an inelastic fluid might predict lower risk of arterial degeneration and overlook significant risk of rupture.

# REFERENCES


1. Peterson, L. H., "The dynamics of pulsatile blood flow", *Circulation Research*, Vol. 2, No. 2, pp. 127–139, 1954.

2. Moini, J., *Phlebotomy: principles and practice*, Jones & Bartlett Learning, 2013.

3. Stoltz, J., "Hemorheology: pathophysiological significance.", *Acta Medica Portuguesa*, Vol. 6, No. 7-8, pp. 4–13, 1985.

4. Perktold, K., G. Karner, A. Leuprecht and M. Hofer, "Influence of non-Newtonian flow behavior on local hemodynamics", *ZAMM-Journal of Applied Mathematics and Mechanics/Zeitschrift für Angewandte Mathematik und Mechanik*, Vol. 79, No. S1, pp. 187–190, 1999.

5. Hell, K., A. Balzereit, U. Diebold and H. Bruhn, "Importance of blood viscoelasticity in arteriosclerosis", *Angiology*, Vol. 40, No. 6, pp. 539–546, 1989.

6. Baskurt, O. and H. Meiselman, "Blood rheology and hemodynamics.", *Seminars in Thrombosis and Hemostasis*, Vol. 29, p. 435, 2003.

7. Fisher, C. and J. S. Rossmann, "Effect of non-Newtonian behavior on hemodynamics of cerebral aneurysms", *Journal of Biomechanical Engineering*, Vol. 131, No. 9, p. 091004, 2009.

8. Lee, B.-K., S. Xue, J. Nam, H. Lim and S. Shin, "Determination of the blood viscosity and yield stress with a pressure-scanning capillary hemorheometer using constitutive models", *Korea-Australia Rheology Journal*, Vol. 23, No. 1, p. 1, 2011.

9. Morris, C. L., C. Smith 2nd and P. L. Blackshear Jr, "A new method for measuring the yield stress in thin layers of sedimenting blood", *Biophysical Journal*, Vol. 52, No. 2, pp. 229–240, 1987.

10. Lou, Z. and W.-J. Yang, "A computer simulation of the non-Newtonian blood flow at the aortic bifurcation", *Journal of Biomechanics*, Vol. 26, No. 1, pp. 37–49, 1993.

11. Malek, A. M., S. L. Alper and S. Izumo, "Hemodynamic Shear Stress and Its Role in Atherosclerosis", *Journal of the American Medical Association*, Vol. 282, No. 21, pp. 2035–2042, 1999.

12. Kawaguchi, T., S. Nishimura, M. Kanamori, H. Takazawa, S. Omodaka, K. Sato, N. Maeda, Y. Yokoyama, H. Midorikawa, T. Sasaki and M. Nishijima, "Distinctive flow pattern of wall shear stress and oscillatory shear index: similarity and dissimilarity in ruptured and unruptured cerebral aneurysm blebs", *Journal of Neurosurgery*, Vol. 117, No. 4, pp. 774–780, 2012.

13. Li, Z. and C. Kleinstreuer, "Effects of blood flow and vessel geometry on wall stress and rupture risk of abdominal aortic aneurysms", *Journal of Medical Engineering and Technology*, Vol. 30, No. 5, pp. 283–297, 2006.

14. Taylor, C. A., T. J. Hughes and C. K. Zarins, "Finite element modeling of three-dimensional pulsatile flow in the abdominal aorta: relevance to atherosclerosis", *Annals of Biomedical Engineering*, Vol. 26, No. 6, pp. 975–87, 1998.

15. Finol, E. A. and C. H. Amon, "Flow-induced wall shear stress in abdominal aortic aneurysms: Part II–pulsatile flow hemodynamics.", *Computer Methods in Biomechanics and Biomedical Engineering*, Vol. 5, No. 4, pp. 319–328, 2002.

16. Scotti, C. M., J. Jimenez, S. C. Muluk and E. A. Finol, "Wall stress and flow dynamics in abdominal aortic aneurysms: finite element analysis vs. fluid–structure interaction", *Computer Methods in Biomechanics and Biomedical Engineering*, Vol. 11, No. 3, pp. 301–322, 2008.

17. Budwig, R., D. Elger, H. Hooper and J. Slippy, "Steady flow in abdominal aortic aneurysm models.", *Journal of Biomechanical Engineering*, Vol. 115, No. 4A, pp.

418–423, 1993.

18. Berger, S. A. and L.-D. Jou, "Flows in stenotic vessels", *Annual Review of Fluid Mechanics*, Vol. 32, pp. 347–382, 2000.

19. Chien, S., S. Usami, R. J. Dellenback, M. I. Gregersen, L. B. Nanninga and M. M. Guest, "Blood viscosity: influence of erythrocyte aggregation", *Science*, Vol. 157, No. 3790, pp. 827–831, 1967.

20. Thurston, G. B., "Viscoelasticity of human blood", *Biophysical Journal*, Vol. 12, No. 9, pp. 1205–1217, 1972.

21. Thurston, G. B., "Frequency and shear rate dependence of viscoelasticity of human blood", *Biorheology*, Vol. 10, No. 3, pp. 375–381, 1973.

22. Thurston, G. B., "The effects of frequency of oscillatory flow on the impedance of rigid, blood-filled tubes", *Biorheology*, Vol. 13, No. 3, pp. 191–199, 1976.

23. Yeleswarapu, K. K., *Evaluation of continuum models for characterizing the constitutive behavior of blood*, Ph.D. Thesis, University of Pittsburgh, PA, USA, 1996.

24. Yeleswarapu, K., M. Kameneva, K. Rajagopal and J. Antaki, "The flow of blood in tubes: theory and experiment", *Mechanics Research Communications*, Vol. 25, No. 3, pp. 257–262, 1998.

25. Anand, M. and K. Rajagopal, "A shear-thinning viscoelastic fluid model for describing the flow of blood", *International Journal of Cardiovascular Medicine and Science*, Vol. 4, No. 2, pp. 59–68, 2004.

26. Anand, M., J. Kwack and A. Masud, "A new generalized Oldroyd-B model for blood flow in complex geometries", *International Journal of Engineering Science*, Vol. 72, pp. 78–88, 2013.

27. Campo-Deaño, L., R. P. Dullens, D. G. Aarts, F. T. Pinho and M. S. Oliveira,

"Viscoelasticity of blood and viscoelastic blood analogues for use in polydymethylsiloxane in vitro models of the circulatory system", *Biomicrofluidics*, Vol. 7, No. 3, p. 034102, 2013.

28. Bodnár, T., A. Sequeira and M. Prosi, "On the shear-thinning and viscoelastic effects of blood flow under various flow rates", *Applied Mathematics and Computation*, Vol. 217, No. 11, pp. 5055–5067, 2011.

29. Shariatkhah, A., M. Norouzi and M. R. H. Nobari, "Numerical simulation of blood flow through a capillary using a non-linear viscoelastic model", *Clinical Hemorheology and Microcirculation*, Vol. 62, No. 2, pp. 109–121, 2016.

30. Rojas, H. A. G., "Numerical implementation of viscoelastic blood flow in a simplified arterial geometry", *Medical Engineering & Physics*, Vol. 29, No. 4, pp. 491–496, 2007.

31. Hakim, S., J. Morshedian, M. R. G. Narenji and P. K. Nia, "Rheological modelling of Caspian pony blood", *Iranian Polymer Journal*, Vol. 10, pp. 293–303, 2001.

32. Namdee, K., M. Carrasco-Teja, M. Fish, P. Charoenphol and O. Eniola-Adefeso, "Effect of variation in hemorheology between human and animal blood on the binding efficacy of vascular-targeted carriers", *Scientific Reports*, Vol. 5, p. 11631, 2015.

33. College, O., *Anatomy and physiology*, Rice University, 2013.

34. Bergel, D., "The static elastic properties of the arterial wall", *The Journal of Physiology*, Vol. 156, No. 3, pp. 445–457, 1961.

35. Fuchs, R. F., *Zur Physiologie und Wachstumsmechanik des Blutgefäss-Systemes.*, Gustav Fischer, 1902.

36. Raghavan, M. L. and D. A. Vorp, "Toward a biomechanical tool to evaluate rupture

potential of abdominal aortic aneurysm: Identification of a finite strain constitutive model and evaluation of its applicability", *Journal of Biomechanics*, Vol. 33, No. 4, pp. 475–482, 2000.

37. Holzapfel, G. A., T. C. Gasser and R. W. Ogden, "A new constitutive framework for arterial wall mechanics and a comparative study of material models", *Journal of Elasticity and the Physical Science of Solids*, Vol. 61, No. 1-3, pp. 1–48, 2000.

38. Holzapfel, G. A., T. C. Gasser and R. W. Ogden, "Comparison of a multi-layer structural model for arterial walls with a Fung-type model, and issues of material stability", *Journal of Biomechanical Engineering*, Vol. 126, No. 2, pp. 264–275, 2004.

39. Ogden, R. W., "Nonlinear elasticity, anisotropy, material stability and residual stresses in soft tissue", *Biomechanics of Soft Tissue in Cardiovascular Systems*, pp. 65–108, Springer, 2003.

40. Dobrin, P. B., "Mechanical properties of arteries", *Physiological Reviews*, Vol. 58, No. 2, pp. 397–460, 1978.

41. Di Martino, E. S., G. Guadagni, A. Fumero, G. Ballerini, R. Spirito, P. Biglioli and A. Redaelli, "Fluid-structure interaction within realistic three-dimensional models of the aneurysmatic aorta as a guidance to assess the risk of rupture of the aneurysm", *Medical Engineering and Physics*, Vol. 23, No. 9, pp. 647–655, 2001.

42. Bilgi, C. and K. Atalık, "Numerical investigation of the effects of blood rheology and wall elasticity in abdominal aortic aneurysm under pulsatile flow conditions.", *Biorheology*, Vol. 56, No. 1, p. 51, 2019.

43. Watton, P., N. Hill and M. Heil, "A mathematical model for the growth of the abdominal aortic aneurysm", *Biomechanics and Modeling in Mechanobiology*, Vol. 3, No. 2, pp. 98–113, 2004.

44. Wolters, B., M. Rutten, G. Schurink, U. Kose, J. De Hart and F. Van De Vosse, "A patient-specific computational model of fluid–structure interaction in abdominal aortic aneurysms", *Medical Engineering & Physics*, Vol. 27, No. 10, pp. 871–883, 2005.

45. Venkatasubramaniam, A., M. Fagan, T. Mehta, K. Mylankal, B. Ray, G. Kuhan, I. Chetter and P. McCollum, "A comparative study of aortic wall stress using finite element analysis for ruptured and non-ruptured abdominal aortic aneurysms", *European Journal of Vascular and Endovascular Surgery*, Vol. 28, No. 2, pp. 168–176, 2004.

46. Sakalihasan, N., J.-B. Michel, A. Katsargyris, H. Kuivaniemi, J.-O. Defraigne, A. Nchimi, J. T. Powell, K. Yoshimura and R. Hultgren, "Abdominal aortic aneurysms", *Nature Reviews: Disease Primers*, Vol. 4, No. 1, p. 34, 2018.

47. Chervu, A., G. P. Clagett, R. J. Valentine, S. I. Myers and P. J. Rossi, "Role of physical examination in detection of abdominal aortic aneurysms", *Surgery*, Vol. 117, No. 4, pp. 454–457, 1995.

48. Vorp, D. A., "Biomechanics of abdominal aortic aneurysm", *Journal of Biomechanics*, Vol. 40, No. 9, pp. 1887–1902, 2007.

49. Fillinger, M. F., S. P. Marra, M. L. Raghavan and F. E. Kennedy, "Prediction of rupture risk in abdominal aortic aneurysm during observation: Wall stress versus diameter", *Journal of Vascular Surgery*, Vol. 37, No. 4, pp. 724–732, 2003.

50. Kerstein, M. D., P. V. Moulder and W. R. Webb, *Aneurysms*, Williams & Wilkins, 1983.

51. Egelhoff, C. J., R. S. Budwig, D. F. Elger, T. A. Khraishi and K. H. Johansen, "Model studies of the flow in abdominal aortic aneurysms during resting and exercise conditions", *Journal of Biomechanics*, Vol. 32, No. 12, pp. 1319–1329, 1999.

52. Fukushima, T., T. Matsuzawa and T. Homma, "Visualization and finite element analysis of pulsatile flow in models of the abdominal aortic aneurysm", *Biorheology*, Vol. 26, No. 2, pp. 109–130, 1989.

53. Viswanath, N., C. M. Rodkiewicz and S. Zajac, "On the abdominal aortic aneurysms: Pulsatile state considerations", *Medical Engineering and Physics*, Vol. 19, No. 4, pp. 343–351, 1997.

54. Rathish Kumar, B. V. and K. B. Naidu, "Hemodynamics in aneurysm", *Computers and Biomedical Research*, Vol. 29, No. 2, pp. 119–139, 1996.

55. Taylor, C. A., M. T. Draney, J. P. Ku, D. Parker, B. N. Steele, K. Wang and C. K. Zarins, "Predictive medicine: Computational techniques in therapeutic decision-making", *Computer Aided Surgery*, Vol. 4, No. 5, pp. 231–247, 1999.

56. Javadzadegan, A., A. Simmons, M. Behnia and T. Barber, "Computational modelling of abdominal aortic aneurysms: Effect of suprarenal vs infrarenal positions", *European Journal of Mechanics, B/Fluids*, Vol. 61, pp. 112–124, 2017.

57. Khanafer, K. M., P. Gadhoke, R. Berguer and J. L. Bull, "Modeling pulsatile flow in aortic aneurysms: effect of non-Newtonian properties of blood.", *Biorheology*, Vol. 43, No. 5, pp. 661–679, 2006.

58. Neofytou, P. and S. Tsangaris, "Flow effects of blood constitutive equations in 3D models of vascular anomalies", *International Journal for Numerical Methods in Fluids*, Vol. 51, No. 5, pp. 489–510, jun 2006.

59. Arzani, A., "Accounting for residence-time in blood rheology models: do we really need non-Newtonian blood flow modelling in large arteries?", *Journal of The Royal Society Interface*, Vol. 15, No. 146, p. 20180486, 2018.

60. Les, A. S., S. C. Shadden, C. A. Figueroa, J. M. Park, M. M. Tedesco, R. J. Herfkens, R. L. Dalman and C. A. Taylor, "Quantification of hemodynamics in

abdominal aortic aneurysms during rest and exercise using magnetic resonance imaging and computational fluid dynamics", *Annals of Biomedical Engineering*, Vol. 38, No. 4, pp. 1288–1313, 2010.

61. Crosetto, P., P. Reymond, S. Deparis, D. Kontaxakis, N. Stergiopulos and A. Quarteroni, "Fluid-structure interaction simulation of aortic blood flow", *Computers and Fluids*, Vol. 43, No. 1, pp. 46–57, 2011.

62. Leung, J. H., A. R. Wright, N. Cheshire, J. Crane, S. A. Thom, A. D. Hughes and Y. Xu, "Fluid structure interaction of patient specific abdominal aortic aneurisms: A comparison with solid stress models", *BioMedical Engineering Online*, Vol. 5, No. 1, p. 33, 2006.

63. Papaharilaou, Y., J. A. Ekaterinaris, E. Manousaki and A. N. Katsamouris, "A decoupled fluid structure approach for estimating wall stress in abdominal aortic aneurysms", *Journal of Biomechanics*, Vol. 40, No. 2, pp. 367–377, 2007.

64. Moireau, P., N. Xiao, M. Astorino, C. A. Figueroa, D. Chapelle, C. A. Taylor and J. F. Gerbeau, "External tissue support and fluid-structure simulation in blood flows", *Biomechanics and Modeling in Mechanobiology*, Vol. 11, No. 1-2, pp. 1–18, 2012.

65. Stergiou, Y. G., A. G. Kanaris, A. A. Mouza and S. V. Paras, "Fluid-Structure Interaction in Abdominal Aortic Aneurysms: Effect of Haematocrit", *Fluids*, Vol. 4, No. 1, p. 11, 2019.

66. Marrero, V. L., J. A. Tichy, O. Sahni and K. E. Jansen, "Numerical Study of Purely Viscous Non-Newtonian Flow in an Abdominal Aortic Aneurysm", *Journal of Biomechanical Engineering*, Vol. 136, No. 10, p. 101001, 2014.

67. Xenos, M., S. H. Rambhia, Y. Alemu, S. Einav, N. Labropoulos, A. Tassiopoulos, J. J. Ricotta and D. Bluestein, "Patient-based abdominal aortic aneurysm rupture risk prediction with fluid structure interaction modeling", *Annals of Biomedical*

*Engineering*, Vol. 38, No. 11, pp. 3323–3337, 2010.

68. Arzani, A. and S. C. Shadden, "Characterization of the transport topology in patient-specific abdominal aortic aneurysm models", *Physics of Fluids*, Vol. 24, No. 8, p. 081901, 2012.

69. Di Achille, P., G. Tellides and J. D. Humphrey, "Hemodynamics-driven deposition of intraluminal thrombus in abdominal aortic aneurysms", *International Journal for Numerical Methods in Biomedical Engineering*, Vol. 33, No. 5, pp. 1–17, 2017.

70. Raptis, A., M. Xenos, E. Georgakarakos, G. Kouvelos, A. Giannoukas, N. Labropoulos and M. Matsagkas, "Comparison of physiological and post-endovascular aneurysm repair infrarenal blood flow", *Computer Methods in Biomechanics and Biomedical Engineering*, Vol. 20, No. 3, pp. 242–249, 2017.

71. Chiu, J. J., D. L. Wang, S. Chien, R. Skalak and S. Usami, "Effects of disturbed flows on endothelial cells", *Journal of Biomechanical Engineering*, Vol. 120, No. February 1998, pp. 2–8, 1998.

72. Kleinstreuer, C., M. Nazemi and J. P. Archie, "Numerical analysis of fluid-particle dynamics in artery bifurcation with stenosis and surgical reconstruction", *World Congress on Medical Physics and Biomechanical Engineering*, Vol. 33, San Antonio, Texas, 1988.

73. Ku, D. N., D. P. Giddens, C. K. Zarins and S. Glagov, "Pulsatile flow and atherosclerosis in the human carotid bifurcation. Positive correlation between plaque location and low oscillating shear stress", *Arteriosclerosis, Thrombosis, and Vascular Biology*, Vol. 5, No. 3, pp. 293–302, 1985.

74. Arzani, A. and S. C. Shadden, "Characterizations and correlations of wall shear stress in aneurysmal flow", *Journal of Biomechanical Engineering*, Vol. 138, No. 1, p. 014503, 2016.

75. Mills, C. J., I. T. Gabe, J. H. Gault, D. T. Mason, J. Ross, E. Braunwald and J. P. Shillingford, "Pressure-flow relationships and vascular impedance in man", *Cardiovascular Research*, Vol. 4, No. 4, pp. 405–417, 1970.

76. Charm, S. E., W. McComis and G. Kurland, "Rheology and structure of blood suspensions", *Journal of Applied Physiology*, Vol. 19, No. 1, pp. 127–133, 1964.

77. Cho, Y. I. and K. R. Kensey, "Effects of the non-Newtonian viscosity of blood on flows in a diseased arterial vessel. Part 1: Steady flows", *Biorheology*, Vol. 28, No. 3-4, pp. 241–262, 1991.

78. Brust, M., C. Schaefer, R. Doerr, L. Pan, M. Garcia, P. Arratia and C. Wagner, "Rheology of human blood plasma: Viscoelastic versus Newtonian behavior", *Physical Review Letters*, Vol. 110, No. 7, p. 078305, 2013.

79. Scotti, C. M. and E. A. Finol, "Compliant biomechanics of abdominal aortic aneurysms: A fluid-structure interaction study", *Computers and Structures*, Vol. 85, No. 11-14, pp. 1097–1113, 2007.

80. Veshkina, N., *Determination of hemodynamics in collapsible walls*, Ph.D. Thesis, Lodz University of Technology, 2013.

81. Kleinstreuer, C., *Biofluid Dynamics Principles and Selected Applications*, p. 286, CRC Press, 2006.

82. Holzapfel, A. G., *Nonlinear solid mechanics II*, John Wiley & Sons, Inc., 2000.

83. Khan, M., D. Steinman and K. Valen-Sendstad, "Non-Newtonian versus numerical rheology: Practical impact of shear-thinning on the prediction of stable and unstable flows in intracranial aneurysms", *International Journal for Numerical Methods in Biomedical Engineering*, Vol. 33, No. 7, p. e2836, 2017.

84. Phillips, S. D., *Analysis of complex viscoelastic flows using a finite element method.*,

Ph.D. Thesis, Massachusetts Institute of Technology, 2006.

85. Coronado, O. M., D. Arora, M. Behr and M. Pasquali, "Four-field Galerkin/least-squares formulation for viscoelastic fluids", *Journal of Non-Newtonian Fluid Mechanics*, Vol. 140, No. 1-3, pp. 132–144, 2006.

86. Behr, M., D. Arora, O. Coronado and M. Pasquali, "GLS-type finite element methods for viscoelastic fluid flow simulation", *Proceedings of the Third MIT Conference on Computational Fluid and Solid Mechanics, Massachusetts Institute of Technology, Cambridge, USA*, pp. 135–308, 2005.

87. Malina, M., T. Lanne, K. Ivancev, B. Lindblad and J. Brunkwall, "Reduced pulsatile wall motion of abdominal aortic aneurysms after endovascular repair", *Journal of Vascular Surgery*, Vol. 27, No. 4, pp. 624–631, 1998.

88. Meng, S., X. K. Li and G. Evans, "Numerical simulation of Oldroyd-B fluid in a contraction channel", *The Journal of Supercomputing*, Vol. 22, No. 1, pp. 29–43, 2002.

89. Sato, T. and S. M. Richardson, "Explicit numerical simulation of time-dependent viscoelastic flow problems by a finite element/finite volume method", *Journal of Non-Newtonian Fluid Mechanics*, Vol. 51, No. 3, pp. 249–275, 1994.

90. Alves, M. A., P. J. Oliveira and F. T. Pinho, "Benchmark solutions for the flow of Oldroyd-B and PTT fluids in planar contractions", *Journal of Non-Newtonian Fluid Mechanics*, Vol. 110, No. 1, pp. 45–75, 2003.

91. Mercan, H. and K. Atalık, "Flow structure for Power-Law fluids in lid-driven arc-shape cavities", *Korea-Australia Rheology Journal*, Vol. 23, No. 2, pp. 71–80, 2011.

92. Hans, S. S., O. Jareunpoon, M. Balasubramaniam and G. B. Zelenock, "Size and location of thrombus in intact and ruptured abdominal aortic aneurysms", *Journal of Vascular Surgery*, Vol. 41, No. 4, pp. 584–588, 2005.

93. Glor, F., B. Ariff, A. Hughes, L. Crowe, P. Verdonck, D. Barratt, S. Thom, D. Firmin and X. Xu, "The integration of medical imaging and computational fluid dynamics for measuring wall shear stress in carotid arteries", *Annual International Conference of the IEEE Engineering in Medicine and Biology - Proceedings*, Vol. 26 II, 2004.